NORTHWESTERN UNIVERSITY

Measurement of the W Boson Mass in Proton-Antiproton Collisions at a Center of Mass Energy of 1.96 TeV

A DISSERTATION

SUBMITTED TO THE GRADUATE SCHOOL
IN PARTIAL FULFILLMENT OF THE REQUIREMENTS

for the degree

DOCTOR OF PHILOSOPHY

Field of Physics and Astronomy

By

Sahal Yacoob

EVANSTON, ILLINOIS

June 2010

ABSTRACT

Measurement of the W Boson Mass in Proton-Antiproton Collisions at a Center of Mass Energy of 1.96 TeV

Sahal Yacoob

I present the measurement of the mass of the W Boson in the electron channel using 4.4 fb^{-1} of $p\bar{p}$ collisions at $\sqrt{s} = 1.96$ TeV recorded by the D0 detector operating at the Fermilab Tevatron Collider.

Acknowledgements

My friends and family, particularly my parents Anu and Zak Yacoob, and Diana Carlson who have been unfailingly supportive and generous while sharing the highs and lows of this process, are the reason I have been able to complete this work. They, unlike myself, have had to deal with stresses over which they had no control due to my studies and I will always be grateful.Financial support from the United States Department of Energy, enabling me to devote my time completely to my studies has been greatly appreciated. Discussions with Tim Andeen and Alex Melnitchouk have always been illuminating and led to a deeper understanding of the subject. Pierre Petroff has also provided a deeper understanding of the challenges associated with the analysis, while being supportive and encouraging. A measurement of the W boson mass at DØ to this level of accuracy would have been impossible without the work accomplished by Dr. Jan Stark on calorimeter calibration. My supervisors Dr. Jan Stark, and Prof. Heidi M. Schellman who have seen the best, and the worst, of me and through it all been supportive and encouraging and gone out of their way to contribute to my success, have guided me through this process successfully and for that I will be forever grateful. Robert Tilden has been a good friend and always ensured that I had a terminal to work at, while encouraging me to always consider other viewpoints. A final thank you to Jeanette Ortiz, and Drew Alexander for allowing me to cohabit with them and dealing with my stresses over the final few weeks

of this work.

The financial assistance of the National Research Foundation (NRF) of South Africa towards this research is hereby acknowledged. Opinions expressed and conclusions arrived at, are those of the author and are not necessarily to be attributed to the NRF.

Table of Contents

List of Tables

List of Figures

CHAPTER 1

Introduction

The current description of fundamental constituents of matter, and the forces between them is stated in the language of field theory. Treatments of this description (The Standard Model, or SM) and the underlying mathematical concepts may be found in reference [**7**], a less technical description of elements of the SM which relate to this work are presented in Chapter 2. Chapter 3 describes the detector, and the environment in which this measurement was performed. The remaining chapters will focus on the details of the analysis performed to determine the mass of the W boson.

1.1. The Importance of the W boson Mass Measurement

The SM requires the existence of a Higgs field. Interactions of particles with the Higgs field are responsible for the non-zero mass of fundamental particles. The heavier a particle is, the stronger its interaction with the Higgs field will be. A consequence of this is the existence of a spin zero particle, the Higgs boson, a quantum of the Higgs field. The lack of direct observation of the Higgs boson is the largest discrepancy between experiment and the SM; at the same time self-consistency arguments lead one to the conclusion that the SM is not the true underlying theory of nature. In this context, it should be clear that direct observation and characterization of the Higgs boson, or the exclusion of the Higgs boson (as described in the SM) is currently of the highest priority. It is hoped that we find a discrepancy between the SM and our observations, which will direct us towards

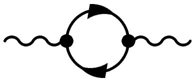

Figure 1.1. Top quark loop correction to the W propagator.

Figure 1.2. An example of a Higgs boson loop correction to the W propagator.

a better understanding of nature.

Within the SM the known masses of observed particles depend on their interaction with the Higgs boson, one can invert this dependence to constrain the Higgs boson mass due to the measured masses of observed particles. In particular the mass of the Higgs boson (m_H^{sm}) affects the masses of the Z (m_Z), and W (m_W) bosons (due to the radiative corrections to the propagator shown in figures 1.1 and 1.2); The uncertainty prediction of m_H^{sm} is currently dominated by the uncertainty on m_W and to a lesser extent on the uncertainty of the top quark mass (m_t). The current uncertainty on m_W needs to be reduced from 23 MeV to 8 MeV in order to be as strong of a constraint on m_H^{sm} as the uncertainty on m_t.

1.1.1. Current Constraints on m_H^{sm}

The combination of precision electroweak measurements [**1**] sets tight constraints on m_H^{sm}. The 95 % confidence limit upper bound is $m_H^{sm} < 186$ GeV. The $\Delta\chi^2$ plot of this result is shown as Figure 1.3. The yellow bands in Figure 1.3 show the regions excluded by direct

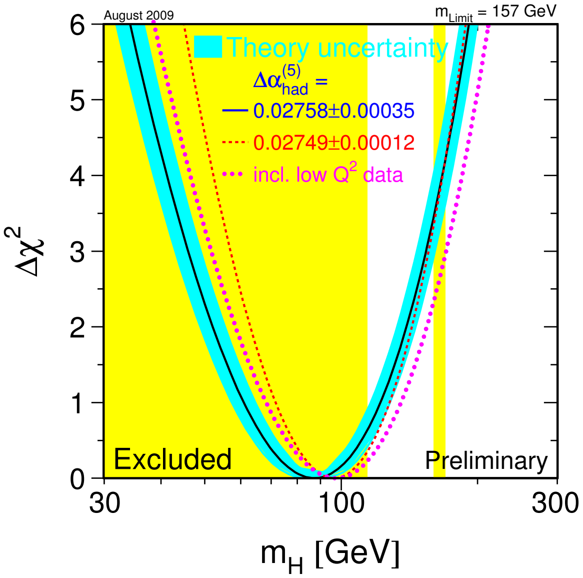

Figure 1.3. $\Delta\chi^2 = \chi^2 - {\chi_{min}}^2$ vs. m_H using precision Electroweak data [**1**].

searches at LEP (114 GeV $< m_H^{sm}$) and the Tevatron [**8**] (160 GeV to 170 GeV). As shown in the figure the best-fit value has been ruled out. Figure 1.4 shows the dependence of the allowed range of m_H^{sm} on the uncertainties of m_W and m_t.

1.1.2. Current Value of m_W and Recent Measurements thereof

The current World Average mass of the W boson is $m_W = 80.399 \pm 0.023$GeV [**2**] and is dominated by LEP and Tevatron measurements as shown in Figure 1.5. The most recently published measurement, to which I have contributed, is from the DØ Collaboration with 1 fb^{-1} of Data [**9**] and is shown in figure 1.5. This work is an extension of that analysis to higher precision with a factor of 4 greater statistics, incorporating changes which are

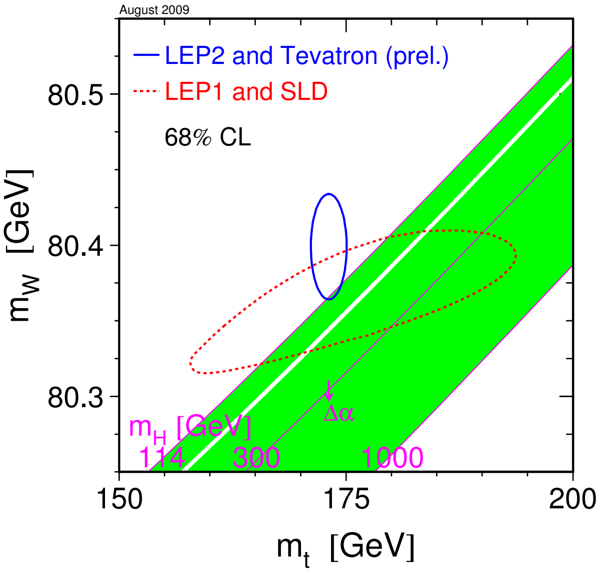

Figure 1.4. The comparison of the indirect constraints on m_W and m_t based on LEP-I/SLD data (dashed contour) and the direct measurements from the LEP-II/Tevatron experiments (solid contour). In both cases the 68% CL contours are plotted. Also shown is the SM relationship for the masses as a function of the Higgs mass in the region favored by theory ($<$ 1000 GeV) and allowed by direct searches (114 GeV to 170 GeV and $>$ 180 GeV) [**1**].

made necessary due to the higher instantaneous luminosity of the Tevatron as described in Chapter 3.

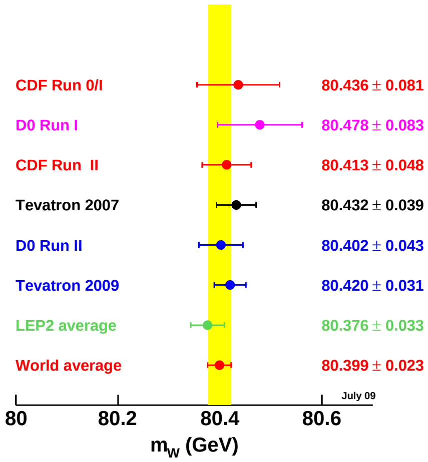

Figure 1.5. Measurements of m_W compared to the world average value [**2**].

CHAPTER 2

Theoretical Overview

2.1. Standard Model Overview

The Standard Model (SM) description of nature has stubbornly refused to yield under pressure from many experimental tests. The ability to describe these experimental results within the SM is unfortunately a source of consternation, since the model is not theoretically sound to all energy scales and as such is not believed to be the true description of the particles and forces of nature. Indeed the SM does not include masses for the neutrinos, tell us whether their mass hierarchy is ‘normal’ or ‘inverted’, tell us if neutrinos are Majorana or Dirac particles, or provide a quantum description of gravity. We hope to be able to discover the underlying theory of nature, which will hopefully describe all of existence at all scales.

The SM has as its components the fermions (matter particles) shown in table 2.1, which may be divided into generations (columns of increasing mass), and the bosons responsible for the forces between these particles. The fermion sector is subdivided into particles which exhibit a color charge (quarks) or rather ‘feel’ the strong force of Quantum Chromo Dynamics, and those that do not (leptons). The Z^0/γ and $W^{\pm}$ bosons mediate the electroweak force, and the gluons mediate the strong force. The most glaring failure of the standard model is that in order to provide masses for the elementary particles in a consistent way the model requires there to be a complex scalar $SU(2)_L$ doublet field (the Higgs

quarks	u	c	t
	d	s	b
leptons	e	μ	τ
	ν_e	ν_μ	ν_τ

Table 2.1. Table of fermions.

field) with finite vacuum expectation value which provides masses to particles based on the strength of their coupling to field. We would expect the photon not to couple to the Higgs field at all and the top quark to have a significantly larger coupling than a neutrino. An unintended consequence of this mechanism is that there now must exist an additional boson, the Higgs boson, the quantum of the Higgs field.

As Shown in Figure 1.3, a fit to high Q^2 data (based on indirect effects on masses and couplings), where Q is the momentum transfer of the inelastic collision, predicts the mass of the Higgs boson to be 87 GeV with 1 sigma uncertainty of $+25$ and -36 GeV which falls in the region already excluded by direct searches at LEP. This discrepancy between direct and indirect evidence constraining m_H^{sm} is the most promising avenue for finally identifying a failure of the SM which we can then further investigate. It must be said that it is still possible for a Higgs boson to be detected at a mass that is not very incompatible with the standard model, but increasing the precision of the measurements contributing to the indirect constraint on m_H^{sm} will reduce the allowed parameter space for this to occur.

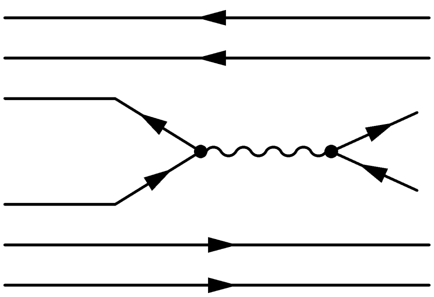

Figure 2.1. Tree Level$W$ boson/ Z Boson production example at the Tevatron showing spectator valence quarks (not involved in the hard scatter)

2.2. W Boson Mass

Within the SM the mass of the W boson may be expressed as:

$$m_W = \sqrt{\frac{\pi\alpha}{G_F\sqrt{2}} \frac{1}{\sin^2\theta_w\,(1-\delta r)}}, \tag{2.1}$$

where the term δr is due to radiative corrections to the W boson propagator dominated by (anti-)top (shown in figure 1.1) and Higgs (shown in figure 1.2) loop corrections, θ_w is the Weinberg angle defined by the relative magnitudes of the weak and electromagnetic couplings in the SM Lagrangian (renormalized to $\sin^2\theta_w = 1 - \frac{m_W^2}{m_Z^2}$), α is the electromagnetic coupling constant, m_t is the top quark mass and G_F is the Fermi Constant. δr is quadratically proportional to M_{top} and logarithmically dependent on m_H^{sm}.

2.3. Boson Production at a Hadron Collider

To leading order production of W/Z Bosons at the Tevatron is dominated by the tree level diagram shown in figure 2.1, where the (anti)proton is represented by its valence (anti)quark constituents. The cross section (σ) for this interaction is given by:

$$\sigma_{bw} \propto \frac{s\Gamma_V^2/m_V^2}{(s-m_V^2)^2 + s^2\Gamma_0^2/m_V^2}, \tag{2.2}$$

Where m_V and Γ_V are the mass and width of the boson being produced, and ($\sqrt{s}$) is the centre of mass energy of the hard scatter ($Q^2 = s$) . This simple picture breaks down at the Tevatron and the (anti)proton needs to be considered as a composite object of many partons. It is important to note that although the (anti)proton momentum is well determined, each parton (i) carries only a fraction (x_i) of the proton momentum. The fraction of the total momentum carried by a parton i (x_i) when the (anti)proton is probed at a particular momentum scale is parameterized for 7 flavors of partons (6 quarks and anti-quarks and the gluons) and determined by combining and fitting data from many sources. Examples of these parton distribution functions (PDFs) include those provided by the CTEQ collaboration [**10**], as well as the ABKM [**11**]and MSTW [**12**] sets. The convolution of the tree level cross section (equation 2.2) with the PDFs gives the full description of the production cross section at the Tevatron:

$$\sigma = \sum_{ij} \int dx_1 dx_2 f_i(x_1, Q^2) f_j(x_2, Q^2) \sigma_{bw}(ij), \tag{2.3}$$

where the sum is over the incoming parton flavors and the function f_i is the PDF for parton flavor i.

2.3.1. Boson Transverse Momentum Distribution

Due to momentum conservation it should be clear that within the picture described above, bosons will be produced with little to no transverse momentum (p_T), and any transverse momentum will be limited to intrinsic transverse momentum of quark anti-quark centre-of-mass system in the lab frame. Practically this is again an over-simplification of the picture, higher order corrections to the tree level diagram in figure 2.1 such as initial state gluon radiation provide a mechanism for production of bosons with significant p_T. A full theoretical description of the p_T and η dependent differential cross sections for production of a boson (V) plus something (X) as a result of the scattering between partons i and j has been presented by Collins, Soper and Sterman [**13**], and involves a regularized singular term (Y), and a term (W) involving the integral over $1/p_T$ (b).

$$\frac{d\sigma(ij \to VX)}{dQ^2 dQ_T{}^2 d_y} = \frac{1}{(2\pi)^2}\delta(Q^2 - M_V{}^2) \int d^2b\, e^{i\vec{Q_T}\vec{b}}\, W_{ij}(b, Q, x_1, x_2) + Y(Q_T, Q, x_1, x_1), \tag{2.4}$$

The function W_{ij} in the integrand may be factorized into a function calculable in perturbative QCD (W_1) and one involving free parameters which need to be determined by comparison to data (W_2) where the incoming parton flavor is still important in general but has been dropped for this discussion, and Q_T is the transverse component of the momentum transfer vector. In particular the authors of [**13**]state:

$$W_2 = \exp\left(-F_1(b)\ln\frac{Q^2}{Q_0^2} - F_2(x_1, b) - F_3(x_2, b)\right), \tag{2.5}$$

Landry, Brock, Nadolsky and Yuan [**14**] have used a wide range of data to determine the explicit (BLNY) parameterization of equation 2.5:

$$W_2 = \exp\left[\left(-g_1 - g_2\ln\frac{Q^2}{Q_0^2} - g_1 g_2 \ln(100 x_1 x_2)\right) b^2\right], \tag{2.6}$$

In particular measurements by DØ have shown good agreement with the central Z boson p_T distribution [**15**]. For this analysis we restrict ourselves to the region $p_T < 30\text{GeV}$ where the shape of the measured distribution is most sensitive to g_2.

2.4. Boson Decay

The W and Z bosons can decay into any of the fermions listed in table 2.1 although a decay with a top quark in the final state is kinematically suppressed due to the high mass of the top quark (172GeV) with respect to the Z (91.188 GeV) and W (approximately 80 GeV) boson masses. The Z boson will decay into particle anti-particles pairs, while the W boson will decay into 2 fermions from any given column of table 2.1 (the left handled doublet states [**7**])or their anti-particles. Although the dominant decay channel is into quarks (and thus hadronic jets), the large cross section for jet production at the Tevatron combined with the comparatively poor jet energy scale resolution means that we will concern ourselves with the lepton decay channels which comprise about 10% of the total branching fraction. The W and Z bosons decay equally in the electron, muon and tauon channels. The τ particle is difficult to detect as it decays before reaching our detector. Due to the superior energy resolution of our electromagnetic calorimeter in comparison to the tracking and muon systems this analysis will focus on the electron decay channel. For the remainder of this work the term electron will be used to refer to both electrons and positrons and the term neutrino can be assumed to refer to the ν_e or $\bar{\nu_e}$ unless otherwise specified.

In the boson rest frame the lepton products of the decay will be back to back with each carrying half the energy of the boson. Here we can already note that the energy of the boson decay products is sensitive to the mass of the boson. The angular distribution of the lepton decay products with respect to the bisector of the incoming beams in the rest frame of the boson differs for W and Z boson events. The general form of the angular decay distribution for Drell-Yan (Z boson) decay products in this frame is [**16**]:

$$\frac{dN}{d\Omega} \propto 1 + \cos^2\theta + (\frac{1}{2} - \frac{3}{2}\cos^2\theta)A_0 + 2\cos\theta\sin\theta\cos\phi A_1 + \frac{1}{2}\sin^2\theta\cos 2\phi A_2 \tag{2.7}$$

and for W boson decay products is [**17**]

$$\frac{dN^{\mp}}{d\Omega} \propto 1 \pm \alpha_1\cos\theta + \alpha_2\cos^2\theta \tag{2.8}$$

where θ is the angle between the lepton and the inner bisector of the beams, and ϕ is measured with respect to the plane defined by the incoming beams. α_2 and the A_i go to zero with the boson transverse momentum, and can be computed perturbatively. The term N^- in equation 2.8 refers to the number of W^- particles. For a $Z \to ee$ event one is able to reconstruct the hard scatter by combining the 2 electron four vectors. Since the neutrino from W boson decay is invisible (does not interact with our detector) we are left to infer its properties from momentum conservation. Having no information about the initial longitudinal momentum (along the beam direction) of the W boson we can still assume that any transverse momentum imbalance is due to momentum carried by the neutrino.

The electron may radiate photons (final state radiation [FSR]) and this 2^{nd} order process interferes with the initial state electromagnetic radiation mentioned earlier.

2.5. Kinematic Observables

The rapidity of a particle is defined as:

$$y \equiv \frac{1}{2}\ln\left(\frac{E + P_l}{E - P_l}\right) \tag{2.9}$$

where E is the energy of the particle and P_l is the longitudinal momentum. In the limit $E >> m$ this may be approximated by the pseudorapidity:

$$\eta \equiv -\ln\left(\tan\frac{\theta}{2}\right) \tag{2.10}$$

where θ is the polar angle defined with respect to the proton beam direction.

When describing detector coordinates in the lab frame it is common to use the term η_{det}, defined as the pseudorapidity of a particle which has been produced at the origin (0,0,0) in the detector co-ordinate system. In order to avoid confusion η is sometimes referred to as η_{phys}. The invariant mass of a particle as a function of its mass-less decay products is:

$$m^2 \equiv 2(E(1) \cdot E(2) - \vec{p}(1) \cdot \vec{p}(2)) \tag{2.11}$$

where $E(i)$ ($\vec{p}(i)$) is the energy (momentum) of particle i. and finally the transverse mass of a particle is defined in an analogous way:

$${m_T}^2 \equiv 2(E_T(1) \cdot E_T(2) - \vec{p}_T(1) \cdot \vec{p}_T(2)) \tag{2.12}$$

where $\vec{p}_T$ is momentum transverse to the beam axis, and E_T is the magnitude of the transverse momentum vector.

CHAPTER 3

Experimental Apparatus

3.1. The Tevatron

The Tevatron is a proton(p)-anti-proton($\overline{p}$) synchrotron accelerator located at Fermi National Accelerator Laboratory with beam energy of 0.98 TeV. The protons and anti-protons travel in ‘bunches’. There are 36 proton and anti-proton bunches comprising the beam circulating in opposite directions, and crossing at collision points every 396 ns. The instantaneous luminosity ($\mathcal{L}$) is a measure of the probability for a hard scatter to take place, for each of the thirty-six possible crossing pairs (Ticks). It is recorded in inverse barns per second averaged over 60 second intervals. (The integrated luminosity is measured in inverse barns.) Data from the Tevatron can be separated into 3 distinct categories, Run I (1992 – 1996) at 0.90 TeV per beam delivered approximately 160 pb^{-1} per experiment; RunIIa (2002 – 2006) at 0.98 TeV per beam delivered 1.41 fb^{-1} to DØ; and RunIIb which began in 2006 at 0.98 TeV per beam which has delivered over 8 fb^{-1} of which 4.35 fb^{-1} collected between the ninth of June 2006 and the thirteenth of June 2009 is used for this analysis. RunIIb is characterized by higher instantaneous luminosities with regards to RunIIa with the mean increasing by a factor of 3, and is still in progress. For our data sample (RunIIb) these high instantaneous luminosities, while providing large data samples, have lead to challenges described in detail later. In brief, there is a large amount of energy recorded in the detector in any given event which is uncorrelated with the boson production we are trying to study, but which we need to describe correctly, taking into account its effect on the overall detector energy response, and the degradation of tracking and triggering.

3.2. DØ Detector

3.2.1. Overview

Located at the south-east side of the Tevatron, DØ is a multi-purpose detector, combining tracking, calorimetry, and muon detectors to study the events created by p-$\bar{p}$ collisions at the Tevatron, to test the Standard Model. Unless otherwise specified this description relies on ref [**18**]. Figure 3.1 shows an overview of the detector. The sub-detector systems visible (from the outside moving inwards) are the muon system, calorimeter, pre-shower, fiber tracker, and silicon tracker. The luminosity monitors are at high $|\eta|$ and are not shown in this figure. Between the central fiber tracker and pre-shower is a solenoid providing the magnetic field used to determine momentum from reconstructed tracks. For RunIIb the tracking system and calorimeter triggers have been upgraded in comparison to RunIIa. This analysis depends on the tracking system to help with event selection and background subtraction, but is most sensitive to the response of the calorimeters. Our ability to understand and characterize the calorimeter response will determine how precisely we are able to measure the lepton energy and the missing transverse energy.

3.2.2. Tracking System

The tracking system lies immediately outside the beam pipe and is surrounded by a solenoidal magnet as shown in figure 3.2. It is comprised of two separate detectors,

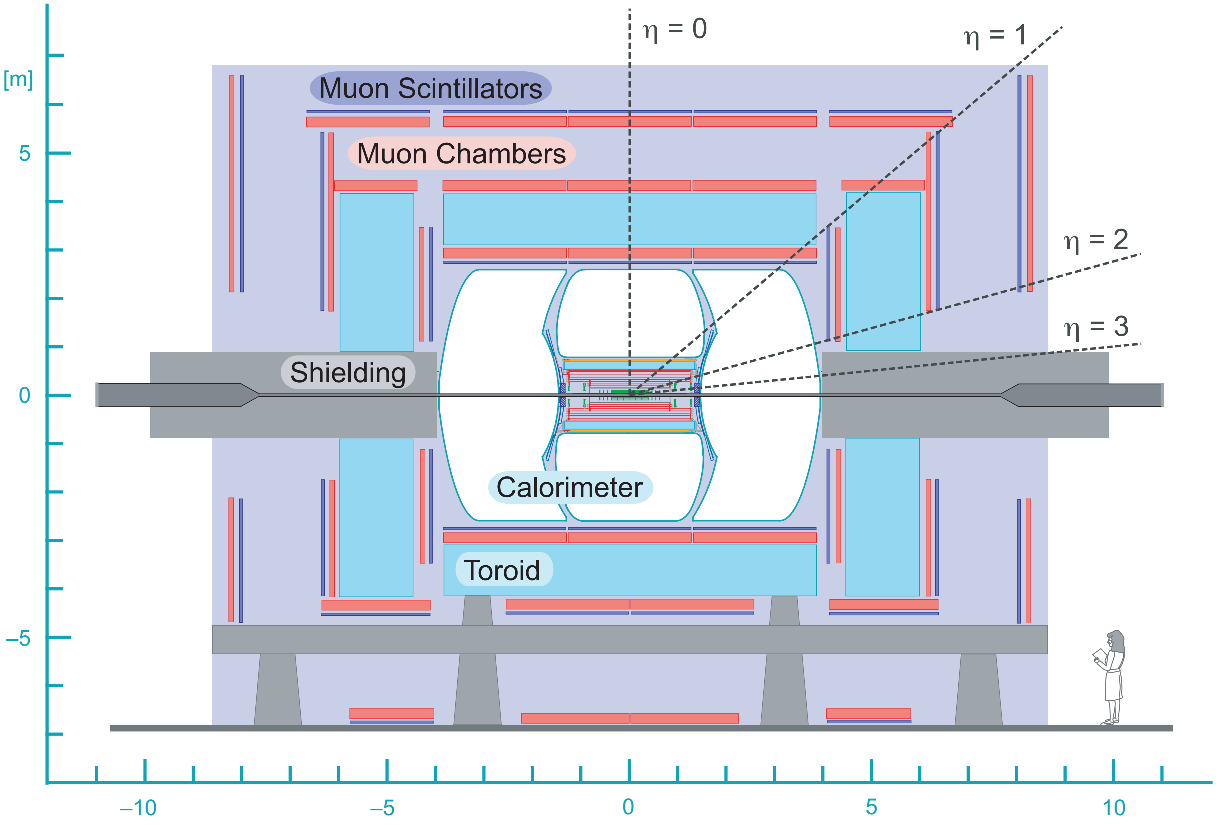

Figure 3.1. the DØ detector

a silicon micro-strip tracker (SMT) and a central fiber tracker (CFT). For RunIIb an additional layer has been added to the SMT called layer 0 and described in reference [**19**] to allow for efficient tracking with the increased beam luminosity.

3.2.2.1. Silicon Tracker. The SMT (disregarding layer 0 for now) consists of six (twelve cm long) barrel segments parallel to the beam each consisting of 4 layers, and 16 disks perpendicular to the beam arranged as shown in figures 3.2 and 3.3. The barrel segments extend to $|z| < 37.8$ cm and provide a measurement of $r - \phi$ with a resolution of 10 μm. Each barrel segment is terminated at high $|z|$ with an 'F-disk', a disk of 12 wedges placed perpendicular to the beam. Six additional F-disk arrangements are placed at higher $|z|$.

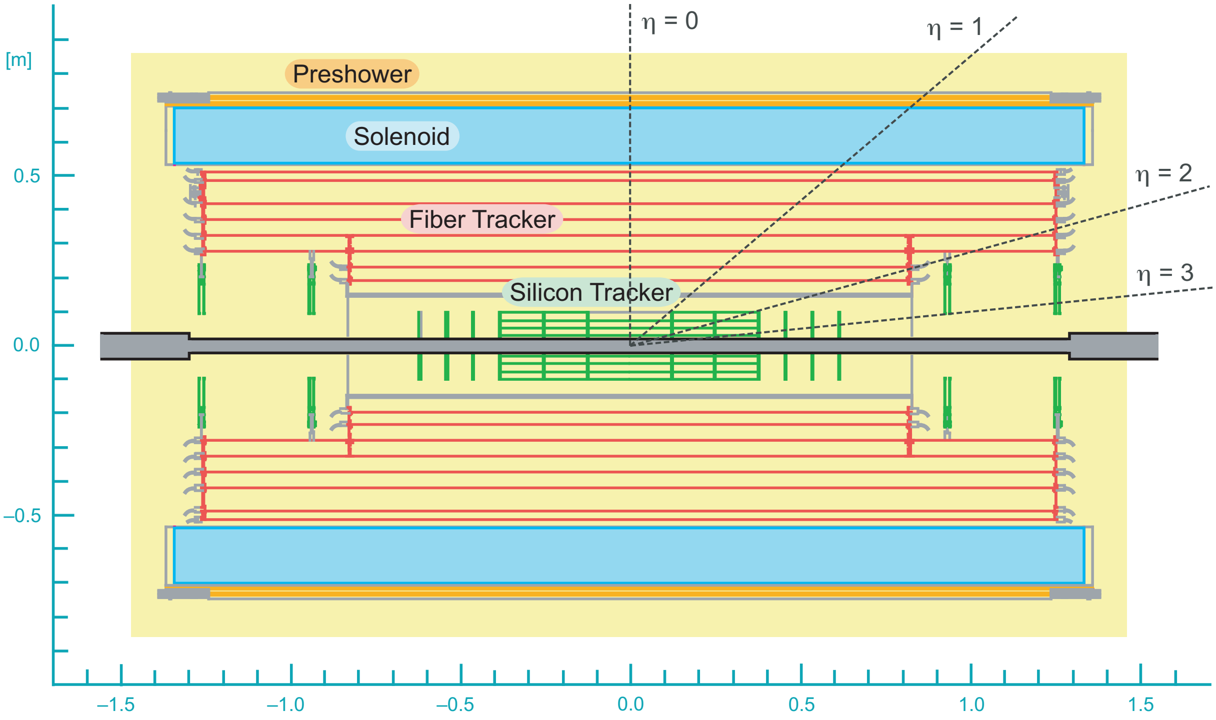

Figure 3.2. DØ Tracking Subsystem

Larger radius 'H-disks' comprising 24 wedges each are located at a $|z|$ coordinate of 100.4 and 121.0 cm extending tracking to the far forward region.The disks provide r – z and r – ϕ determination.

Inside the original barrel SMT layers, a new 'layer 0' detector with sensors at a radius 16.1 to 17.2 mm (the layer 1 SMT sensors are at 27.15mm) extends out to $|z| = 380$ mm. For tracks with a transverse momentum less than 2 GeV, the addition of layer 0 has improved our vertex resolution by greater than 20%

3.2.2.2. Fiber Tracker. Outside of the SMT in the central region ($|\eta| < 1.7$) additional tracking is provided by the Central Fiber Tracker (CFT). Comprised of 8 layers between 20 and 52 cm in the radial direction, the CFT contains 76,800 scintillating fibers grouped into alternating layers along the beam direction or at ±3 deg. The photons emitted by

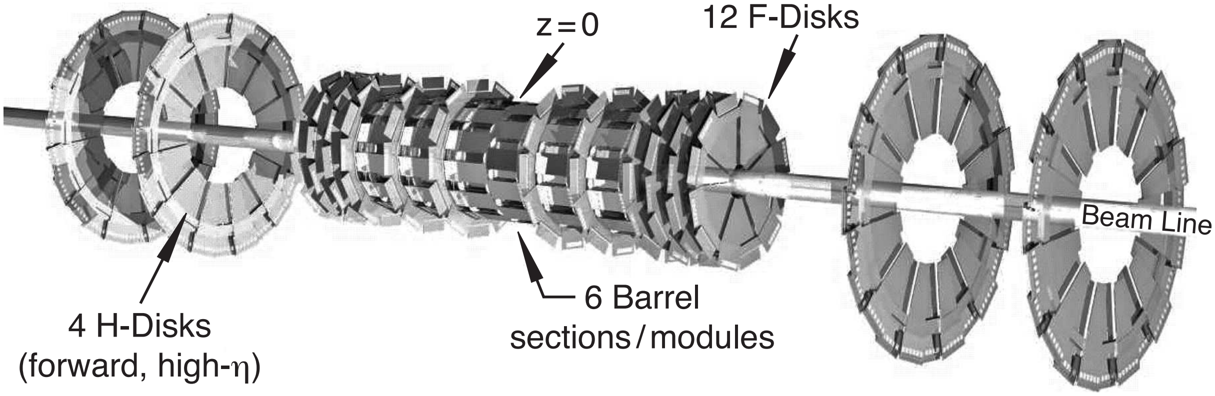

Figure 3.3. DØ Silicon Microstrip Tracker

charged particles traversing the detector are collected by high quantum efficiency photodetectors. The CFT provides 3D track reconstruction with a resolution of approximately 100 μm.

3.2.3. Solenoid and Pre-shower

The solenoid is a 2 T superconducting magnet placed just outside the CFT. It is 0.9 radiation lengths thick at normal incidence. The pre-shower detector consists of the central pre-shower (CPS) covering the region $|\eta|$ <1.3 and the forward pre-shower covering the region 1.5 $|\eta|$ < 2.5. The pre-shower was designed to help identify photons and electrons. Unfortunately the detector electronics were saturated for the RunIIa data-taking period. Although the electronics have since been replaced this analysis does not utilize any readout from either of the pre-shower detectors. Reference [**20**] focuses on the performance of the pre-shower and fiber tracker detectors for RunIIb.

3.2.4. Calorimetry System

The DØ calorimetry system consists primarily of 3 sampling calorimeter sub-detectors with layers of absorber plates sandwiching the active layers of liquid argon. A central calorimeter covers the range $|\eta| \lesssim 1$ and two end cap calorimeters(EC) extend coverage out to $|\eta| \lesssim 4$ as shown in figure 3.4. Each of the calorimeters is housed within a cryostat to keep the temperature at approximately 90 K. The first four layers of each calorimeter are referred to as the electromagnetic calorimeter or EM Cal. Photons and electrons from the interaction region are expected to lose all of their energy before escaping these layers. The remaining four (five)layers of the CC(EC) are the hadronic calorimeter and measure energy deposits due to the nuclear interactions of hadrons. As shown in figure 3.4, the hadronic calorimeter is further subdivided into fine, and course layers. The absorber plates in the EM layers are depleted uranium, in the fine hadronic layers they are a uranium-niobium alloy, and in the course hadronic layers they are copper (stainless steel) in the CC (EC). The calorimeter is divided into 5000 pseudo-projective towers of size 0.1 in η and ϕ coordinates. Figure 3.5 shows the eta and depth segmentation of the calorimeter. In general the size of individual calorimeter cells is also 0.1 in η and ϕ coordinates, the exception is layer three of the EM Cal with four cells per tower covering 0.05 in η and ϕ coordinates. This is because the calorimeter was designed for RunI when, in the absence of the solenoid, an electron at normal incidence would deposit the largest fraction of its energy at layer 3. The calorimeter cell structure is shown for reference in figure 3.6, but will not be discussed. Complete details of the calorimeters are available in reference [**18**].

The region $1.1 < |\eta| < 1.4$ covering the transition region between the CC and EC calorimeter sub-detectors has been instrumented with scintillator tiles (ICD) to aid with

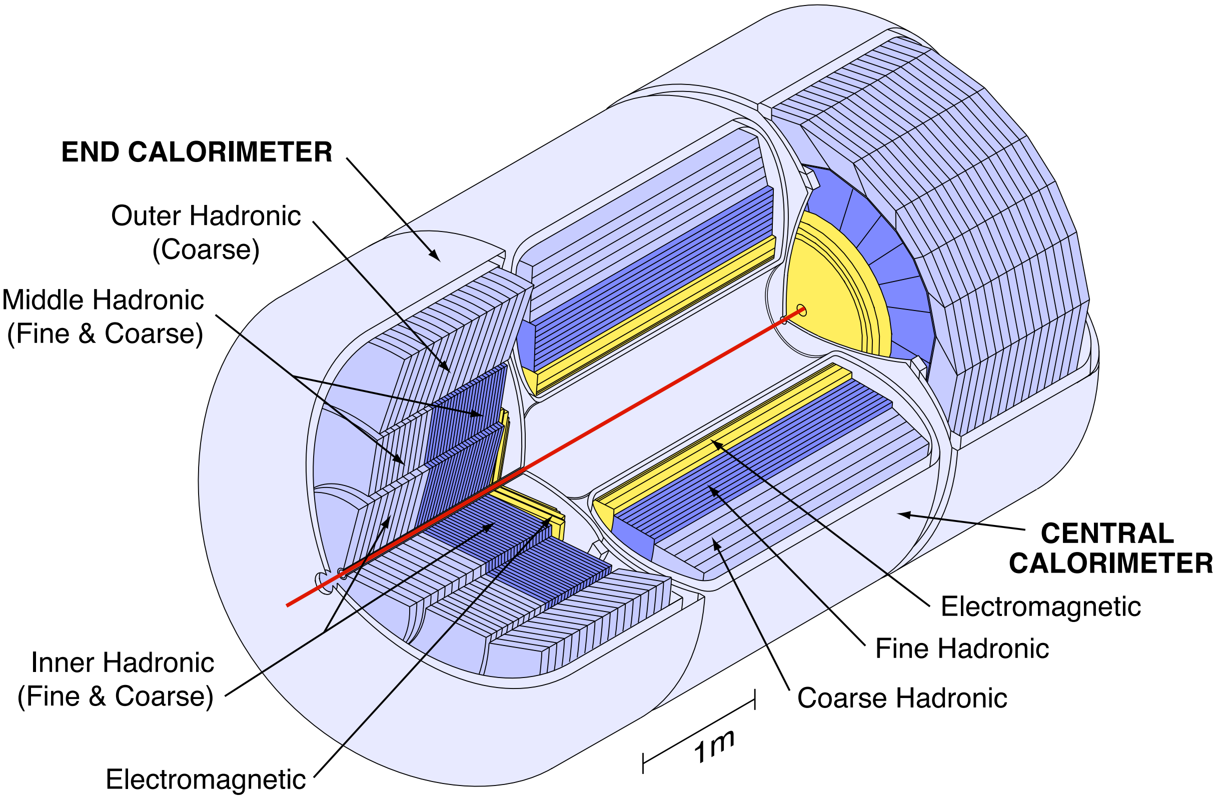

Figure 3.4. DØ Calorimeters

the degraded energy resolution in this area. As with the pre-shower detectors the ICD is not used in this analysis (with an exception for the estimation of the background).

3.2.5. Calorimeter Trigger System

The DØ trigger system has three layers of increasing complexity. The Level 1 Calorimeter triggers have been significantly upgraded for the high instantaneous luminosity environment of RunIIb. A calorimeter trigger tower (TT) consists or two adjacent calorimeter towers and spans 0.2 × 0.2 in $\eta - \phi$ space. for EM triggers the Level 1 trigger object consists of a TT, which has a large energy deposit and its neighbor with highest transverse energy. This is a change from RunIIa when the Level 1 trigger object was only

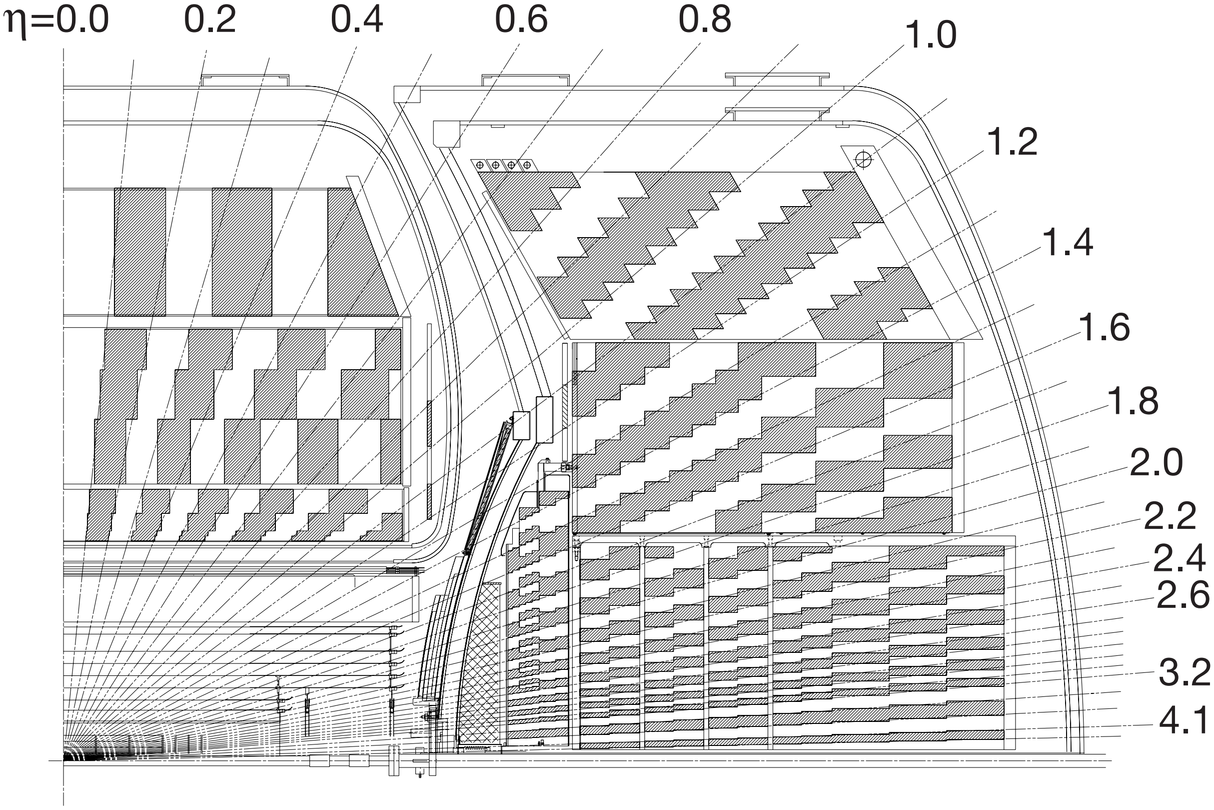

Figure 3.5. Quarter panel of the DØ calorimeter illustrating segmentation and η_{det} coverage

a simple TT. The Level 1 calorimeter trigger can make decisions based on the ratio of electromagnetic to hadronic energy, and isolation of the level 1 cal object. Reference [**21**] gives the full details of the new system.

The Level 2 and Level 3 trigger systems are unchanged from RunIIa. At Level 2 we cut on the combined energy of a seed TT and its neighbor with highest energy and evaluate its isolation compared to the remaining towers in a 3 × 3 cluster centered on the seed tower. At Level 3 decisions are based on complex shape variables of EM clusters as described in section 4.4.

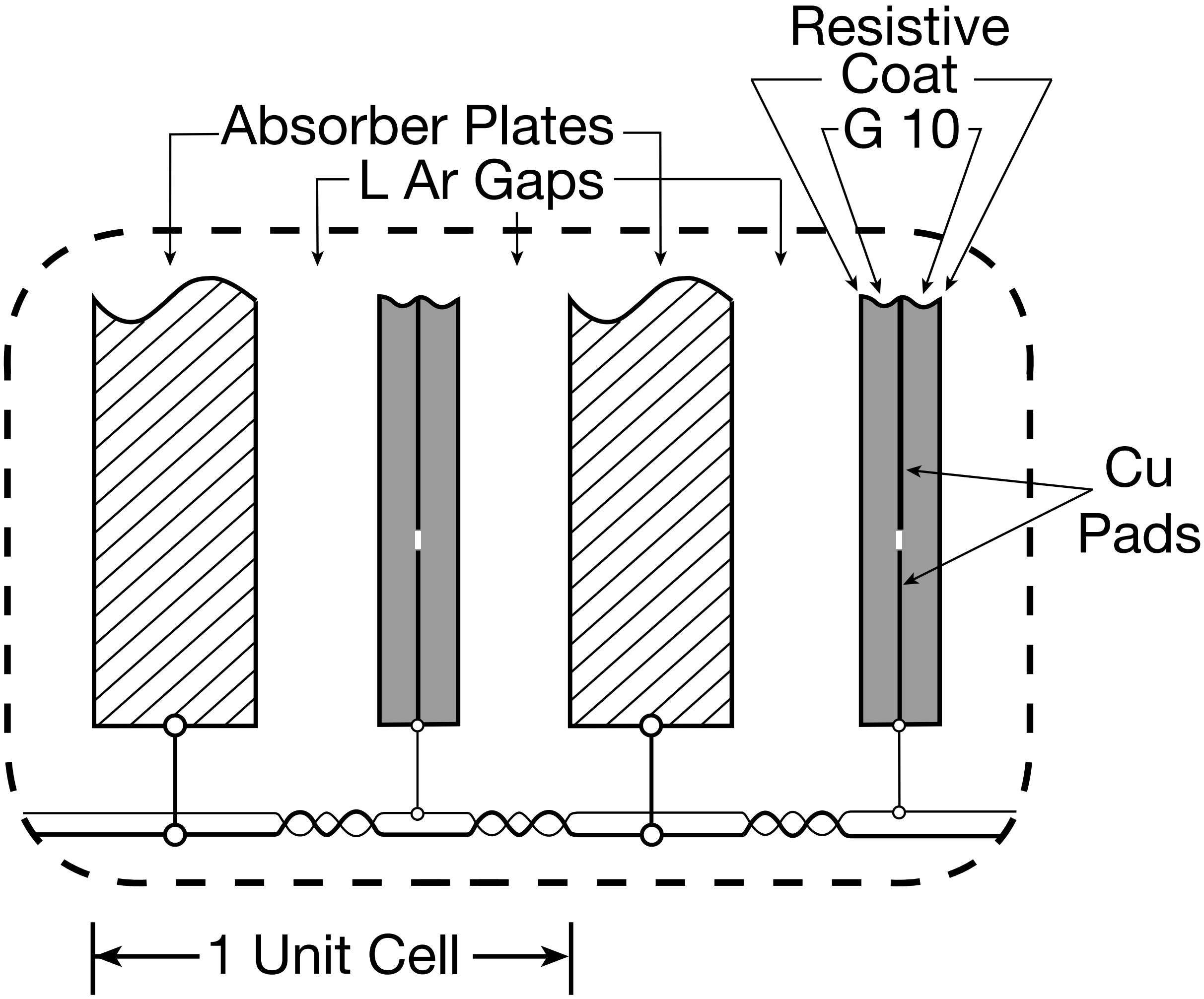

Figure 3.6. A typical DØ calorimeter cell.

3.2.6. Luminosity System

The luminosity monitor consists of 2 arrays of scintillator counters with photomultiplier tube readout located at z = ± 140 cm. covering the rapidity range $2.7 < |\eta| < 4.4$. The system measures the luminosity by counting the number of inelastic collisions for a particular bunch crossing over one minute, which are determined by a signal in both detectors in timing coincidence with a bunch crossing.

CHAPTER 4

Calorimeter Calibration and Reconstruction of Physics Objects

Our analysis is particularly sensitive to the response of the EM and hadronic calorimeter systems. In order to reduce our uncertainties and perform an accurate measurement we need to calibrate the detector. A measurement of the missing transverse energy requires that the response of the calorimeter is relatively uniform over all η and ϕ values. A measurement of the electron transverse momentum requires that the calorimeter response to electrons in the transverse momentum range concerned is well understood. The calibration takes place in multiple steps:

- Pulsar calibration of readout electronics.
- ϕ balance in rings of η from events with minimal trigger requirements.
- Energy loss corrections.
- Absolute scale based on the Z invariant mass peak.

4.1. Read Out Calibration

The initial calibration of the calorimeter electronic readout is performed using pulsers. Pulses of known charge spanning the range of the readout are injected into the electronics and then read out. A comparison of the true charge with the measured value allows one (in principle) to linearize and equalize the gains of each channel. In practice the input signal is modified by reflections off the calorimeter cells, which degrade this calibration and need to be accounted for with detailed simulations.

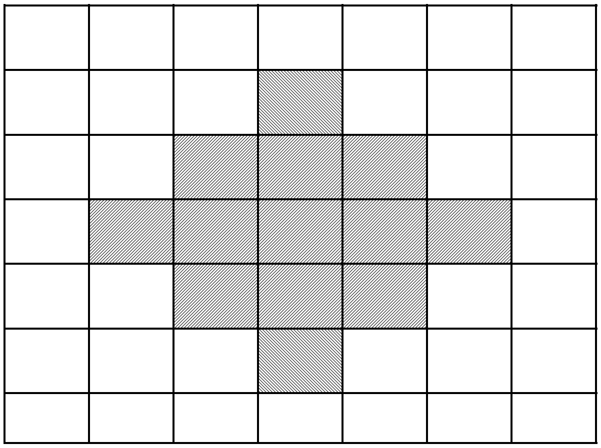

Figure 4.1. An EM Cluster in $\eta \times \phi$ Space each square signifies a tower of dimension 1×1.

4.2. EM Response Calibration

Since the Tevatron beams are unpolarized we expect the energy flux to be ϕ-independent. We exploit this to adjust the relative gains of calorimeter towers and layers in rings of ϕ at fixed η values until we see uniform occupancy above specified threshold. This procedure allows us to remove the ϕ degree of freedom from the calibration of the absolute energy scale without limiting ourselves to the small sample of reconstructed electron events available to us [**22**]. We cluster towers within a cone of radius 0.2 in $\eta \times \phi$ as shown in figure 4.1 into electromagnetic (EM) objects. The clustering algorithm requires a seed of $E_T > 500$ MeV, and the final cluster must have less than 10% of its energy deposited in the hadronic calorimeter and a final E_T greater than 1.5 GeV. The cluster should also be isolated from other calorimeter activity. The overall energy scale for an EM cluster is determined using a combination of Monte-Carlo and data studies [**3**]. The energy deposited in the active layers by an electron traversing our calorimeter is dependent on the initial energy of the

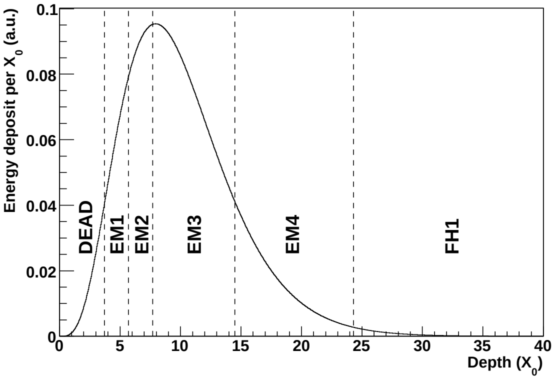

(a) $\eta = 0$

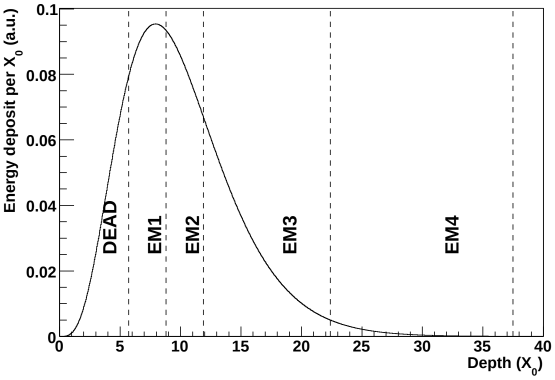

(b) $\eta = 1$

Figure 4.2. Longitudinal shower development for a 45 GeV electron at $\eta = 0$ and $\eta = 1$ Ref [**3**] using the GFLASH [**4**] simulation tool. The marked regions refer to the layers of the EM calorimeter as defined in the text.

electron and the angle of incidence (the dependence on the angle of incidence is demonstrated in figures 4.2(a) and 4.2(b)), since electrons at larger values of η will encounter more dead material before reaching the active calorimeter layers than more central electrons. By studying the response of the detector as described in the Monte-Carlo with single electron events spanning the energy and η plane, we derive correction factors as a function of η and energy, relating the energy deposited in each calorimeter layer at a given η to the total true energy of the electron. It is extremely important that the material description in our Monte-Carlo accurately describes the dead material in front of our detector in order to describe this dependence correctly. Detailed studies [**23, 24**] by the W Mass group have shown that the standard detector description in our GEANT based Monte-Carlo description of the detector does not account for all of the dead material in front of the calorimeter. The same studies show that by adding 0.16 radiation lengths of 'effective material' in the form of a copper cylinder outside the solenoid, we can recover a longitudinal shower profile as a function of η and electron energy which agrees with the data. As a final step in the calibration we compare the Z Boson Mass peak measured in data with the known value from LEP [**25**]. We fit a Voigtian (a convolution of a Breit-Wigner and a Gaussian distribution) function to the data allowing for an additional gain calibration as a function of η. This procedure effectively averages over the effects of the instantaneous luminosity on the reconstructed EM cluster energy. To keep the data size manageable the read out is zero-suppressed. This means that cells with energy below a certain threshold are not read out. These factors are taken into account in this analysis as described in chapter 6.

4.3. Reconstructed Physics Objects

4.3.0.1. Tracking and Vertex Identification. Charged particles leave hits in the SMT and CFT detectors. which are reconstructed in two stages. First track segments are created in each layer, and then these track segments are combined into tracks. A χ^2 is calculated between the track trajectory and the hits associated with the track, this χ^2 is used to determine the quality of the track. Based on initial work described in [**26**], the tracking algorithm consists of a propagator [**27**] fed into a Kalman fitter [**28**]. A vertex is the source of multiple detected tracks and indicates the position of a proton-anti-proton collision (primary vertex) or the decay of a particle (secondary vertex). A primary vertex is required to have at least three tracks with at least one hit in the SMT, which point back to a common origin. The vertex position along the beam direction (z axis) (Vtx_Z) is well described by a Gaussian convoluted with a Lorentzian and extends out to $|z|$ values greater than sixty cm., while in the x–y plane the vertex has a small spread related to the beam width. Determining the correct vertex position along the z-axis is important for an accurate calculation of the missing transverse energy in the event.

4.3.0.2. Electromagnetic Cluster. As described earlier 13 Electromagnetic Calorimeter Towers are grouped together to form an Electromagnetic cluster as shown in figure 4.1 using a simple cone algorithm with radius $\Delta R = \sqrt{\Delta\eta^2 + \Delta\phi^2} = 0.2$ centered on the tower of maximum energy. In the absence of a track pointing towards a reconstructed cluster the position is determined using the primary vertex and centroid of the cluster, however if possible the θ and ϕ positions of the cluster are given by a track which points towards the ΔR cone of the EM cluster. In order to separate electrons and photons from π^0's or other hadrons, which may have deposited energy in the calorimeter, we apply additional criteria to the EM Cluster based on how deeply into the calorimeter the shower progressed ($frac_{EM}$), how isolated the shower cluster is from other energy deposits (f_{Iso}), and a shower shape requirement (HMatrix). The $frac_{EM}$ variable is the ratio of the total energy deposited in the EM layers of the cluster towers to the energy in the EM layers and the first layer of the hadronic calorimeter. Isolation is defined as:

$$f_{Iso} = \frac{E(R < 0.4) + E_{EM}(R < 0.2)}{E_{EM}(R < 0.2)}, \tag{4.1}$$

where E is the total energy in the calorimeter and E_{EM} is the energy deposited in the EM layers only. The shower shape variable (HMatrix7) is the inverse of the covariance matrix comparing seven EM cluster shape variables to the eigenvector values determined for electrons in Monte Carlo. The variables concerned are:

- EM fraction in each of the 4 EM layers,
- the width of the shower in the ϕ direction,
- the energy, and
- Vtx_Z.

To determine whether a track and an EM cluster are matched we use a spatial χ^2 between the cluster centroid and the track direction extrapolated to layer 3 of the calorimeter:

$$\chi^2 = \left(\frac{\Delta z}{\sigma_z}\right)^2 + \left(\frac{\Delta\phi}{\sigma_\phi}\right)^2, \tag{4.2}$$

4.3.1. Recoil

The transverse recoil vector $\vec{u}_T$ is the vector sum of the transverse energy of unsuppressed calorimeter cells which are not included in the leading (W boson event candidates) or leading and sub-leading (Z boson event candidates) EM clusters. The $\vec{u}_T$ variable may include contributions from spectator quarks and multiple interactions in addition to the actual recoil against the vector boson. Cells in the ICD region are not included in the sum.

4.3.2. Missing Transverse Energy ($M\vec{E}T$)

The $M\vec{E}T$ is defined as:

$$M\vec{E}T = -\vec{p}_T^{\,e} - \vec{u}_T \tag{4.3}$$

It is a proxy for the transverse energy carried away by the neutrino and is a useful cut for removing backgrounds from the W candidate event sample. Fake sources of MET include the misidentification of a QCD jet as an EM Object resulting in an incorrect energy scale application, and the loss of energy into an inactive volume of the detector.

4.3.3. Scalar Transverse Energy (SET)

SET is the scalar sum of all non-zero suppressed cells in the calorimeter, except those which are in towers associated with an EM cluster, and gives us a handle of the overall energy of the event. We see that the tracking efficiency is strongly dependent on SET which needs to be modeled accurately.

4.4. Analysis Cuts

Primary Vertex requirement:

- $\mid Vtx_Z \mid< 60$ cm.

Electron requirements:

- An EM object clustered with the simple cone algorithm, $frac_{EM} > 0.9$, $f_{iso} < 0.15$.
- $|\eta_{det}| < 1.05$.
- HMatrix7 < 12,

- The EM cluster should not be close to the edge of a calorimeter module (fiducial cuts),
- $p_T > 25$ GeV, and
- Spatial track match probability greater than 0.01 with a hit in the SMT.

$Z \to ee$ requirements:

- Two electrons which pass the cuts listed above.
- At least one electron passes trigger requirements (L1/L2/L3).
- Both electrons have good matched tracks.
- Electron $|\eta_{det}| < 1.05$.
- $|\vec{u}_T| < 15$ GeV.
- $70 < m_{ee} < 110$ GeV.

Where m_{ee} is the invariant mass of the two electrons $W \to e\nu$ requirements:

- One electron which passes the cuts listed above.
- The electron must pass trigger requirements (L1/L2/L3).
- The electron must have a good matched track.
- Electron $|\eta_{det}| < 1.05$.
- $|\vec{u}_T^{rec}| < 15$ GeV.
- $50 < m_T < 200$ GeV.

The fiducial cuts are applied based on the position as determined from the matched track. This is important because the response of a calorimeter tower varies strongly with the position of the EM cluster with respect to cracks in the ϕ direction, and the cluster position is biased towards the center of the module as shown in figure 4.3. The degradation of the calorimeter response is due to energy that would normally be deposited in active layers of

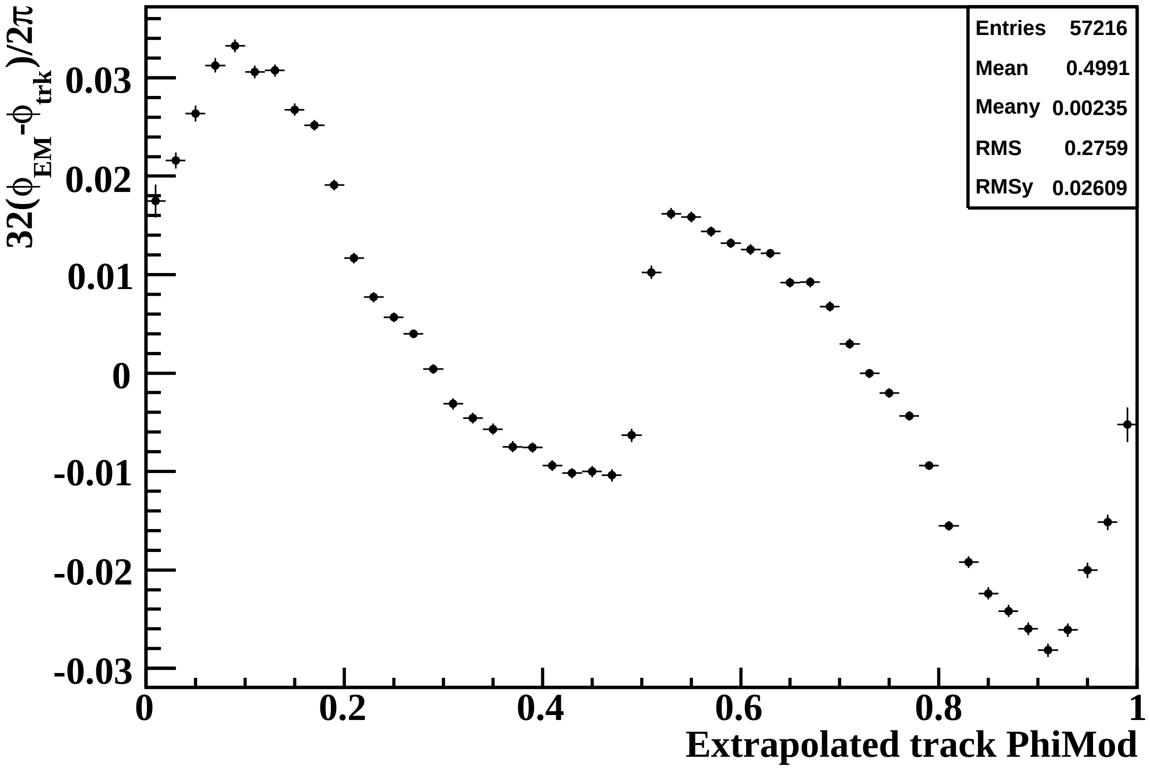

Figure 4.3. Shift in EM Cluster ϕ position in a module compared to the position from the tracking system as function of the position from the tracking system.

the calorimeter, being deposited in the cracks between the modules. The variable Phimod is the remainder of the mathematical operation:

$$\frac{32\phi}{2\pi} \div 1.0 \tag{4.4}$$

$0 \leq$ Phimod ≤ 1 for any ϕ module is a measure of the ϕ position within the module. We use events in the range $0.1 <$ Phimod < 0.9.

4.5. Trigger Requirements

The data have been collected with 2 distinct trigger list sets (v15 and v16). During the period of data collection with the v15 trigger list we use an unprescaled EM trigger with a level 3 p_T cut at 25 GeV. Due to the higher instantaneous luminosities delivered by the Tevatron as RunIIb progressed, we used two triggers from v16. At high instantaneous luminosities at the beginning of a store we used a prescaled EM trigger with a level 3 p_T cut at 27 GeV. This was necessary to reduce QCD background while keeping the trigger rates at an acceptable level. When the luminosity in a store has decreased enough to allow it we switch back to an unprescaled EM trigger with a level 3 p_T cut at 25 GeV. The detailed requirements for each trigger are level 1, level 2 and level 3 are listed in table 4.1.

Trigger	L1	L2	L3
E1_SHT25	$E_T > 19$ GeV	$E_T > 22$ GeV or $E_T > 19$ GeV and Isolation	$E_T > 25$ GeV and shower shape requirements
E1_SHT25 (v16)	$E_T > 19$ GeV	$E_T > 25$ GeV or $E_T > 19$ GeV and likelihood	$E_T > 25$ GeV cut and shower shape requirements
E1_SHT27	$E_T > 19$ GeV	$E_T > 25$ GeV or $E_T > 19$ GeV and likelihood	$E_T > 27$ GeV cut and shower shape requirements

Table 4.1. Single EM triggers.

The instantaneous luminosity distribution of our total data sample broken down by trigger is shown in figure 4.4. This corresponds to 4.35 fb^{-1} of integrated luminosity collected between the ninth of June 2006 and the thirteenth of June 2009, with 1.65 fb^{-1} collected with the v15 trigger list. The corresponding distribution for RunIIa is shown in figure 4.5. After our analysis cuts we are left with Z and W boson candidate yields

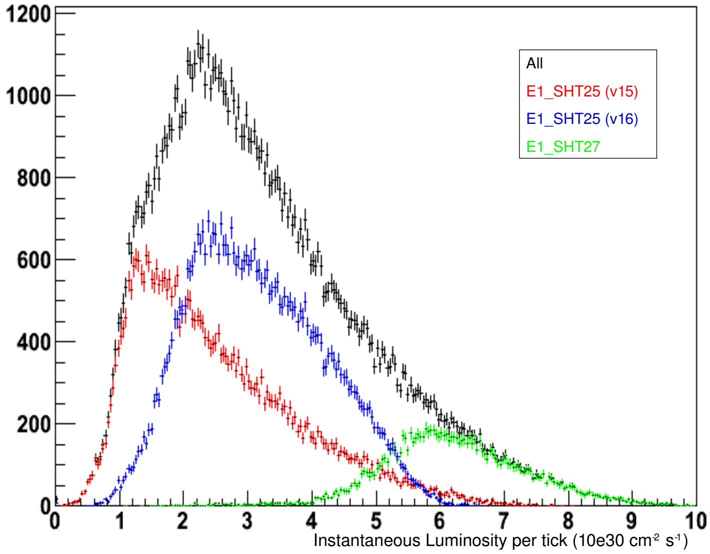

Figure 4.4. The number of events in our Z candidate sample as function of instantaneous luminosity separated by trigger.

of 54,508 and 1,677,489 events respectively. The invariant mass, and transverse mass distributions are shown in figures 4.6 and 4.7

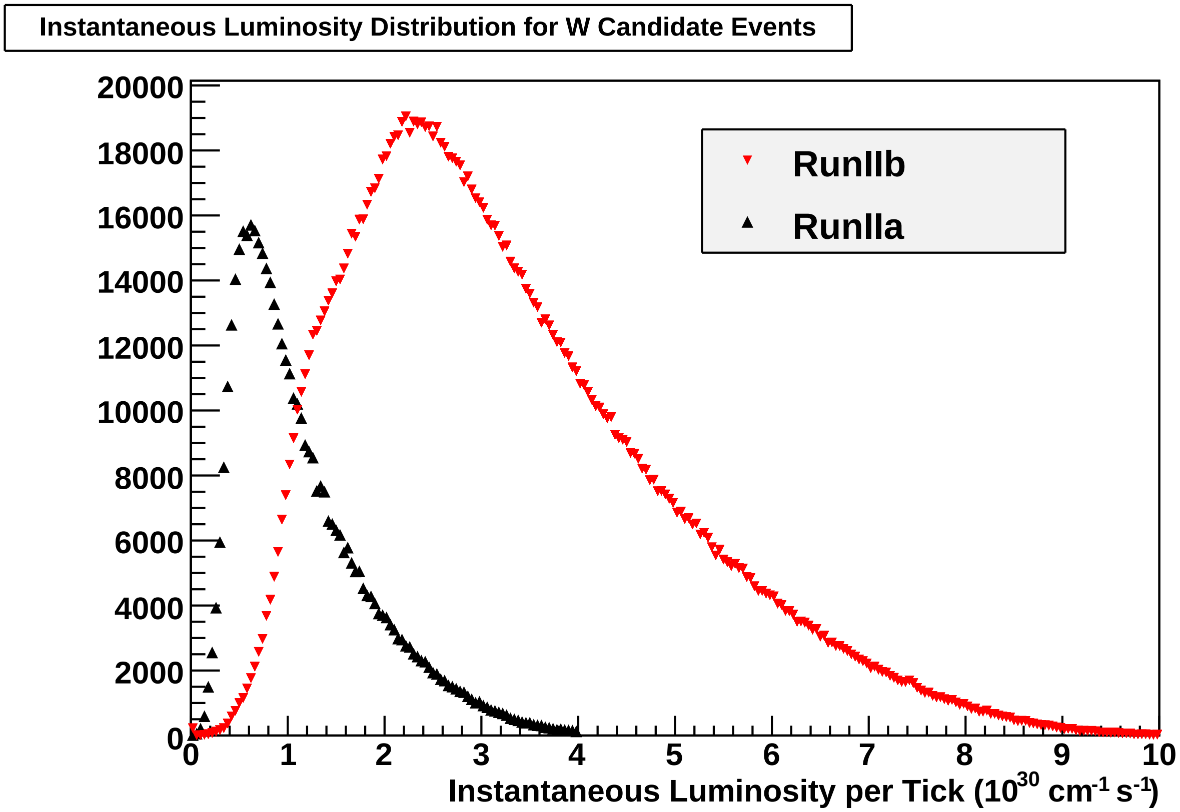

Figure 4.5. Instantaneous luminosity distribution from the RunIIa and RunIIb W Boson Candidates.

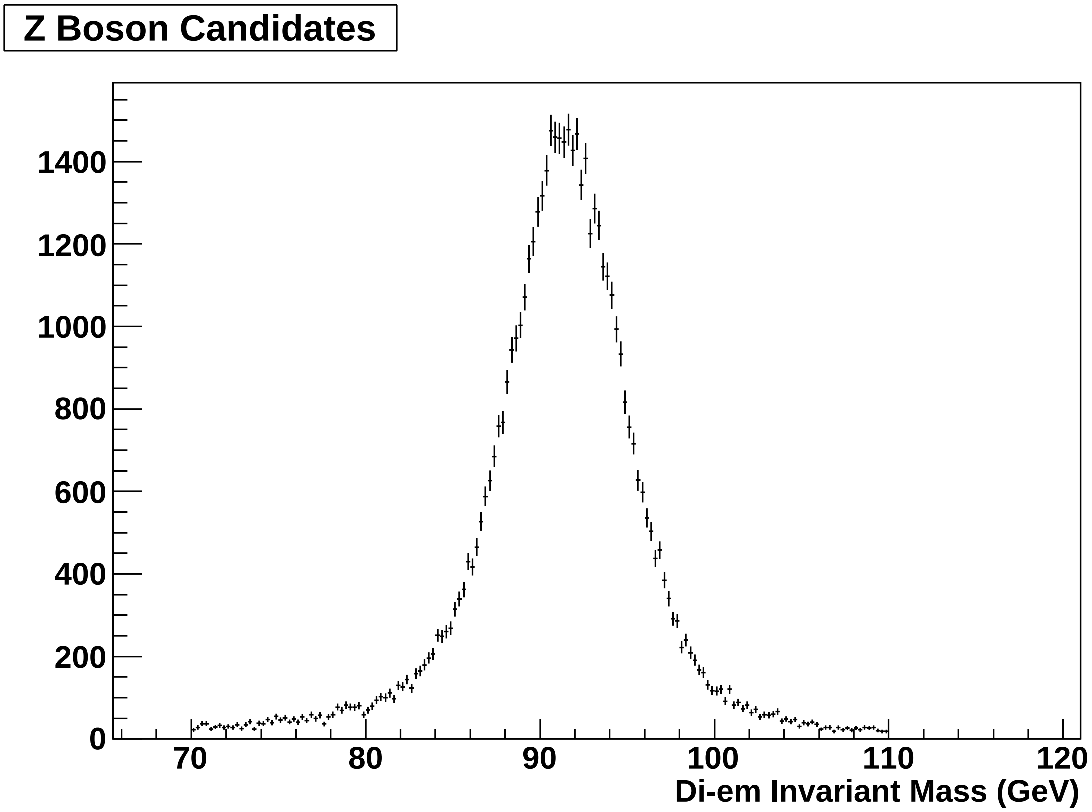

Figure 4.6. Z boson invariant mass distribution for RunIIb.

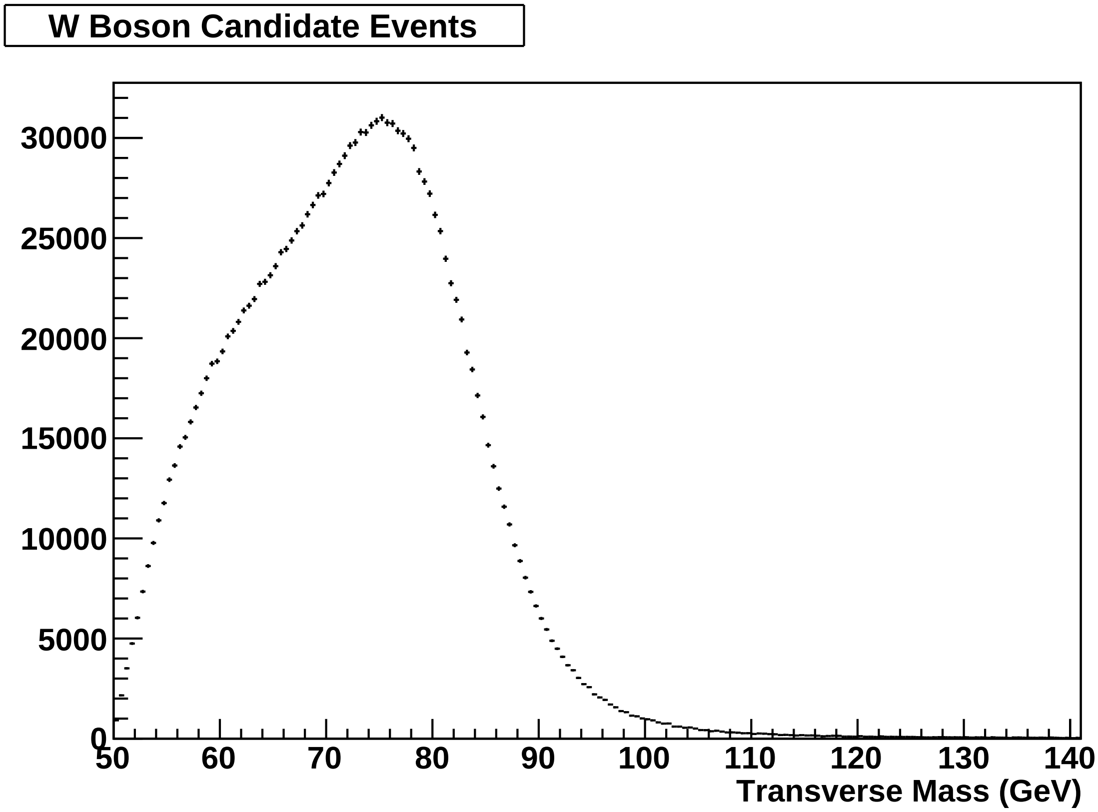

Figure 4.7. Transverse mass distribution of W boson candidate events.

CHAPTER 5

Analysis Strategy and Description

We will determine the W boson mass using a template fit method. We fit templates of the transverse mass distribution generated over a range of possible W boson Mass values to the data by finding the template (and hence the mass), which has the maximum likelihood of agreement with the data. This method depends on having a realistic model for event generation as well as the ability to reproduce the detector response for our selection cuts with enough accuracy to be able to faithfully describe the final distributions obtained when studying the data. We use the ResBos [**29, 8, 30, 31, 32, 14, 33**] Monte Carlo event generator to produce and decay the vector bosons. ResBos uses parton distribution functions from the CTEQ collaboration [**34, 10**].While Resbos does not include final state radiation from the electron, which we use Photos [**35**] to simulate, it includes NLO perturbative calculations of fully differential cross-sections at high boson transverse momentum as well as a re-summed calculation for the low transverse momentum cross-section providing a consistent description of boson production over the range of interest. ResBos does not include a model of the hadronic interaction, which we simulate using specialy selected events from our data. We also use Pythia version 6.323 [**36**] for additional studies as described later. In addition to an accurate description of W Boson events we also require an accurate description of Z Boson events, which will be used as a standard candle to tune our simulation. The analysis proceeds along the lines previously described in references [**23, 24**] and [**9**]. In addition to the increased precision required to describe four times as much data when compared to reference [**9**], we are faced with additional challenges due to the increased instantaneous luminosity. Following the precedent of previous analyses, in order to reduce bias from experimenters who have an expectation of the value of m_W the numerical value of the result of our fits to m_W is blinded, that is the result returned from the fit program has an unknown offset from the true fitted value. We will remove the blinding offset once we are satisfied that our comparison plots indicate that we have a good description of the data.

5.1. Event Generation

Although the CTEQ collaboration has released their version 6.6 PDF set [**10**], which include updated parameterizations, and heavy quark distributions, the analysis still partially relies upon the version 6.1 PDF set [**34**] (particularly for Pythia based studies). The CTEQ collaboration determines the parton distribution functions for the proton from global fits to a large range of data. The fit is performed in a space of 20 orthogonal vectors, and along with the central value function includes additional PDF sets, which correspond to variations in the positive and negative direction along each eigenvector corresponding to the 90% uncertainty interval. CTEQ 6.1 contains one function for the gluon distribution, and 6 other functions for quark and anti-quark distributions (the s and c quark distributions are assumed to be the same as the $\bar{s}$ and $\bar{c}$ distributions respectively) and is fit in a space of 20 eigenvectors. The CTEQ 6.6 set includes improved fits and parameterizations, and allows for the strange quark distribution to be independent of the other sea quark distributions. CTEQ 6.6 has 22 degrees of freedom, and 44 error sets, which describe variations from the optimal fit. ResBos computes fully differential production cross-sections of Z and W bosons for the process $p\bar{p} \rightarrow (V- > ll)X$ at next-to-leading order (NLO) in perturbation theory where V denotes either a W or Z boson, l is a lepton, and X represents QCD recoil. ResBos does not include any description of spectator quarks, additional interactions or final state radiation. Photos includes the effects of photon radiation from the final state leptons. The Z boson p_T and rapidity distributions from Resbos+Photos have been shown to be in good agreement with Z boson Data [**37**]. Pythia describes the same process at Resbos (as well as many others) at leading order, however Pythia also includes a description of the underlying event and multiple interactions presenting a controlled environment which is similar to that found in the data allowing us to study the effect of these components on our analysis. ZGRad2 (available at http://ubhex.physics.buffalo.edu/ baur/) has been used to estimate the uncertainty due to the model of final state radiation.

5.2. Detector Simulation

Our fast Monte-Carlo detector simulation would ideally be optimized to describe the kinematic range of electrons from W Boson decays. For this reason we calibrate based on the clean sample of kinematically similar electrons we obtain from the decay of Z bosons. Unfortunately the cross section for Z boson production is a factor of ten lower than for W boson production limiting the precisions of our simulation. The requirement that we must identify both decay products from the Z boson while being unable to limit the acceptance of the neutrino from W boson decay adds to the intrinsic difference between W and Z boson event kinematics. The starting point for our simulation is a model of the electron response incorporating the EM resolution, scale and offset. We add to this the effects of zero suppression and the underlying energy reconstructed in the electron cluster which is uncorrelated with the true electron energy, this underlying energy is based on the interaction between the electron and the hard recoil system and the energy due to the underlying event. The recoil simulation is the conglomeration of many components modeled independently:

- The QCD recoil against the Boson.
- The component due to the breakup of the incoming hadrons involved in the Hard Scatter (minimum bias component).
- The component due to additional hadronic interactions in the same beam crossing and electronic noise (zero bias component).
- Leakage of energy from the electron out of the electron cone.
- Final state radiation from the lepton, which is not reconstructed as part of the EM cluster.

5.3. The Template Fit Method

Once we have a set of templates, each representative of the transverse mass distribution for a given value of the mass of the W boson we fit for the most compatible value to the data using a binned negative log likelihood technique. The likelihood L is calculated as:

$$L = \prod_{i=1}^{N} \frac{e^{-m_i} m_i^{n_i}}{n_i!}, \tag{5.1}$$

where N is the number of bins. n_i is the number of events observed in bin i and m_i is the number of events in the template histogram. We are performing a shape analysis so the templates are normalised to the data sample. The number of events in any given template is at least two orders of magnitude greater than in our data sample, ensuring that the only statistical fluctuations we are sensitive to are those in our limited data sample. We minimize $-\ln L$ in order to determine the parameter in our fit. The $\pm 1\sigma$ uncertainty is determined as the values which increase $-\ln L$ by 0.5. We use the template fit to determine parameters in our model as well as for the final determination of the W boson mass.

CHAPTER 6

Simulation of Detector Response

We simulate the detector response (and resolution) in three categories. The response to electrons, the response to the recoil system, and the efficiencies for events to pass our selection requirements.

6.1. EM Response and Resolution

This section describes the response of the detector to electrons, as implemented in our fast Monte-Carlo simulation.

6.1.1. EM Resolution

We use the same energy resolution function as was derived in the RunIIa W Mass analysis [**9**].Specifically:

$$\frac{\sigma_{EM}(E)}{E} = \sqrt{C_{EM}^2 + \frac{S_{EM}^2}{E} + \frac{N_{EM}^2}{E^2}} \tag{6.1}$$

where

$$S_{EM} = (S_1 + \frac{S_2}{\sqrt{E}}) \times \frac{e^{S_{exp}/\sin\theta}}{e^{S_{exp}}} \tag{6.2}$$

with

$$S_{exp} = S_3 - S_4/E - S_5^2/E^2. \tag{6.3}$$

where C_{EM}, S_{EM} and N_{EM} are the constant, sampling and noise terms, S_1, S_2, S_3, S_4, S_5 and S_{exp} are constants, and E is the energy of the electron in GeV respectively. The term involving N_{EM} accounts for effects due to electronic readout noise, and radiactivity from the Uranium absorber plates and is negligible at the values of E which concern us ($E > 25\ GeV$), and the term in volving C_{EM} accounts for non-uniformities in the response of the calorimeter. S_{EM} is usually a constant, and the term in equation 6.1 accounts for the loss of resolutiion due to the sampling nature of the calorimeter. We find that due to the large amount of dead material in front of our calorimeter and the fact that the amount of dead material varies as a function of η we need to introduce this unusual parameterization of S_{EM} in order to describe our data. All parameters except the C_{EM} term, which is determined by a fit to the data, are derived from detailed Monte-Carlo studies. The exact values of these parameters are sensitive to the number of radiation lengths of material traversed before the active calorimeter layers, and our ability to derive the correct values for data was enabled by the studies described in Chapter 4 which allowed us to determine the amount of material in front of the calorimeter. The constant term is derived from a template fit of our fast Monte-Carlo output to the data, and we find a value of $C_{EM} = 0.0198 \pm 0.0006$, which is in agreement with the RunIIa analysis value of 0.0204 ± 0.0013 The negative log(likelihood) curve is shown in figure 6.1, and the comparison to the two EM invariant mass from data after the EM calibration is shown in figure 6.2.

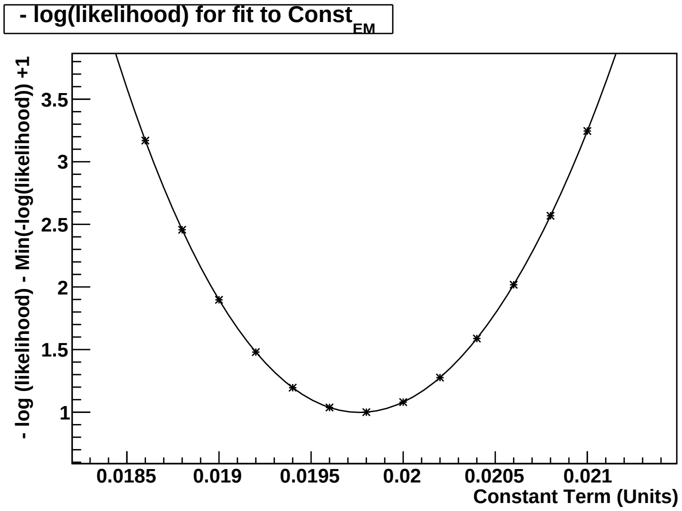

Figure 6.1. Negative log(likelihood) plot from used to determine C_{EM}. The absolute values on the y-axis are arbitrary.

6.1.2. EM Response

In the absence of effects correlated with the recoil system which will be discussed later the observed energy for an electron in a calorimeter can be related to the true energy by equation 6.4.

$$E_{\text{obs}} = \alpha^0_{EM} E_{\text{true}} + \beta^0_{EM}. \tag{6.4}$$

We determine α^0_{EM} and β^0_{EM} from a binned log likelihood fit to Z boson data. The Z boson invariant mass may be expressed as:

$$M_Z^2 = 2E(e_1)E(e_2)(1 - \cos\theta), \tag{6.5}$$

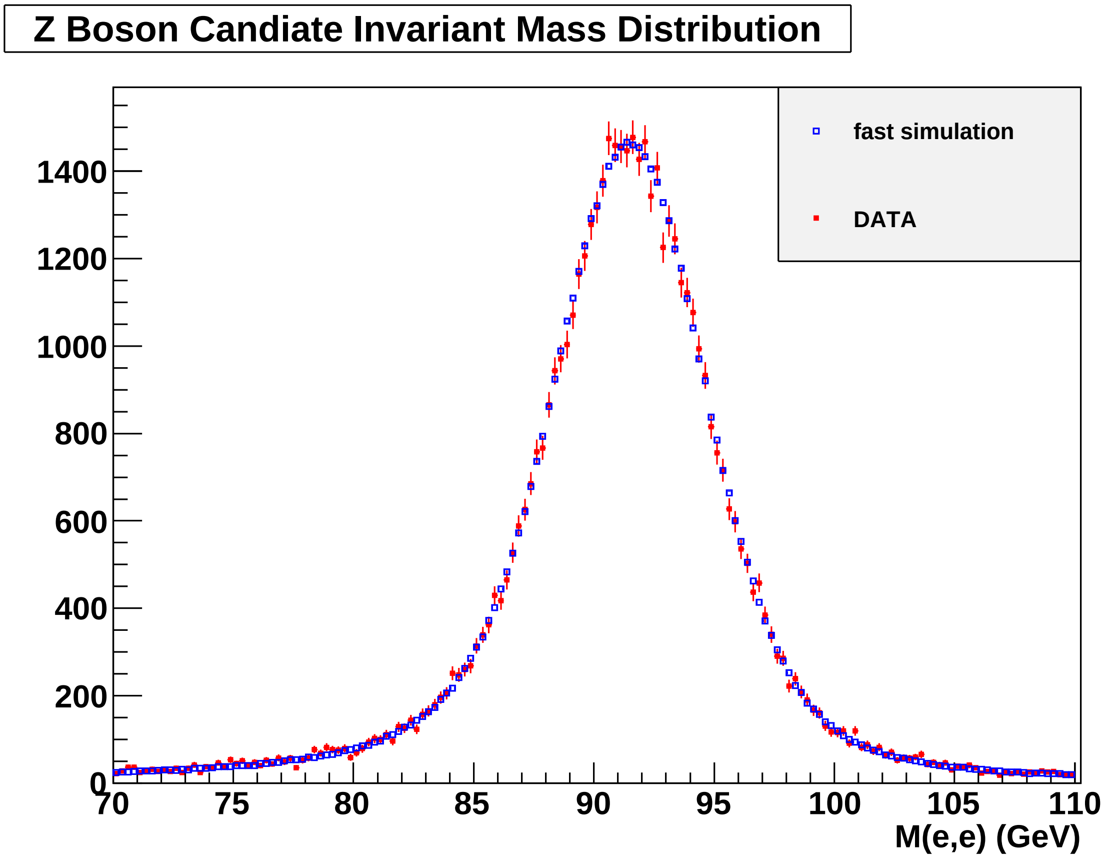

Figure 6.2. Comparison of the Z boson invariant mass peak from fast Monte-Carlo to the Z boson candidate invariant mass peak from data. $\chi^2/NDF = 161.6/160$.

where θ is the angle between the electrons, which, when combined with equation 6.4 may be written as:

$$M_{\text{obs.}}(Z) = \alpha^0_{EM} M_{\text{true}}(Z) + \beta^0_{EM} f_Z^{\text{true}} + \mathcal{O}((\beta^0_{EM})^2), \tag{6.6}$$

where f_Z^{true} is defined as:

$$f_Z^{true} = \frac{E_{\text{true}}(e_1) + E_{\text{true}}(e_2)}{M_{\text{true}}(Z)}(1 - \cos\theta), \tag{6.7}$$

and $E_{\text{true}}(e_1)$ and $E_{\text{true}}(e_2)$ are the true energies of the two electrons, $M_{\text{true}}(Z)$ is the true Z mass, $M_{\text{obs.}}(Z)$ is the observed Z mass, and θ is the true opening angle between the electrons, which due to the superior resolution on angular position than energy is adequately described by the detected opening angle. For small offsets f_Z^{true} may be approximated by $f_Z^{\text{obs.}}$. A template fit to this two dimensional distribution (shown in figure 6.3) which involves making templates of the f_Z vs. m_Z distribution as functions of α^0_{EM} and β^0_{EM} which we compare to the distribution from data, allows us to determine α^0_{EM} and β^0_{EM}. An in depth study of this method for determining the scale and offset is available at reference [**38**]. In order to reduce the correlation between α^0_{EM} and β^0_{EM} we parameterize the electron response as:

$$E_{\text{obs.}} - E_{\text{mean}} = \alpha_{EM}(E_{\text{true}} - E_{\text{mean}}) + \beta_{EM} \tag{6.8}$$

and fit for α_{EM} and β_{EM}. Where we choose $E_{\text{Mean}} = 43\ GeV$. For our data sample we find $\alpha_{EM} = 1.0162 \pm 0.0019$ and $\beta_{EM} = 0.0706 \pm 0.0144\ GeV$ with a correlation factor of -0.769. The 1 σ uncertainty contour on the parameters is shown in figure 6.4. The deviation of the semi-major axis from the horizontal is representative of the correlation between the parameters. Figure 6.3 shows the m_Z vs. f_Z distribution from data, and figure 6.2 shows the comparison to the Z boson candidate invariant mass distribution in the data after the determination of α_{EM}, β_{EM} and the term C_{EM} described in the previous section.

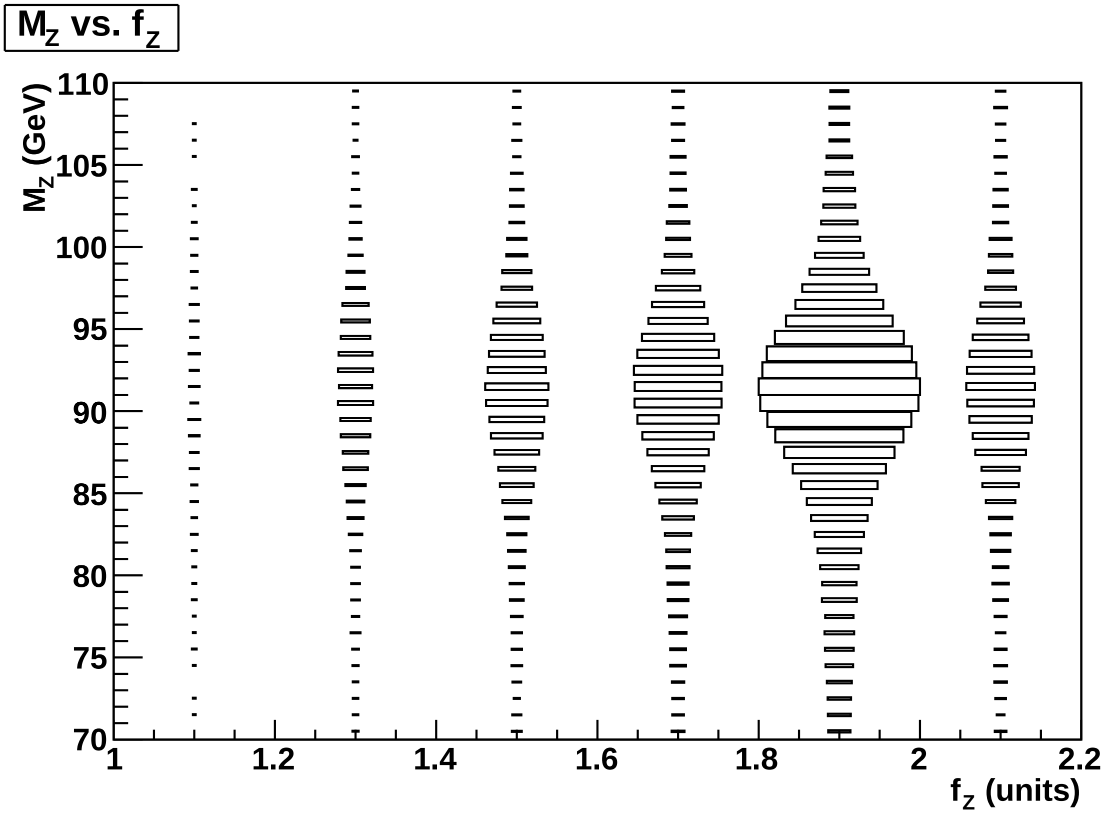

Figure 6.3. m_Z vs. f_Z used to determine α_{EM} and β_{EM}.

6.2. Hadronic Response

The transverse momentum of the hadronic recoil $\vec{u}_T$ is modeled as the sum of individual components from different sources:

$$\vec{u}_T = \vec{u}_T^{\,\mathrm{HARD}} + \vec{u}_T^{\,\mathrm{MB}} + \vec{u}_T^{\,\mathrm{ZB}} + \vec{u}_T^{\,\mathrm{UPARA}} + \vec{u}_T^{\,\mathrm{PHOTON}}$$

where each of the individual terms above are described in detail below.

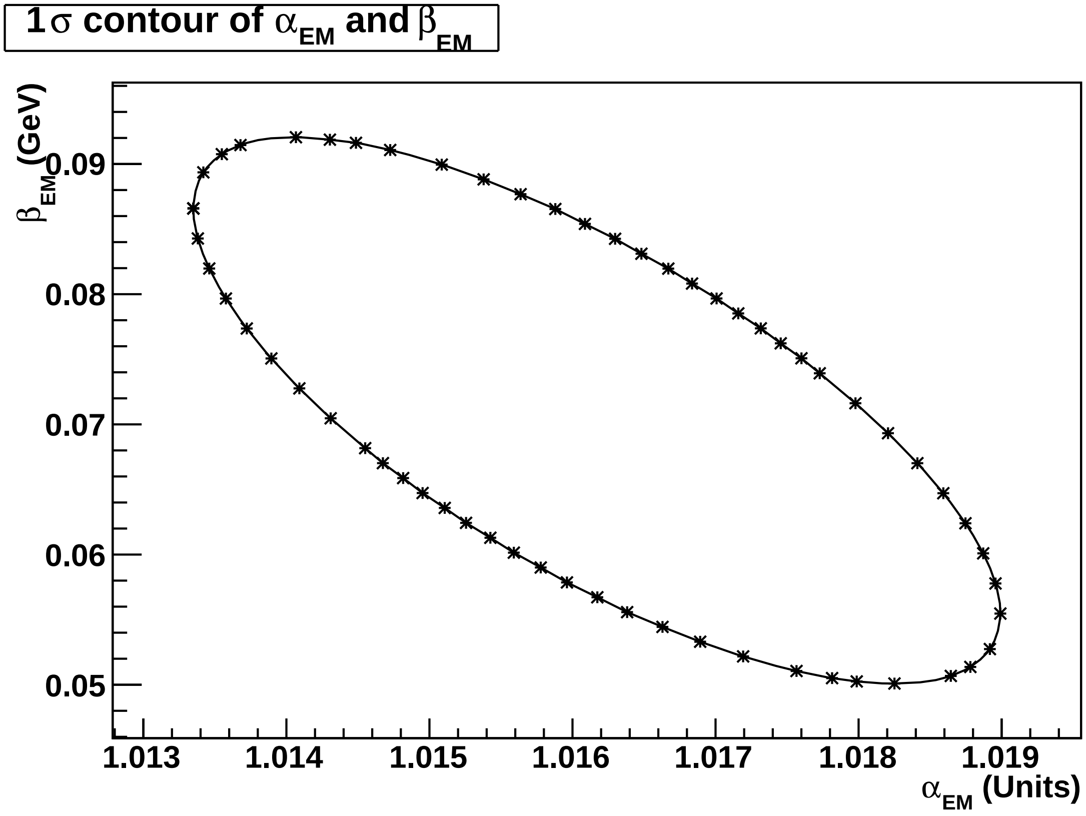

Figure 6.4. 1 σ contour on the fit of the scale and offset parameters to the Z boson invariant mass peak, as described in the text.

6.2.1. Hard Recoil Smearing ($\vec{u}_T^{\,\mathrm{HARD}}$)

This describes the smearing of the hard scatter recoil against the boson, which balances the boson transverse momentum.

$$\vec{u}_T^{\,\mathrm{HARD}} = \vec{f}(\vec{q}_T) \tag{6.9}$$

where q_T is the transverse momentum transfer for the event. The response is determined from studies of Pythia $Z \to \nu\nu$ events in our GEANT based Monte-Carlo and is described in detail in reference [**5**]. The neutrinos escape the system undetected leaving us with a clean 'Hard Recoil' to study. Our model has to account for correlations between the magnitude of the recoil vector and the azimuthal angle ϕ. By studying this sample we determine a parameterization for the hadronic response of our detector which we use to realistically smear the hard recoil provided by our event generator. The following variables are used for the parameterization :

- $R_{rec} = \frac{q_T - u_T}{q_T}$ — recoil p_T resolution ($R < 1$),
- $\Delta\phi = \phi(\vec{u}_T) - \phi(\vec{q}_T)$ — recoil angular resolution ($|\Delta\phi| < \pi$),
- $Resp = \frac{u_T}{q_T}$ — recoil response,
- $Resp_{prj} = \frac{\vec{u}_T \cdot \vec{q}_T}{q_T}$ — projected recoil response.

Where u_T (q_T) is the magnitude of $\vec{u}_T$ ($\vec{q}_T$). Two-dimensional distributions of the p_T resolution versus the ϕ resolution are plotted for 32 bins of true p_T from 0 to 100 GeV as shown in figure 6.5 for the bin of $4.5 <$ (true) $p_T < 5$. These distributions are fit with the function shown below:

$$pdf(x,y) = p_0 \exp\left[-\frac{1}{2}\left(\frac{x-\mu(y)}{\sigma_x(x,y)}\right)^2\right] \exp\left[-\frac{1}{2}\left(\frac{y}{\sigma_y(y)}\right)^2\right],$$

where: $x \equiv R_{rec}, \;\; y \equiv \Delta\phi\,[rad], \;\; \mu(y) = p_1 + p_2 \cdot y,$

$$\sigma_x(x,y) = \begin{cases} p_3, & x < \mu(y) \\ p_4, & x > \mu(y) \end{cases}, \; \sigma_y(y) = p_5 + p_2 \cdot y$$

and p_0 through p_5 are parameters of the fit used to describe R_{rec} and $\delta\phi$ for each bin of true recoil transverse momentum. These functions allow us to realistically simulate the u_T and ϕ response and resolution of the hard recoil in our fast Monte-Carlo simulation.

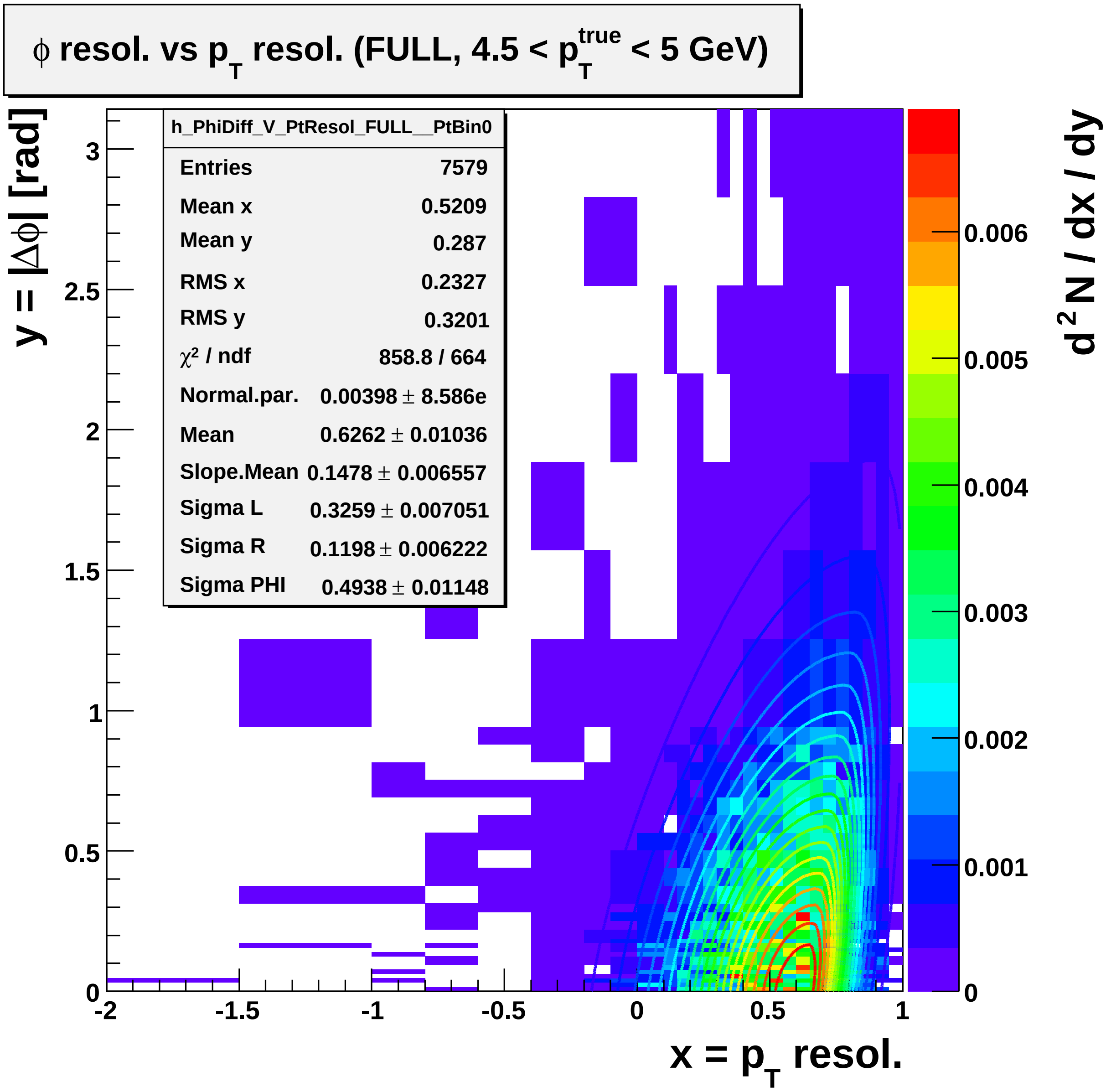

Figure 6.5. The 2-D distribution of the recoil p_T- and ϕ resolutions for: FULL MC (boxes) and fit (contours) for $q_T \in [4.5, 5]\,GeV$.

6.2.2. Soft Recoil Smearing ($\vec{u}_T^{\,\mathrm{MB}}$ and $\vec{u}_T^{\,\mathrm{ZB}}$)

The soft recoil describes energy in the event from source other than the leading order hard interaction responsible for boson production. This includes contributions from the remnant of the proton and anti proton involved in the hard scatter, additional interactions between protons and anti-protons from the current (or previous) beam crossing(s) and detector noise. The catchall term 'detector noise' includes energy from beam related backgrounds, uranium decays and electronic readout noise. We model these contributions as the vector sum of two contributions,

- $\vec{U_T}^{\text{ MB}}$ – the minimum bias piece which describes the energy from the proton and anti-proton remnants, and
- $\vec{U_T}^{\text{ ZB}}$ – the zero bias piece which describes the remaining effects

which contribute the following term to the recoil.

$$\vec{u}_T^{\text{SOFT}} = + \, \alpha_{mb} \cdot \vec{U_T}^{\text{ MB}} + \vec{U_T}^{\text{ ZB}} \tag{6.10}$$

where α_{mb} is a tunable parameter which allows for the removal of double counting of effects which unavoidably occur in both the $\vec{U_T}^{\text{ MB}}$ and $\vec{U_T}^{\text{ ZB}}$ models. In order to describe the effects due to spectator partons from the breakup of the hadron involved in the initial hard scatter $\vec{U_T}^{\text{ MB}}$ we create a library of events selected by trigger which requires only that there is an inelastic collision in the event. The library contains per event information about the SET, instantaneous luminosity and MET. Events in this library must have exactly one primary vertex so ensure that we do not include contributions in this library which should be included in the model for $\vec{U_T}^{\text{ ZB}}$. These events underestimate the contribution we aim to model because the spatial overlap between the hadrons involved in a collision which results in the production of a W or Z boson is most likely to be larger than for the events in our library increasing the probability for an interaction between the hadron remnants which would lead to an energy deposit in the fiducial volume. We account for this by comparison of the SET distribution of out MB library with the SET distribution of low momentum ($p_T < 3$ GeV) Z boson events where the energy in the electron cones does not contribute to the SET (as usual). The MB library events are reweighted to match the SET distribution from this special Z boson sample. We continue to use the MB library from the RunIIa W mass analysis as the contribution from this event should not have changed. To describe the effects of the underlying event which depend strongly on luminosity (due primarily to multiple interactions, and noise in the calorimeter) our library consists of events read out in time with the beam crossings, which are selected to match the instantaneous luminosity distribution of the data. The complete data library consists of approximately twenty-five million events and the comparison of the instantaneous luminosity distributions from our data sample and the zero bias library is shown in figure 6.6. For each generated event we process through our fast Monte-Carlo simulation processes the information for one randomly selected event from each of the MB and ZB libraries are included as described in equation 6.10. Figure 6.7 shows a comparison of the magnitude of $\vec{u}_T$ in each of the soft libraries which illustrates clearly that the ZB library add significantly more energy than the MB library. A smaller zero bias library has been created from events where the calorimeter was read out in a mode where cell energies are not zero suppressed. For these events the full detector readout is stored in a format, which enables us to overlay this information onto generated events before the detector simulation takes place. A complete description of the zero bias library making process is given in reference [**39**]. This library has approximately 1.7 million events and our fast Monte-Carlo program uses these same events when we are performing studies of

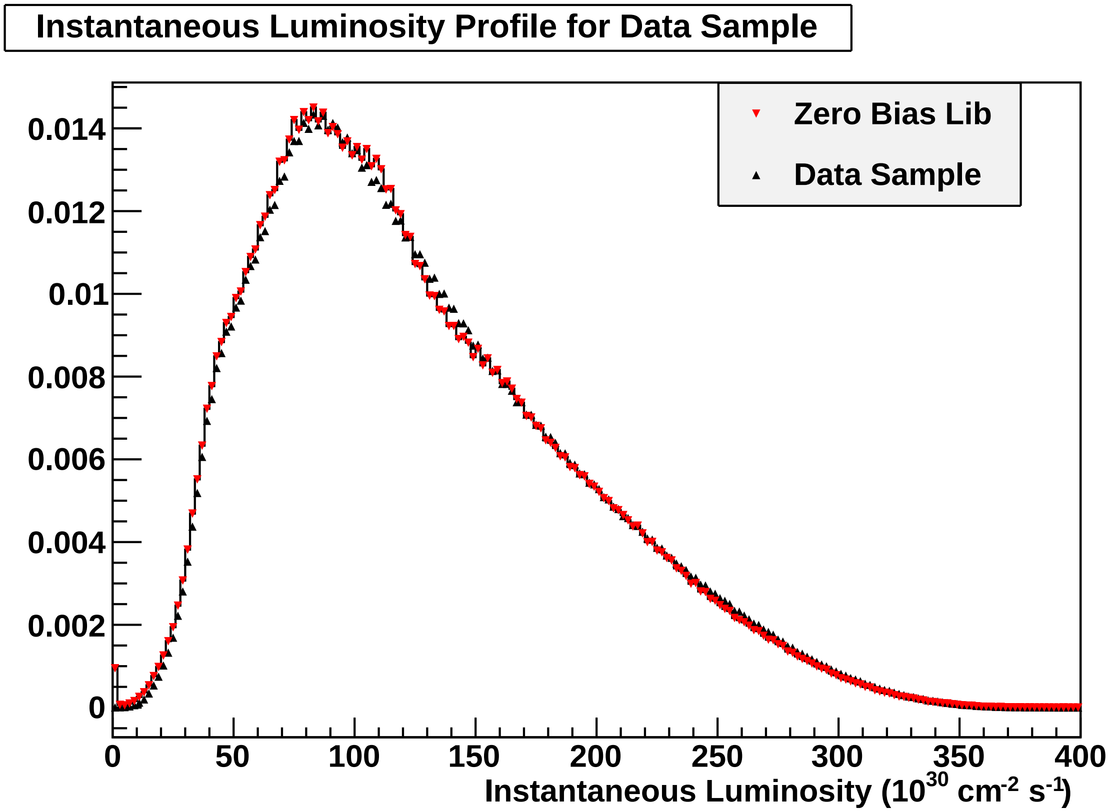

Figure 6.6. Comparison of data and zero bias library luminosity distributions

the full Monte-Carlo. For the moment I will continue to ignore correlated effects between the recoil system and the boson decay products, there is still the correlation between the various recoil components to consider. While the ZB and MB libraries give an accurate description of the SET distribution of the effects they aim to model, the zero suppression of the calorimeter readout means that the SET due to MB+ZB contributions is larger than the sum of the individual contributions as additional cells pass the zero suppression threshold. We study this effect by comparing the SET distribution of Pythia minimum bias events with unsuppressed zero bias events over-laid onto them before the detector simulation (including zero suppression) is applied, to the sum of the individual minimum

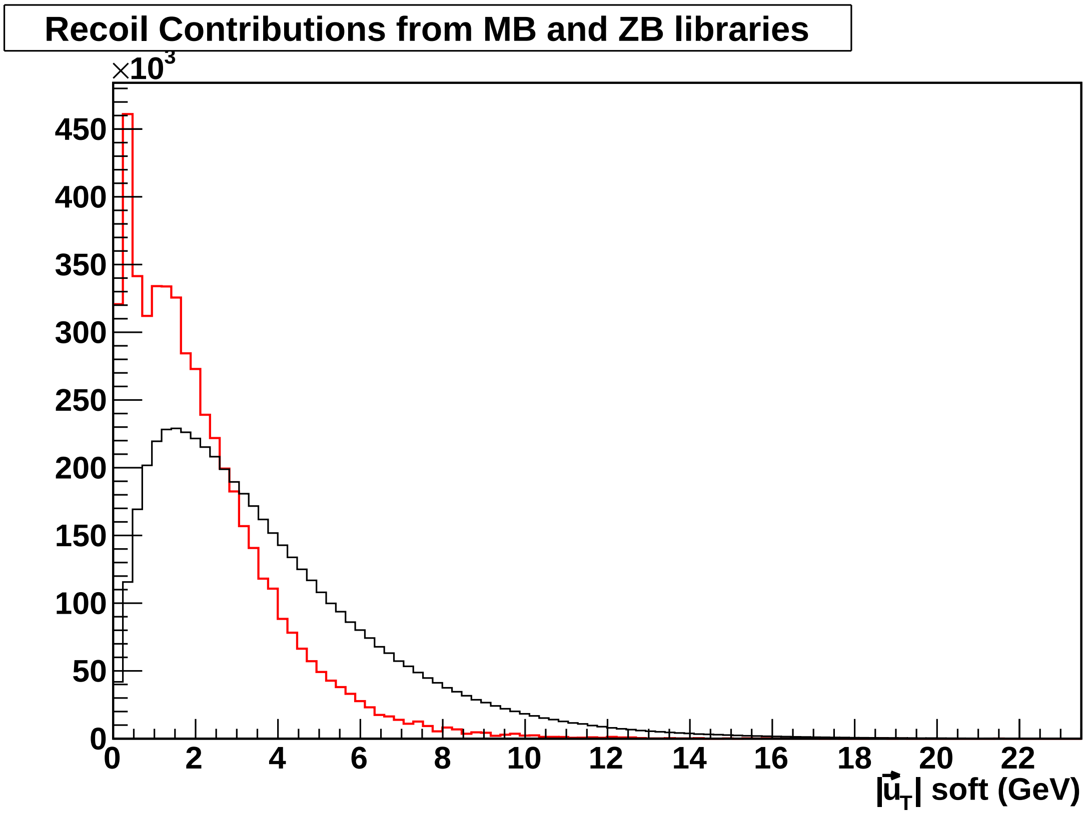

Figure 6.7. Magnitude of the contribution to $\vec{u}_T$ from the MB (red) and ZB (black) libraries.

bias and zero SET values from our libraries. This is done per event and is shown in figure 6.8 we see that this effect can be described with constant multiplicative factor:

$$SET_{MB^i+ZB^j} = \alpha_{SET}(SET_{MB^i} + SET_{MB^j}) \tag{6.11}$$

We use an α_{SET} value of 1.02.

This accounts for a small part of the correlation between the various components of the recoil, which we model separately. We account for the full correlation and the effect of double counting effects by introducing 6 tunable parameters which describe the recoil

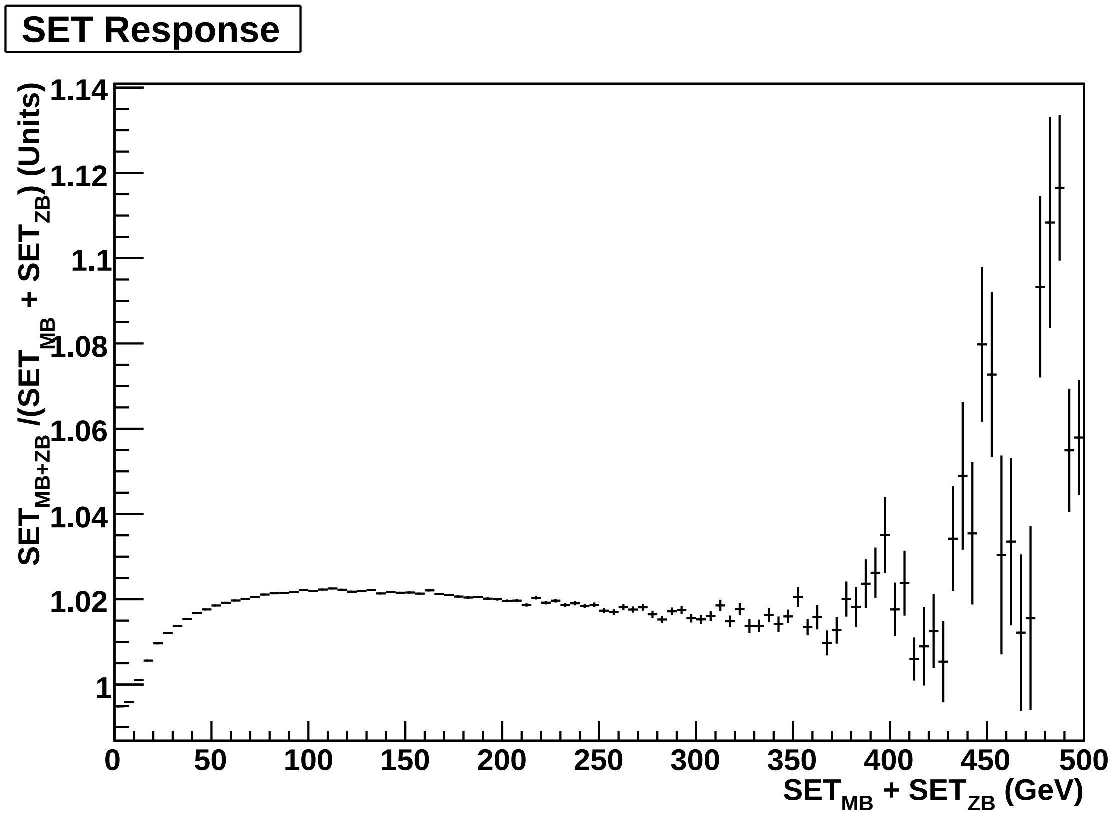

Figure 6.8. Determination of α_{SET}

response and resolution and tuning them by comparing the balance between the Z boson transverse momentum and the recoil transverse momentum in data and fast Monte-Carlo. We minimize the sensitivity of the recoil tuning parameters to the electron resolution by comparison of the η imbalance distribution [**40**] variable (defined below) from $Z \to ee$ events processed through our fast Monte-Carlo simulation with Z events which pass our standard selection cuts. In the plane transverse to the beam axis, the η axis is defined along the inner bisector of the transverse momenta of the two electrons as shown in Figure 6.9. The axis depends only on the directions of the two reconstructed electrons,

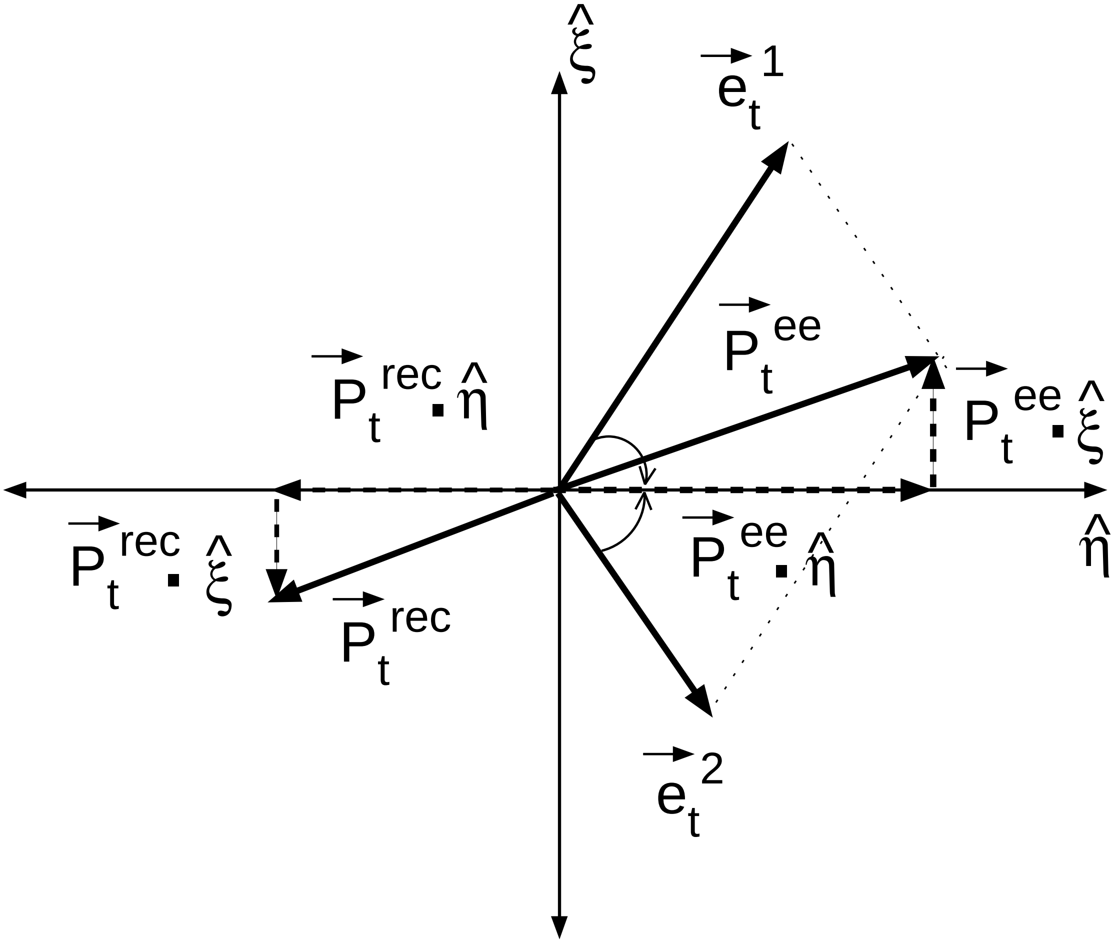

Figure 6.9. The $\eta - \xi$ coordinate system in a $Z \to ee$ event [**5**].

and is independent of their momenta. The ξ axis is defined to be perpendicular to the η axis.

the momentum imbalances along the η and ξ axes are defined as:

$$\begin{aligned} \eta_{imb} &= \vec{p}_T^{\,ee} \cdot \hat{\eta} + \vec{u}_T \cdot \hat{\eta}, \\ \xi_{imb} &= \vec{p}_T^{\,ee} \cdot \hat{\xi} + \vec{u}_T \cdot \hat{\xi}, \end{aligned}$$

where $\vec{p}_T^{\,ee}$ is the momentum of the di-electron pair and $\vec{u}_T$ is the transverse momentum of the recoil. These vectors are projected onto the η axis as ${p_\eta}^{ee}$ and u_η respectively. The mean of the η_{imb} distribution is sensitive to the response and the width is sensitive to the resolution.

The parameters of the recoil response tuning function (R) are determined by performing a template fit to minimize the χ^2 of the mean of the η_{imb} distributions in bins of Z boson transverse momentum between the fast Monte-Carlo and data. The parameters of the recoil resolution tuning function σ_R are similarly determined by minimizing the χ^2 for the width of the η_{imb} distribution in bins of Z boson transverse momentum between data and fast Monte-Carlo. The best-fit comparison is shown in figure 6.10, as well as the χ distribution. We have a greater than two σ deviation in the lowest p_T bin which we are investigating, but which should not have a huge effect on our result as this bin does not contain many events.

$$R_{had} = \text{RelScale} + \text{RelOffset} \cdot \exp \frac{-q_T}{\tau_{\texttt{HAD}}} \tag{6.12}$$

$$\sigma_{R_{had}} = \text{RelSampA} + \frac{\text{RelSampB}}{\sqrt{q_T}} \tag{6.13}$$

where R_{had} describes the additional response of the calorimeter to the recoil which is not adequately described by the hard component model baes on GEANT Monte-Carlo as a function of the magnitide of the generated recoil transverse momentum (q_T). RelOffset describes the response of the calorimeter at low q_T, where the scale of 'low' is set by

τ_{had}. In addition to the parameters in the functions (R_{had}) and ($\sigma_{R_{had}}$) the parameter α_{mb}, introduced previously, is allowed to float when performing the fits. We obtain the following values:

- RelScale = 1.042 ± 0.011,
- RelOffset = 2.16 ± 0.42,
- $\tau_{\texttt{HAD}} = 2.44 \pm 0.38$,
- RelSampA = 1.237 ± 0.050, and
- α_{mb}= 0.568 ± 0.082,

where we have fixed RelSampB to be 0, which is consistent with its preferred value when allowed to float. The recoil response and resolution value are strongly correlated. The correlation between α_{MB} and RelSampA is -0.6913. The correlation matrix below is for RelScale, RelOffset, and τ_{HAD}. Figure 6.12 shows the comparison of the mean of the η_{imb} distribution between fast Monte-Carlo and data, as well as the χ distribution.

$$\begin{pmatrix} 1 & 0.4616 & -0.5984 \\ 0.4616 & 1 & -0.8657 \\ -0.5984 & -0.8657 & 1 \end{pmatrix}$$

6.3. Correlated Response Modeling ($\vec{u}_T^{UPARA}$ and $\vec{u}_T^{PHOTON}$)

The response and resolution of the electromagnetic and hadronic components of the event do not factorize as simply as has been presented above. Energy from the recoil system which overlaps with the electron cone ($-\vec{u}_T^{UPARA}$) will be included as part of the electron energy, and has to be removed from the recoil system in our fast Monte-Carlo

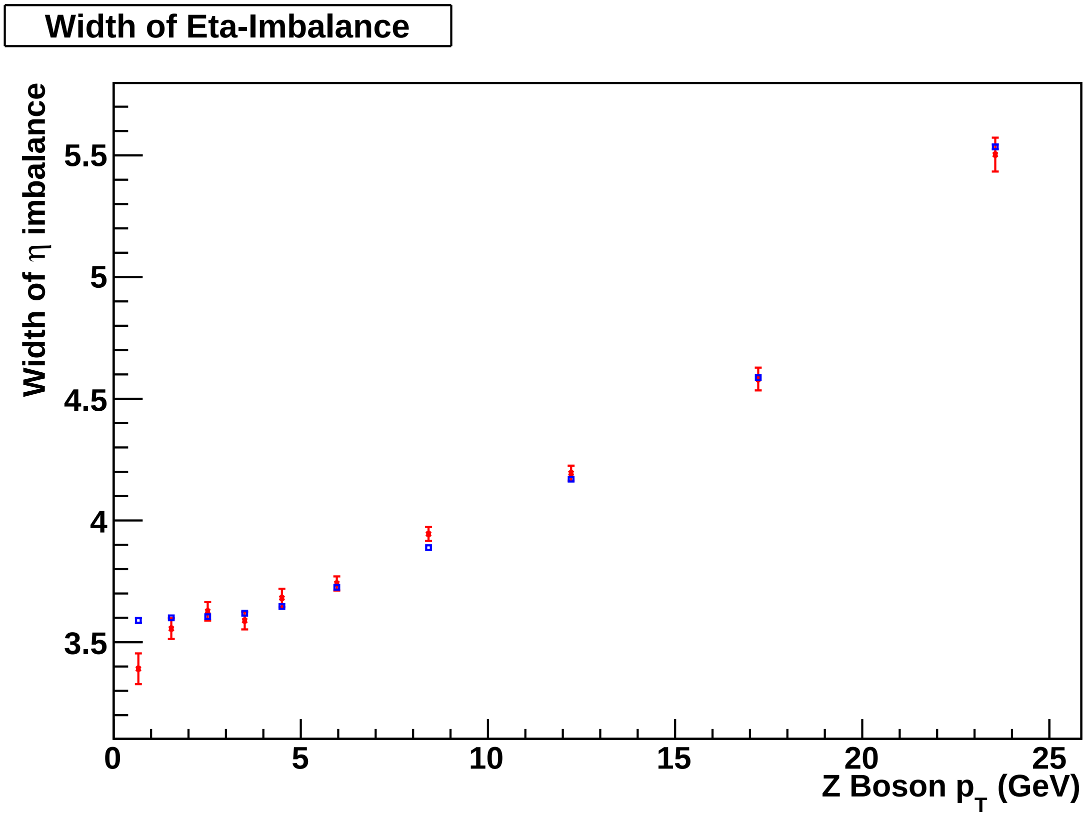

Figure 6.10. Width of the η_{imb} distribution in bins of Z p_T after the recoil tune.

(with the appropriate energy added to the electron description). An electron may radiate a photon outside of the electron cone which will contribute to $\vec{u_T}$ ($\vec{u}_T^{PHOTON}$), but this effect is trivially included since we have a model of FSR and simply add the $\vec{u}_T$ of the γ to the recoil. The component of the recoil which lies under the electron cone is determined from events which pass our W boson selection cuts as a function of η_{det}, instantaneous luminosity and the component of the recoil in the direction of the electron ($u_{||}$) as shown in figure 6.14 and defined in equation 6.14. We sum the energy of EM cluster-like cones of 13 calorimeter towers at the η_{det} value of the leading EM cluster, but rotated away from the electron in ϕ (rotated cone E_T). These values are stored as functions of the instantaneous

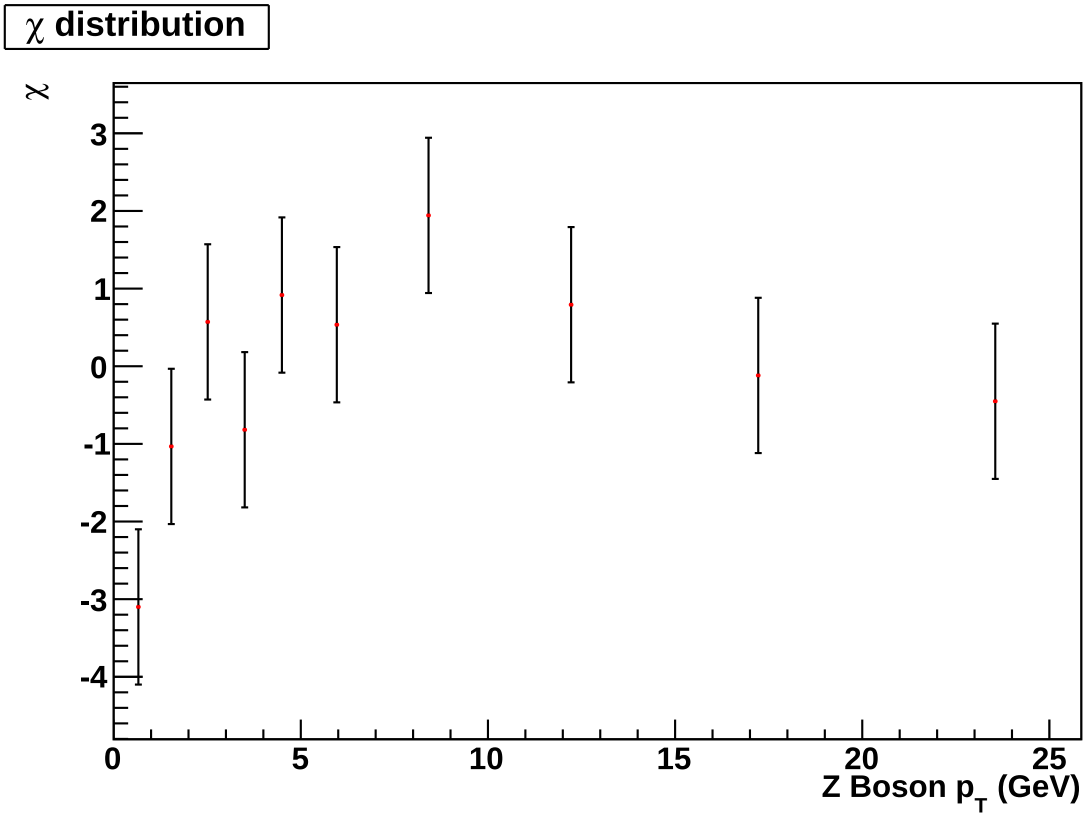

Figure 6.11. χ for the width of the η_{imb} distribution in bins of Z p_T after the recoil tune.

luminosity and $u_{||}$ of the event. When simulating the detector response we draw a random value for this energy ($\Delta u_{||}$) from the luminosity and ($u_{||}$) bin corresponding to the event being modeled. Figure 6.15 shows the spectrum of rotated cone E_T. The distribution is heavily peaked in the first bin which has 11.8×10^6 entries. ($-\vec{u}_T^{UPARA}$ is the transverse projection of a vector of magnitude $\Delta u_{||}$ in the EM cluster direction.)

$$\vec{u}_T^{\,\mathrm{UPARA}} = -\sum_e \Delta u_{\|} \cdot \vec{p}_T(e) \tag{6.14}$$

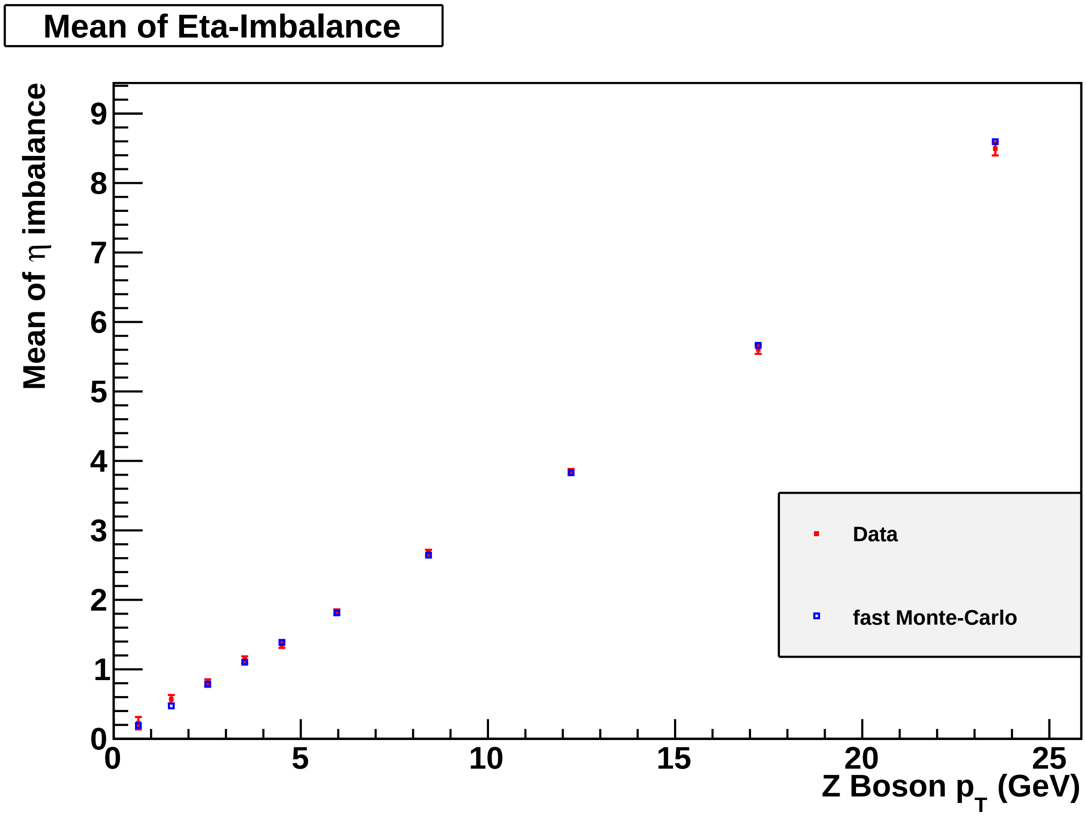

Figure 6.12. Mean of the η_{imb} distribution in bins of Z p_T after the recoil tune.

The effect of the energy from the recoil which lies under the electron, is slightly more complicated to model. One cannot simply add the energy from the rotated cone to the electron, since, as mentioned when describing α_{SET}, the presence of the energy from the electron will mean that more cells in the EM cluster will be above the zero suppression threshold. We model this effect by comparing the change in the energy of a fully reconstructed electron with and without unsuppressed zero bias overlay, as a function of the energy in the towers occupied by the electron when the zero bias overlay is zero suppressed. This is achieved by studying three GEANT Monte-Carlo samples:

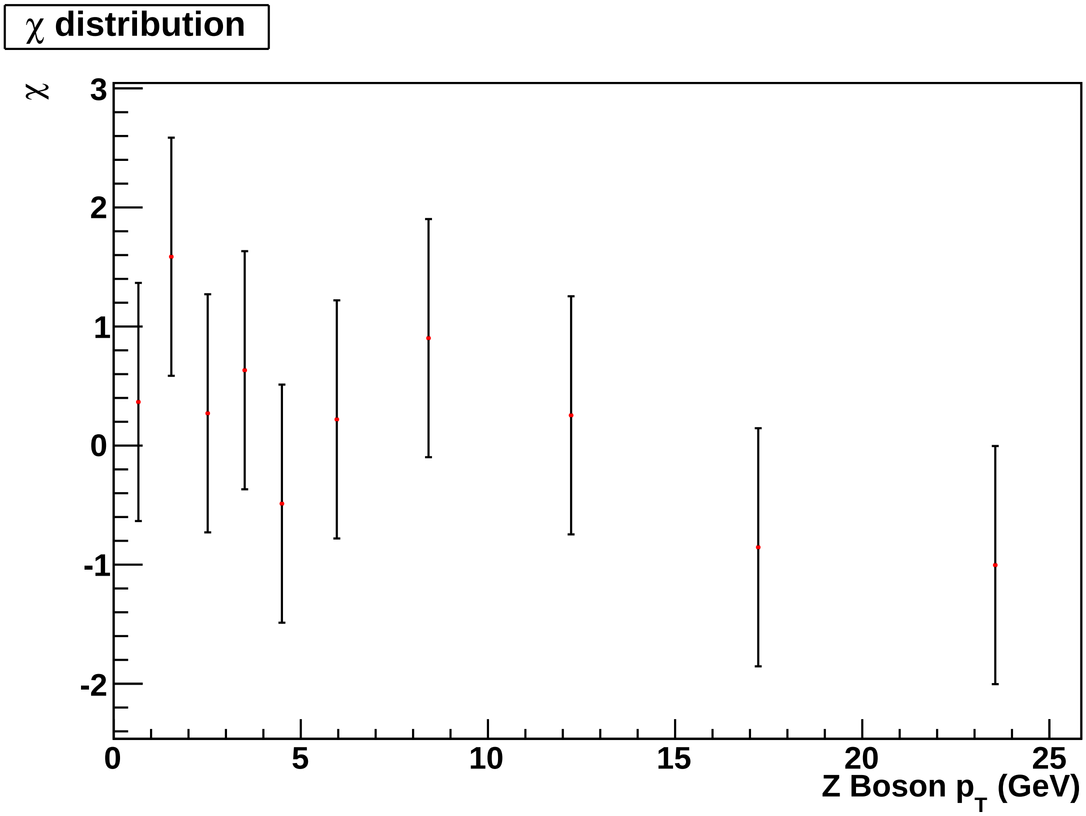

Figure 6.13. χ for the Mean of the η_{imb} distribution in bins of Z p_T after the recoil tune.

- Sample A – Single electrons processed through our full detector simulation with no zero bias overlay.
- Sample B – Zero bias events from the overlay processed through our full detector simulation.
- Sample C – Single electrons processed through our full detector simulation with zero bias overlay.

For all electrons from sample C which pass our selection cuts, we compare the sum of the energy in the cells, which contribute to the cluster in each of the three samples (E_{cells}).

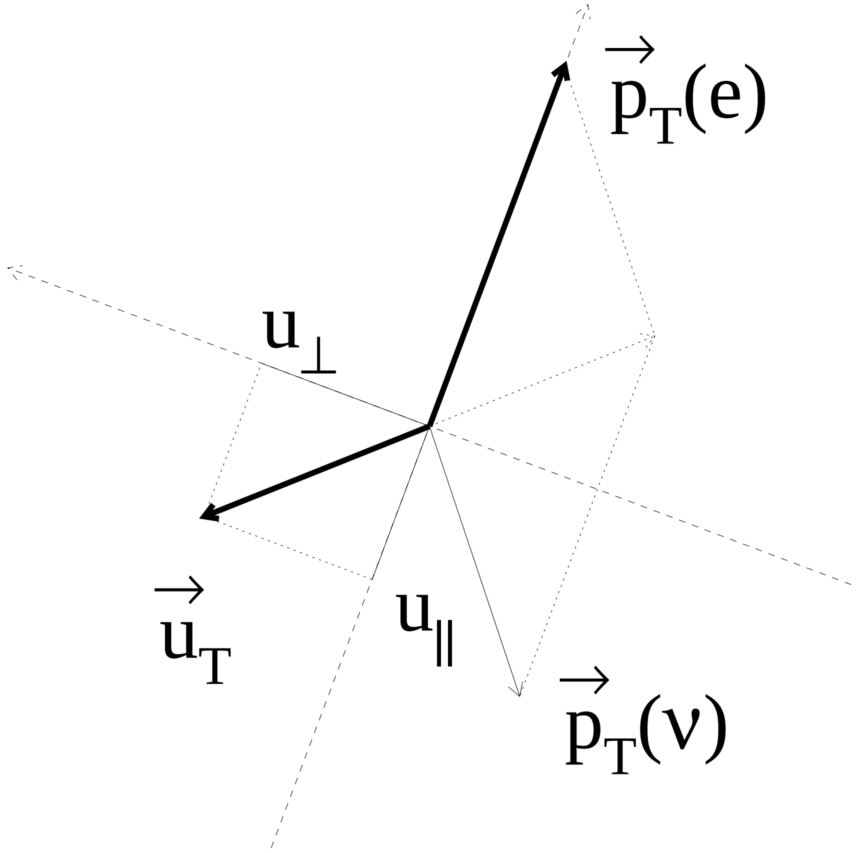

Figure 6.14. Definition of $u_{||}$.

This allows us to determine :

$$U_{para_{c}orr} = f({E_{cells}}^{B}) = {E_{cells}}^{C} - {E_{cells}}^{A}, \tag{6.15}$$

the correction to the EM cluster energy (u_{para_corr}) as a function of $\Delta u_{||}$. We determine these functions in bins of η_{det} and use two distinct samples of single electrons, one of which is kinematically similar to the η and E_T spectrum of electrons from Z boson decay, and one which is similar to the spectrum from W boson decay. The correction is shown in figures 6.16,6.18, and 6.17, where the red points (and fit) correspond to results from

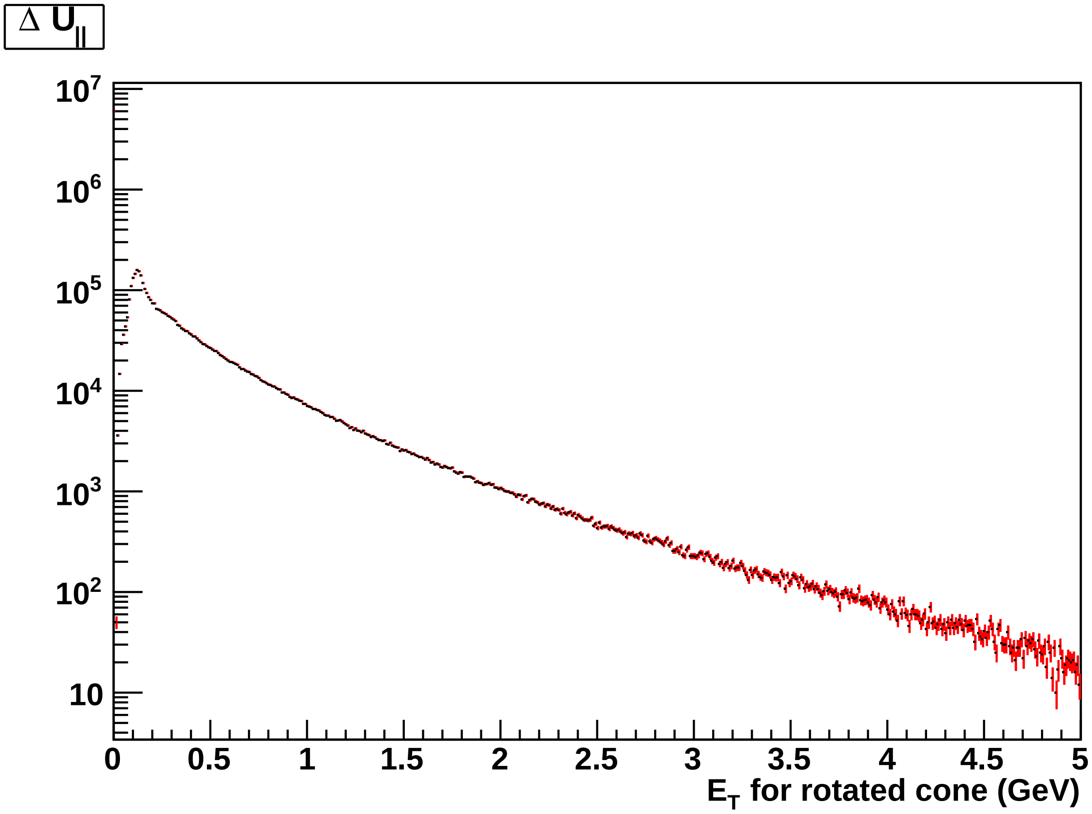

Figure 6.15. E_T spectrum of rotated cone used to model $\Delta u_{||}$

the Z boson like sample, and the black points (and fit) correspond to the results from a W boson like sample. This correction is not sensitive to the difference between the two. These fits are used to correct the EM cluster energy in our fast simulation. As shown in figure 6.15 the most likely input to this correction ($\Delta u_{||}$) is essentially zero. In this case in order to take advantage on the information we have describing fluctuations in u_{para_corr} we do not modify the EM cluster energy based on the functions shown in figures 6.16,6.18, and 6.17, instead we select a random value from a histograms of all values of u_{para_corr} in our GEANT Monte-Carlo study which correspond to the correct bins of η_{det} and $\Delta u_{||}$. An example of one of these histograms is shown in figure 6.19.

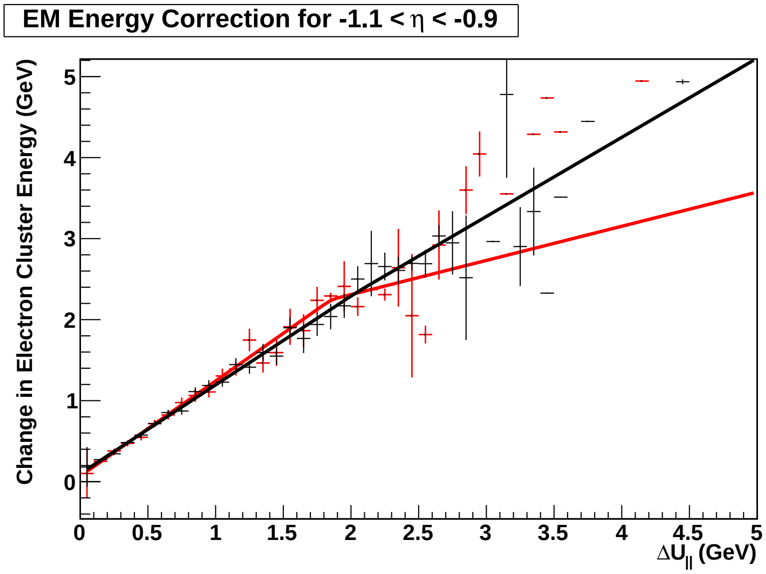

Figure 6.16. Correction to EM Cluster Energy as a function of $\Delta u_{||}$ for η between -1.1 and -0.9. The red points correspond to Z boson like events, and the black points to W boson like events.

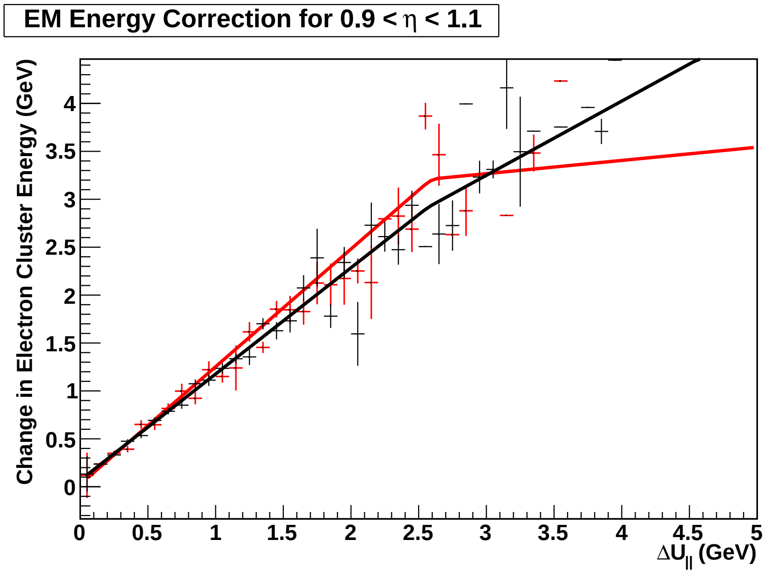

Figure 6.17. Correction to EM Cluster Energy as a function of $\Delta u_{||}$ for η between 0.9 and 1.1. The red points correspond to Z boson like events, and the black points to W boson like events.

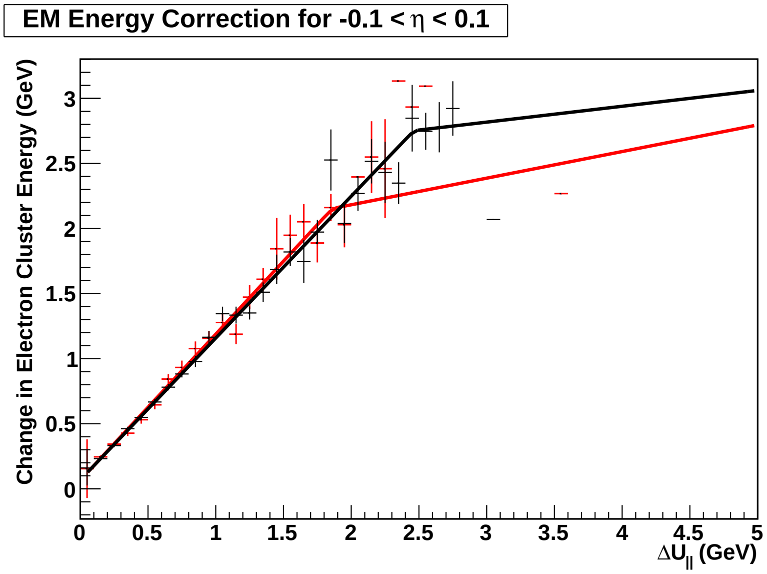

Figure 6.18. Correction to EM Cluster Energy as a function of $\Delta u_{||}$ for η between -0.1 and 0.1. The red points correspond to Z boson like events, and the black points to W boson like events.

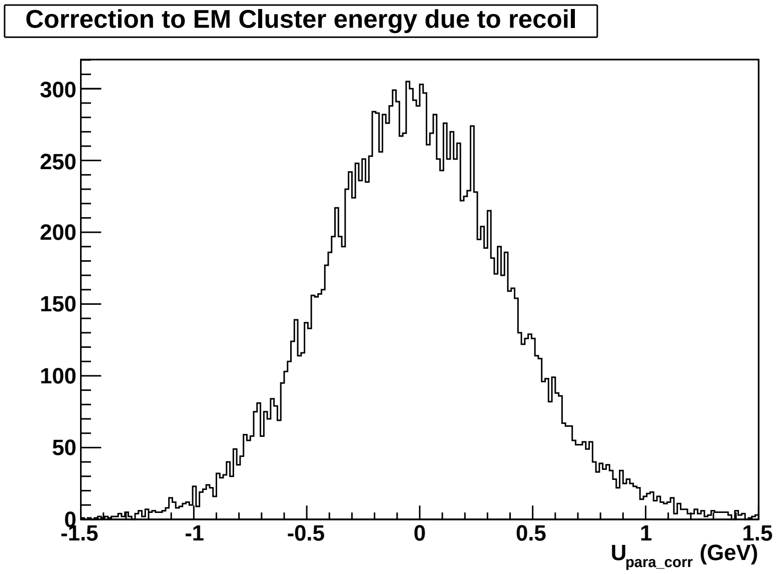

Figure 6.19. Histogram of u_{para_corr} values for central (-1.1 < η < 1.1) W like events

CHAPTER 7

Efficiencies

Our measurement is not particularly sensitive to the absolute efficiencies of our selection cuts, since we are performing a shape-based analysis rather than a counting based one. We do need to be careful to describe the kinematic dependence of the efficiency of our detector and event selection cuts as any kinematic effect in the data which is not reproduced in our fast Monte-Carlo will lead to a bias in our result. We begin by measuring the efficiency for each of our electron selection cuts using a method called tag and probe[**41**] that exploits our knowledge of the Z boson to provide us with a clean sample of electrons with which to evaluate our efficiencies. We then evaluate the efficiencies with respect to the kinematic variables SET and $u_{||}$ which are sensitive to more than just the properties of a single electron, and include information from the recoil system which affects our ability to identify real electrons in the detector. The Tag and Probe method requires one 'Tag' electron to pass our full selection criteria, coupled with a second 'Probe' electron which is used to evaluate the efficiency we are concerned with. We require that the invariant mass of the tag and probe electrons is within the range $70 < m(e, e) < 110$ GeV to reduce background contributions.

7.1. Direct EM Cluster Efficiencies

This section describes the determination of efficiencies for identifying EM clusters, which are parameterized in terms of the property of the EM Cluster.

7.1.1. Vtx Position Simulation

The primary vertex distribution is a function of the beam parameters of the Tevatron, the information required to reproduce the distribution is determined from studying the vertex position distribution of events written out with zero bias trigger requirements for a variety of time 'epochs'. When simulating an event in our fast simulation we pick a vertex position randomly from the vertex distribution corresponding to the epoch in which the event picked from our zero bias library was taken. The final Vtx_Z position is shown after selection cuts in figure 7.10 for Z boson events.

7.1.2. Trigger Efficiency

The Trigger Efficiency for each of our triggers (E1_SHT_25 (v15), E1SHT_25 (v16) and E1_SHT_27) is shown in figure as a function of transverse momentum. The Tag electron is required to pass all our Z boson selection cuts including the trigger requirement. The probe is required to pass all our usual cuts except the trigger requirement. The efficiency is determined from the fraction of 'probe' electrons which pass the level1, level2, and level3 trigger requirements for the trigger under study. Figures 7.1,7.2 and 7.3 show the probability for the probe electron to pass the trigger requirement as a function of transverse momentum for each of the triggers we utilize. Each histogram includes two efficiency determinations; a black one, which is based on our entire data sample, and a red one, which is based only on the data taken with the trigger currently under study. We see that for E1_SHT_27 which ran only at high luminosity, the determination using the entire dataset is an overestimation, showing that there is a luminosity dependence of

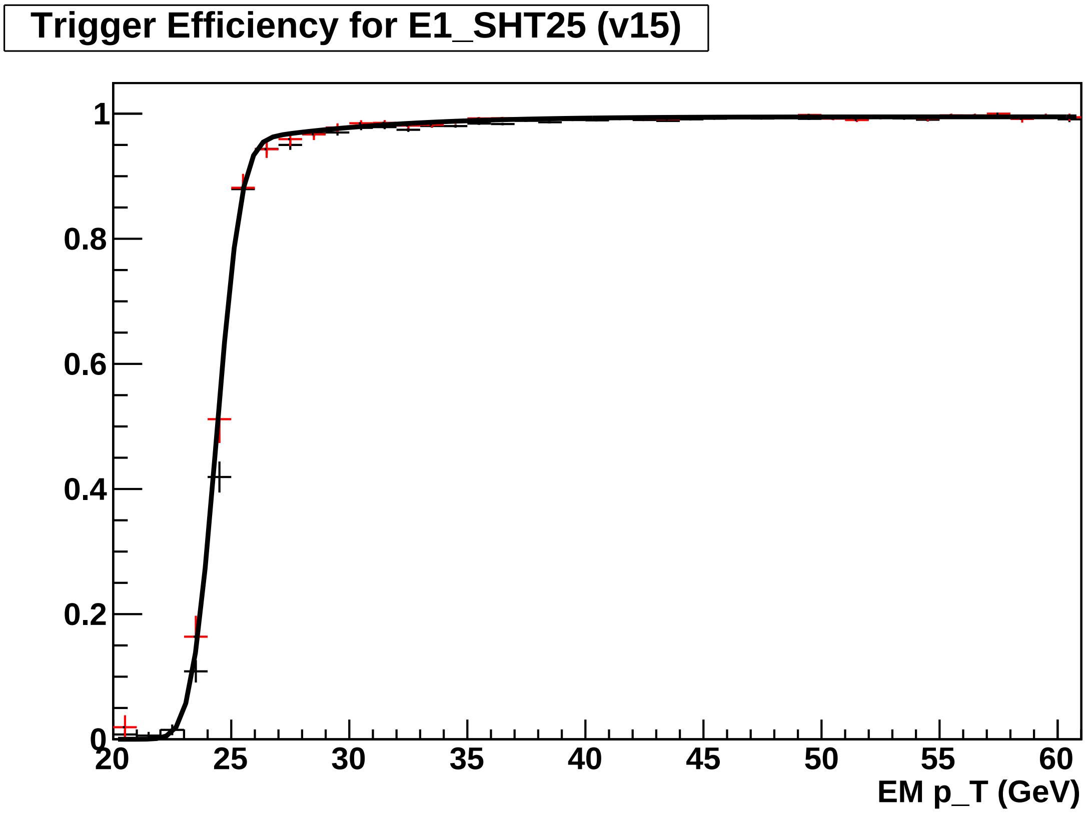

Figure 7.1. Trigger Efficiency for RunIIb $E1\_SHT25$ (v15) determined by Tag and Probe. The black histogram is determined from all the data in our sample. The red histogram is determined only from the sample of events taken with $E1\_SHT25$ (v15).

the trigger. We determine the trigger efficiencies for a given trigger using only the data taken with the trigger under study.

7.1.3. Preselection Efficiency

The preselection efficiency is the probability that we will detect an EM cluster with $frac_{EM} < 0.9$ and $f_{iso} < 0.15$. In this case the tag is still an EM cluster, which passes our full set of selection cuts. The probe, however, is a track with a $p_T > 12$ GeV. We require

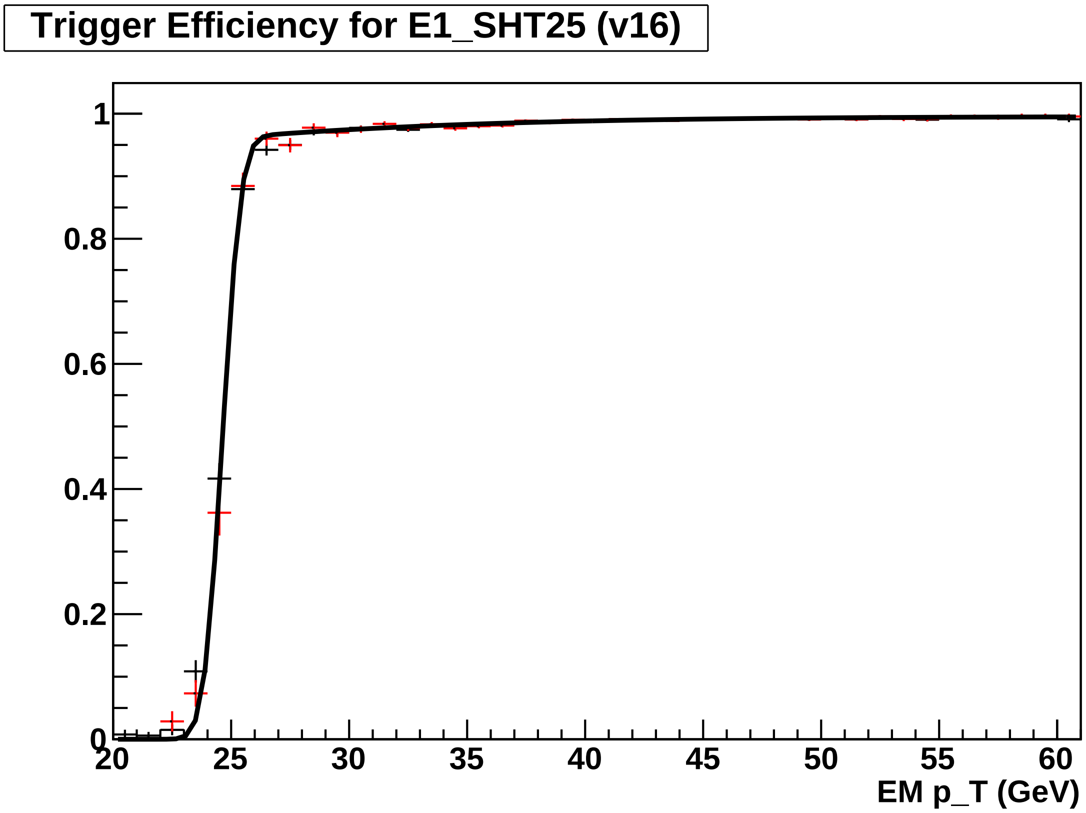

Figure 7.2. Trigger Efficiency for RunIIb $E1\_SHT25$ (v16) determined by Tag and Probe. The black histogram is determined from all the data in our sample. The red histogram is determined only from the sample of events taken with $E1\_SHT25$ (v16).

that the EM cluster-track invariant mass lies in the window ($70 < m(cluster\,track) < 110$ GeV) and look for a second EM cluster within a radius of 0.2 in $\eta \times \phi$ of the track. In the central region we see no evidence of a deviation from an efficiency of unity, as shown in figure 7.4. The structure outside of $|\eta| > 1.1$ is not a concern since we do not use electrons from the end cap calorimeter in this analysis.

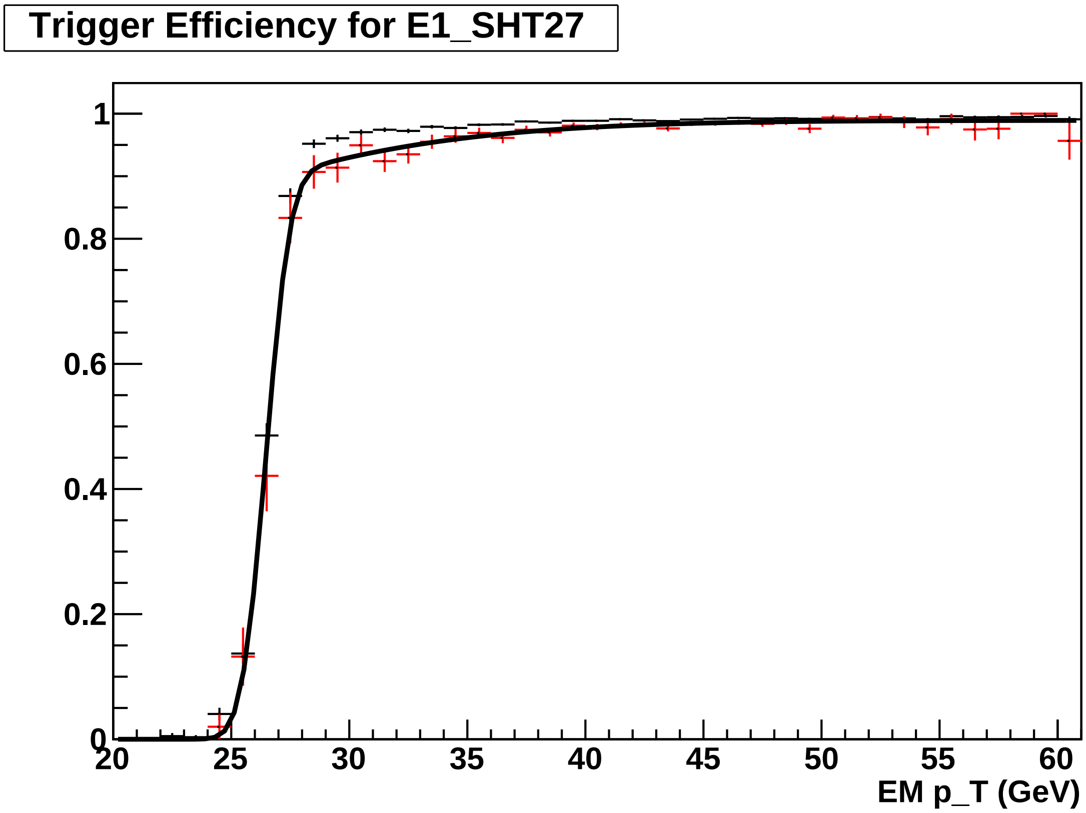

Figure 7.3. Trigger Efficiency for RunIIb $E1\_SHT27$ (v16) determined by Tag and Probe. The black histogram is determined from all the data in our sample. The red histogram is determined only from the sample of events taken with $E1\_SHT27$ (v16).

7.1.4. Spatial Track Match Efficiency

This is the efficiency for finding any track matched to an EM cluster (with no quality cuts on the track). The probe EM cluster in this case is any EM cluster which passes our preselection requirement. This efficiency is determined in bins of η_{phys} and Vtx_Z as shown in figure 7.5.

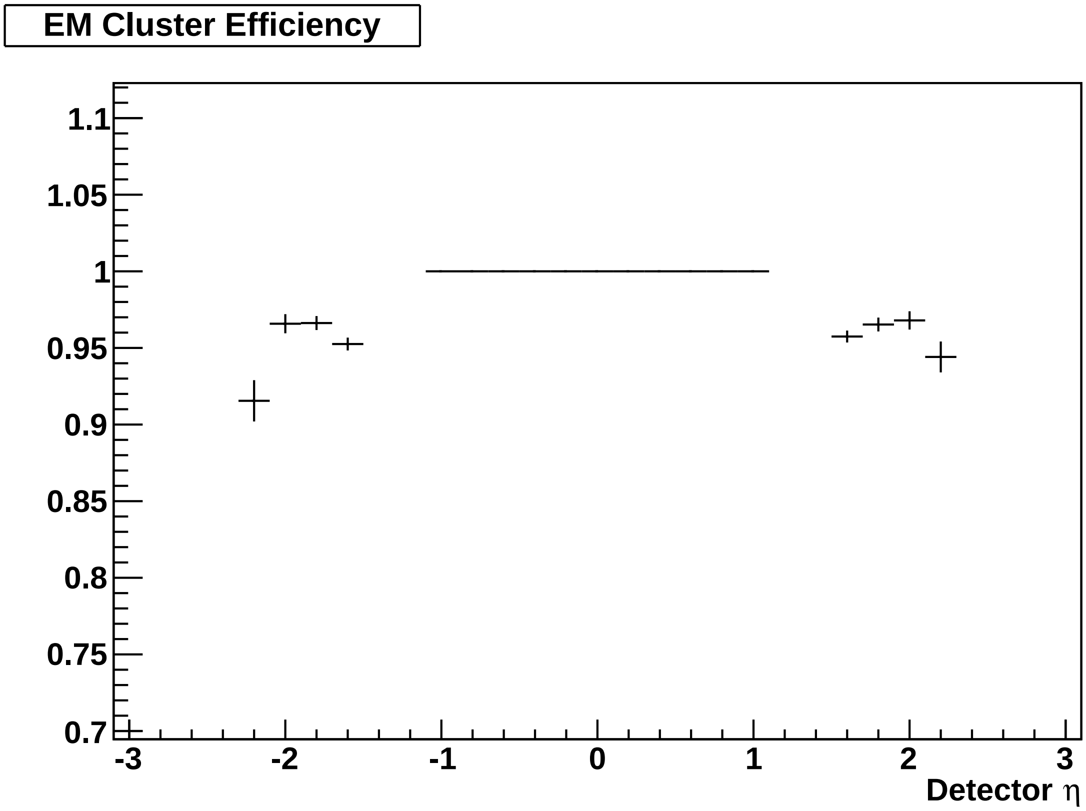

Figure 7.4. Efficiency for finding EM clusters as a function of η_{det}.

7.1.5. HMatrix Efficiency

The probe EM cluster in this case is required to pass the preselection and spatial track match cuts, and we evaluate the efficiency of these electrons to pass the HMatrix Cut in bins of η_{det} as shown in figure 7.7.

7.1.6. Tight Track Match Efficiency

This is the efficiency for finding a track which passes our full set of analysis tracking cuts. The probe EM cluster in this case has passed all of the analysis cuts except for the tracking and trigger selection cuts. This efficiency is determined in bins of η_{phys} and

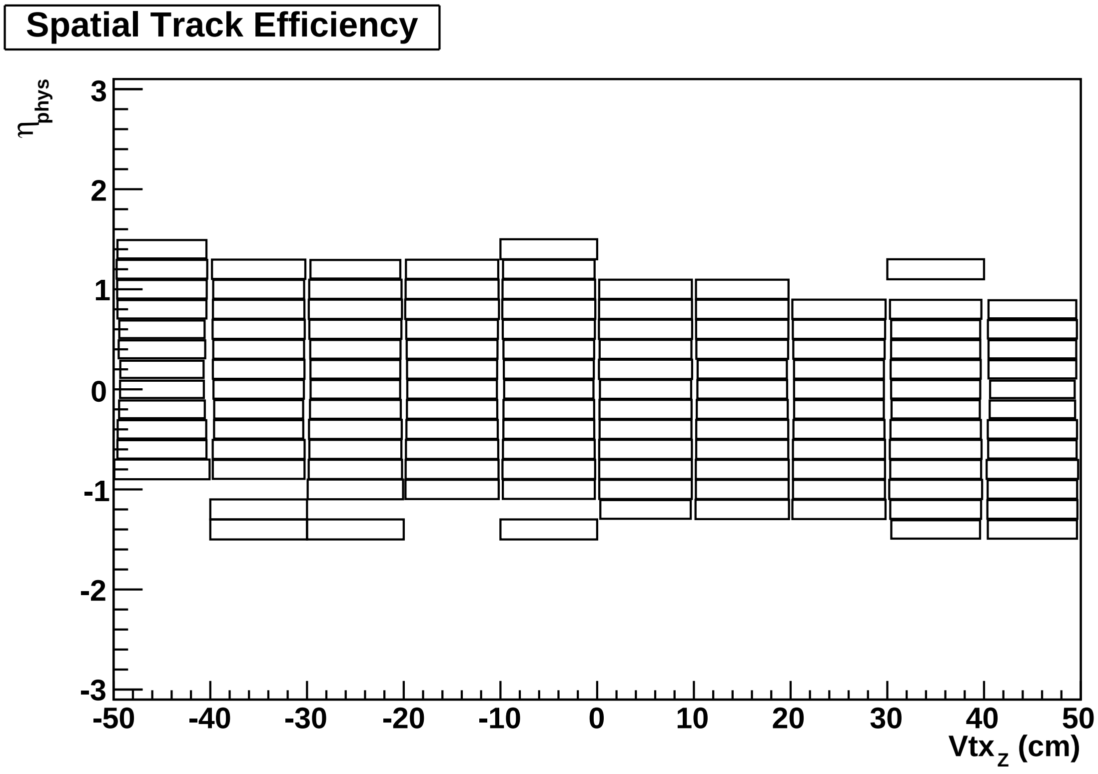

Figure 7.5. Spatial track match efficiency for events which have passed the EM cluster selection as a function of η_{phys} and the z co-ordinate of the primary vertex.

Vtx_Z as shown in figures 7.8 and 7.9. The course binning in this efficiency is responsible for the discontinuities in the simulated Vtx_Z distribution shown in figure 7.10.

7.2. Recoil Related Efficiencies

This section describes the $u_{||}$ and SET dependence of our selection. The $u_{||}$ efficiency, as its name implies is based on the overlap between the recoil and electron systems. The SET efficiency introduces a dependence on the activity in the detector for a given event. Both of these efficiencies aim to describe the degradation of the tracking, isolation, and

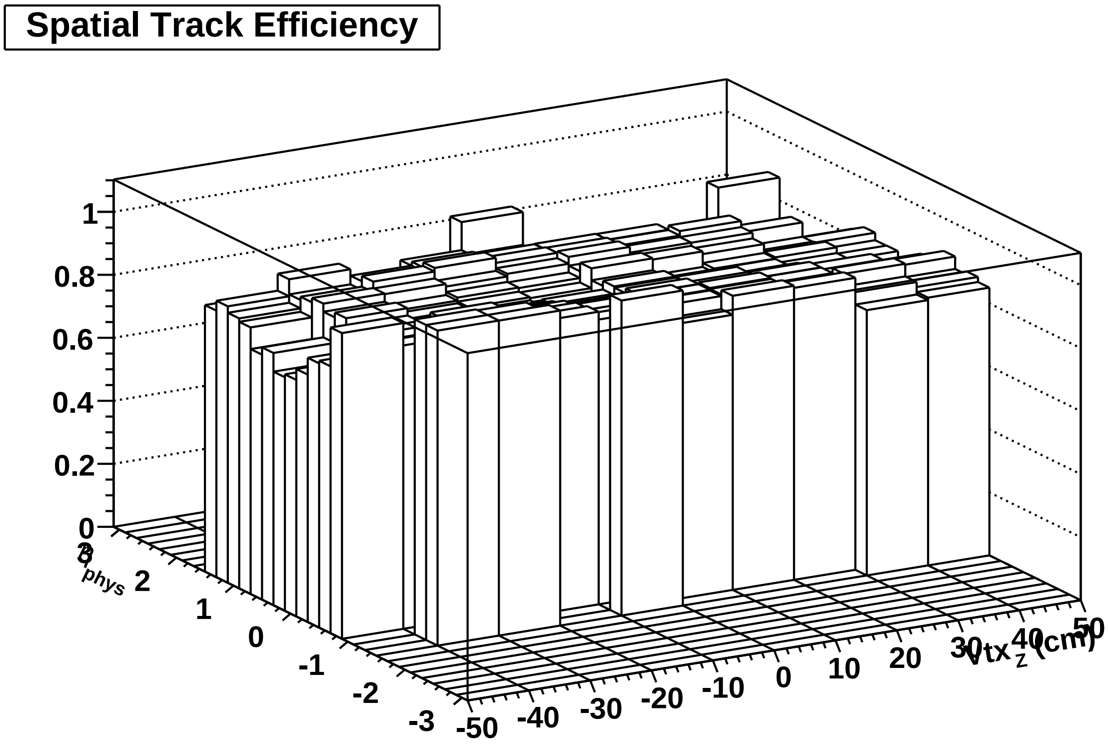

Figure 7.6. Spatial track match efficiency for events which have passed the EM cluster selection as a function of η_{phys} and the z co-ordinate of the primary vertex.

HMatrix discriminates used to identify electrons as energy from other sources leaks into the EM cluster.

7.2.1. SET Efficiency

The Scalar E_T efficiency has two components. The initial efficiency is determined from GEANT based Monte-Carlo studies. We find that determining the efficiency in this way is not sufficient for our analysis and a correction based on the ratio of the efficiency in data and GEANT Monte-Carlo is determined to describe the efficiency in data. Both efficiency components are applied as 'per event' efficiencies, not per electron as with the efficiencies

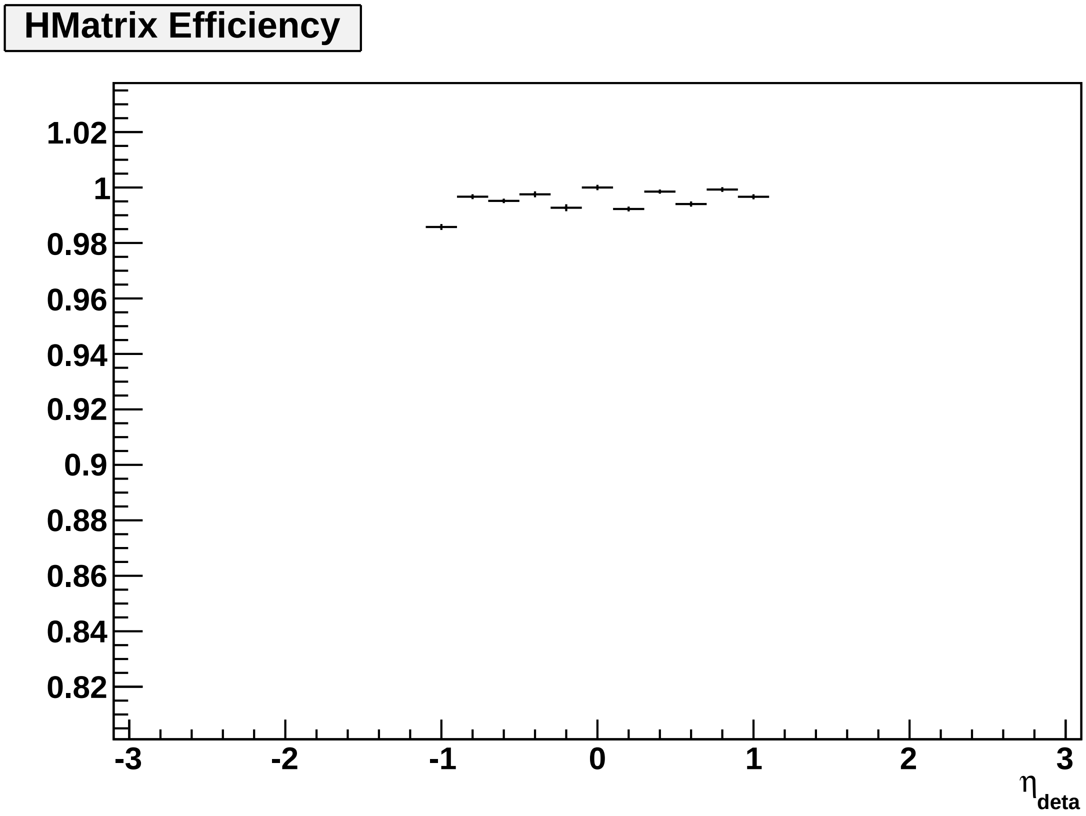

Figure 7.7. The efficiency for EM Clusters which have passed the preselection and spatial track match cuts to pass the shower shape requirements as a function of η_{det}.

previously described. The GEANT based initial efficiency is determined in bins of electron p_T and is determined using truth information as the ratio of the number of events which pass all selection requirements to the number of events which pass just the acceptance requirements. The SET and instantaneous luminosity distributions predicted from our fast Monte-Carlo simulation with this efficiency applied still shows a discrepancy with the data, we have identified this discrepancy to being primarily due to the SET dependence of the efficiency for finding spatial tracks, and determined that there is an additional luminosity dependence. The efficiency for finding a track is evaluated separately for the

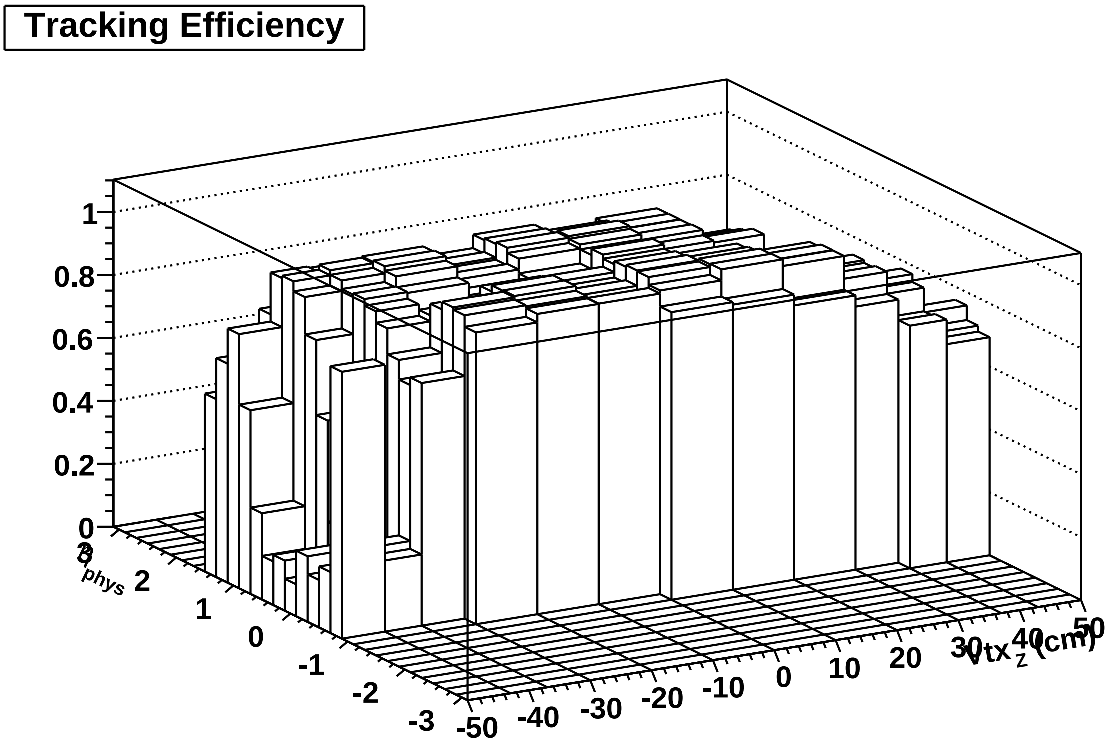

Figure 7.8. The efficiency for EM cluster, which has passed all of our other selection cuts to be matched to a tight track, shown as a lego plot.

GEANT Monte-Carlo and the data in bins of luminosity, SET, and electron transverse momentum. The ratio of these efficiencies is applied as an additional efficiency in our fast Monte-Carlo when we are describing the data. The correction is shown for one bin of SET ($80 < \text{SET} < 110$ GeV) as a function of the transverse momentum of the electron for two luminosity bins in figures 7.11 and 7.12. Figure 7.13 shows the entire luminosity range. The luminosity dependence is clear. Unfortunately the limited yield of Z bosons means that the binning is coarse.

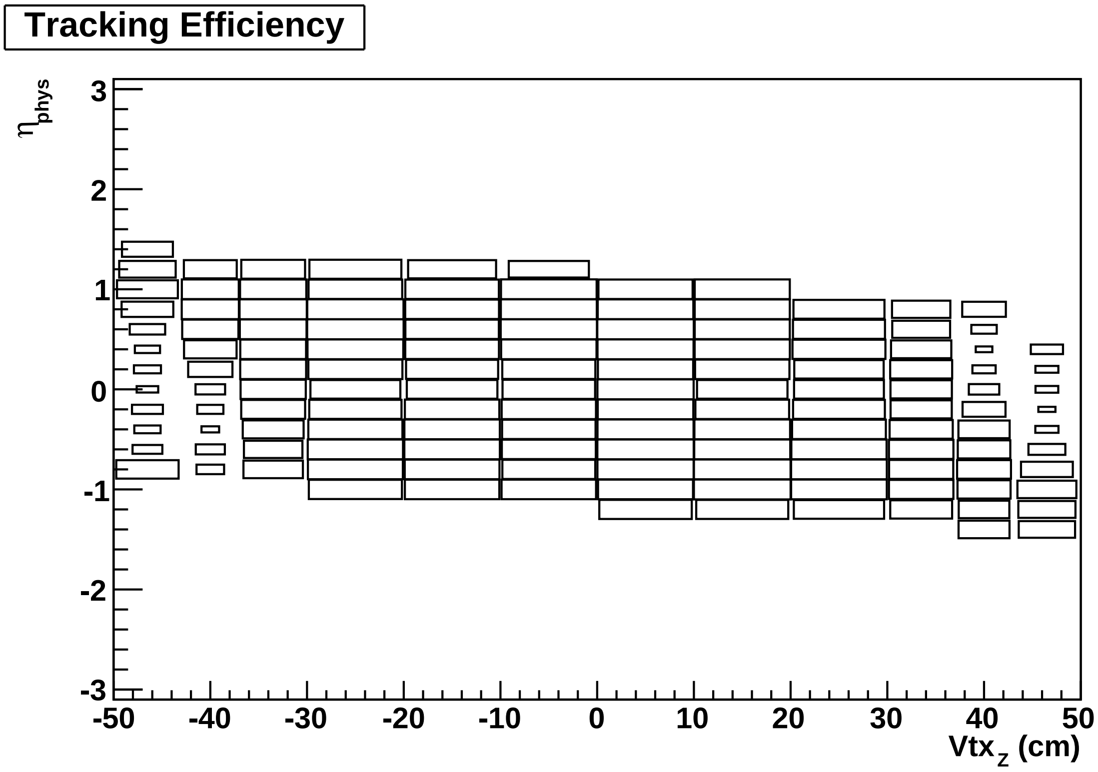

Figure 7.9. The efficiency for EM cluster, which has passed all of our other selection cuts to be matched to a tight track, shown as a box plot.

The effect of the correction is illustrated in figure 7.14, where we see that although the efficiency correction improves agreement between data and our fast Monte-Carlo, the agreement is not as good as we would like.

7.2.2. $u_{||}$ Efficiency [6].

The variation of our ability to identify an EM cluster which passes all of our selection cuts as a function of $u_{||}$ is determined from tag and probe studies where the probe is an EM cluster with $frac_{EM} > 0.9$ (no isolation cut), and the efficiency is determined by requiring that the probe pass isolation, HMatrix and track match requirements as we expect these

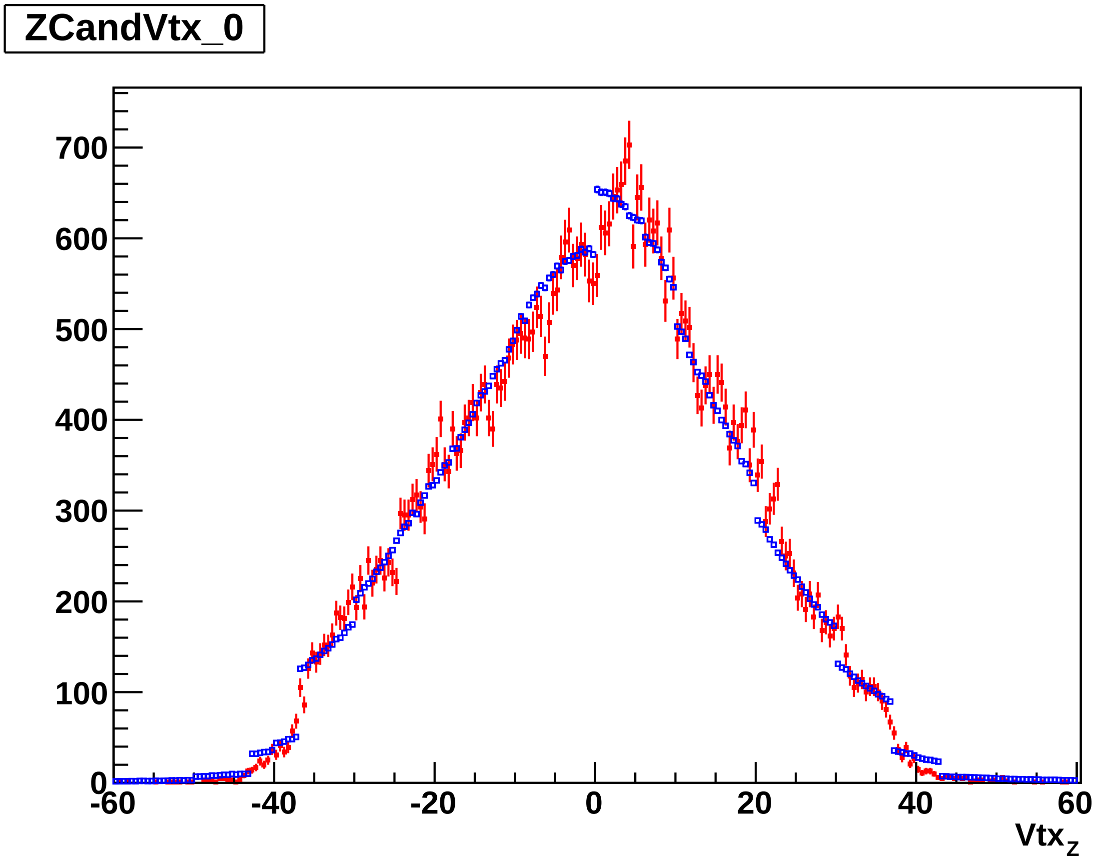

Figure 7.10. Comparison of our simulated Z co-ordinate of the Vtx with Data. The discontinuities in the fast simulation description are due to the binning of the track match efficiency determination.

conditions to be most sensitive to $u_{\|}$. The efficiency is parameterized in the following way:

$$\epsilon(u_{\|}) = p_2 \begin{cases} 1 & \text{for } u_{\|} < p_0 \\ 1 - p_1(u_{\|} - p_0) & \text{otherwise} \end{cases}$$

Where p_2 is an overall efficiency for the combined cuts under study, p_0 is the value of $u_{\|}$ below which the efficiency is constant as a function of $u_{\|}$, and p_1 is the rate of change of the efficiency above p_0. In order to properly account for the relationship between the

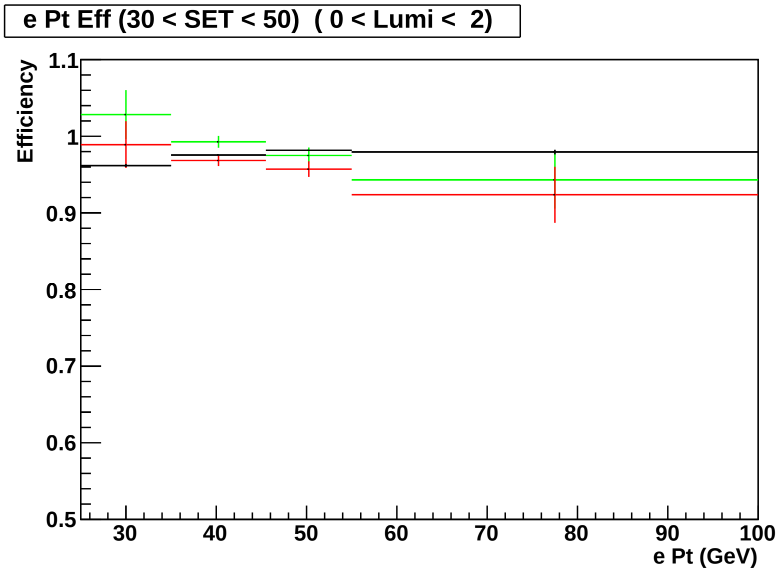

Figure 7.11. SET Efficiency Correction at low luminosity. The black points correspond to the GEANT Monte-Carlo, the red points to the data, and the green to the ratio.

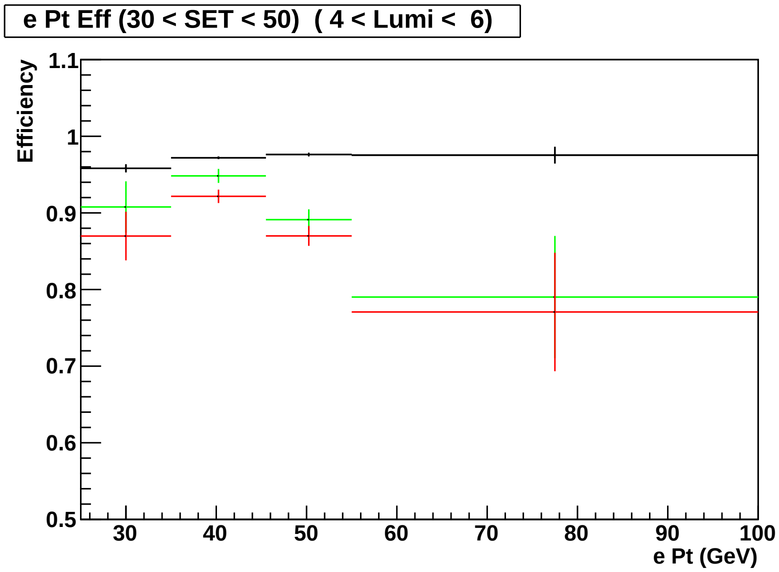

Figure 7.12. SET Efficiency Correction at high luminosity. The black points correspond to the GEANT Monte-Carlo, the red points to the data, and the green to the ratio.

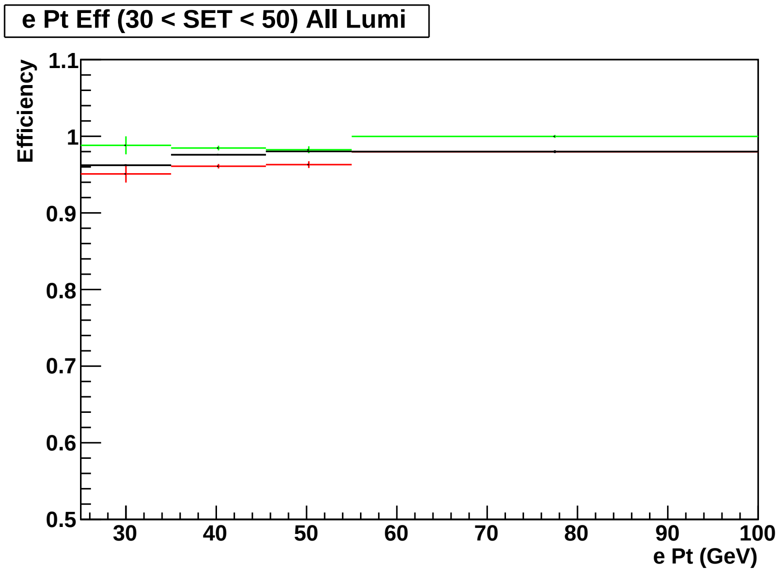

Figure 7.13. SET Efficiency Correction averaged over all luminosity bins. The black points correspond to the GEANT Monte-Carlo, the red points to the data, and the green to the ratio.

EM cluster and the recoil system, which applies to W boson events, we allow for the tag electron to be in either of the end cap (EC) calorimeters. Based on GEANT Monte-Carlo studies we have verified that the value obtained from tag and probe methods is a realistic estimate of the efficiency, and that by scaling the $u_{||}$ value by the ratio of the masses of the W and Z bosons the appropriate parameters for W boson events is obtained. The parameters p_0, p_1 and p_2 are not used directly in our fast Monte-Carlo simulation. In order to ensure that we do not double count efficiencies determined previously, the parameters we feed into the functional dependence of $\epsilon(u_{||})$ are determined so as to ensure that the tag and probe study of the FAST Monte Carlo returns the same values as the study in the data. The $u_{||}$ efficiency has not been properly updated from the RunIIa determination [**9**]. The model of $u_{||}$ has been updated to be representative of the environment at DØ for RunIIb, and parameter which in our fast simulation which ensures that the p_1 values in

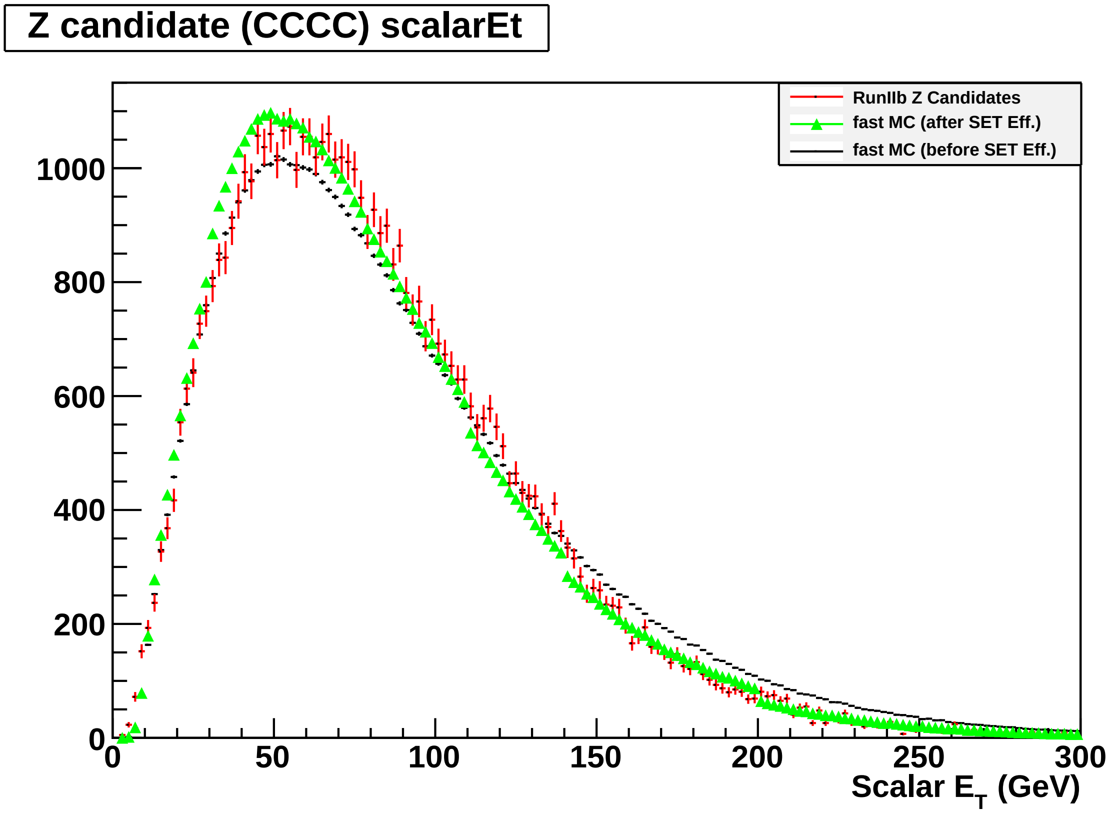

Figure 7.14. Scalar E_T distribution for Z → ee events, illustrating the effect of the Scalar E_T efficiency correction.

the fast Monte-Carlo and the data match has been updated [**42**]. The new value is a minor correction, as the previously described set of efficiencies, when applied, bring us very close to the correct $u_{||}$ dependence. Table 7.1 shows the parameters that have been determined for this efficiency. Figure 7.15 shows the efficiency determined from tag and probe, for RunIIa. Figure 7.16 shows the Tag and Probe comparison between RunIIb data, and our fast simulation. We see that although the parameters have not been tuned the simulation shows the correct behavior.

	p_0 (GeV)	p_1 (GeV^{-1})	p_2
$Z \to ee$	1.250 ± 0.041	0.0053 ± 0.0006	0.7966 ± 0.0012

Table 7.1. $u_{||}$ Efficiency parameters using tag-probe method in $Z \to ee$ events.

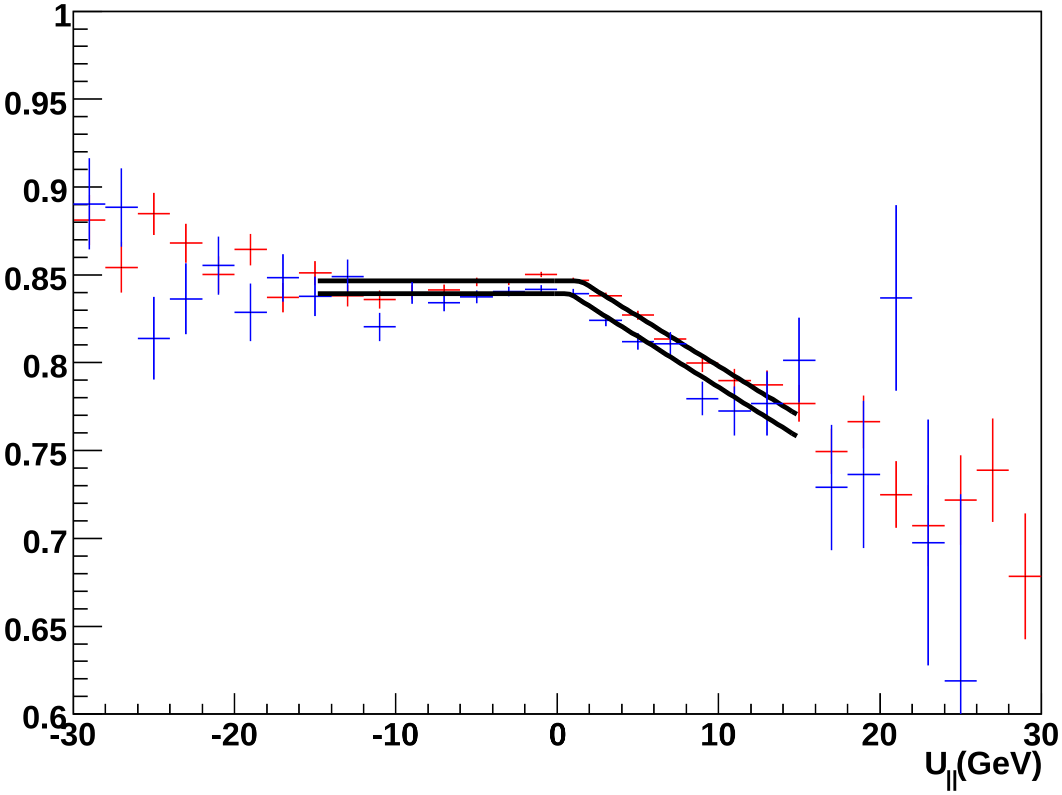

Figure 7.15. $u_{||}$ efficiency in full Monte-Carlo $Z \to ee$ using the tag-probe method with the tag electron either in the CC (Red) or the EC (Blue) region for RunIIa, The probe electron is always in CC region [**6**].

7.3. Z → ee Comparison with Data

As part of this analysis we have developed a large number of control plots which allow us to evaluate the quality of our fast Monte-Carlo before making a decision to remove the

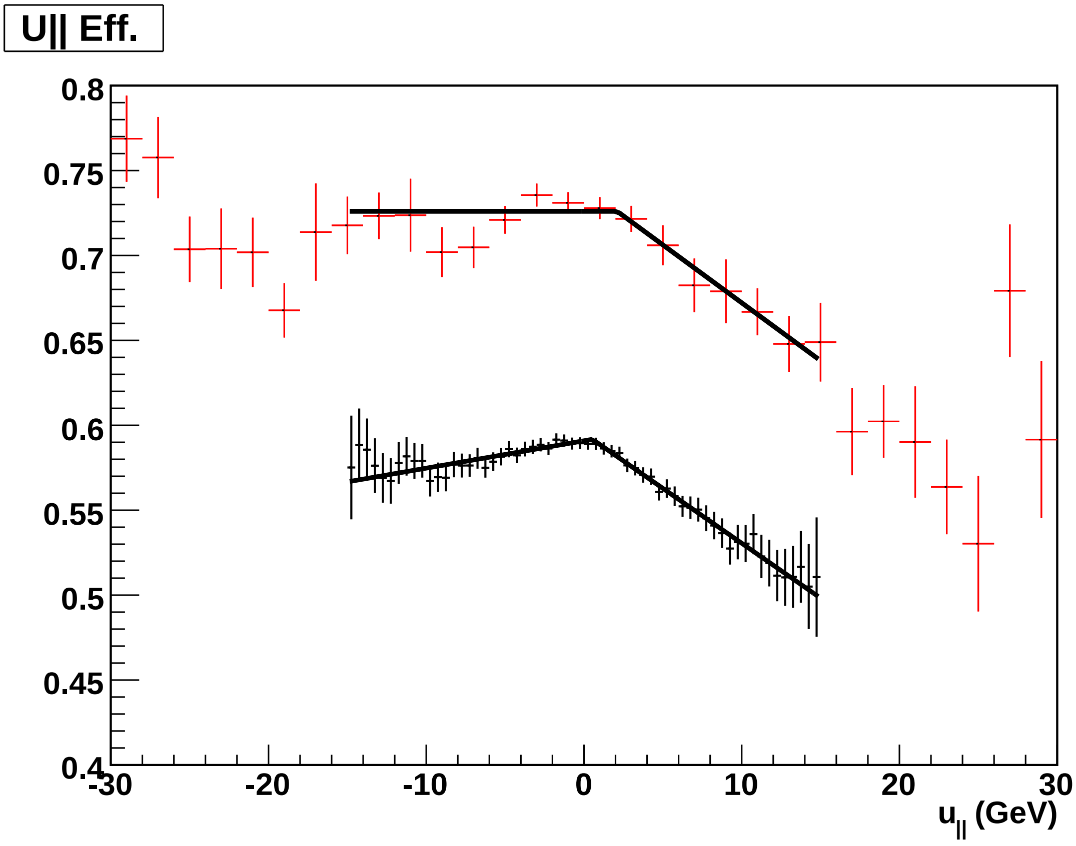

Figure 7.16. $u_{\|}$ efficiency from Tag and Probe for the data (red) and the fast Monte-Carlo(black) for RunIIb.

blinding offset from our W boson comparison plots. In lieu of showing all 64 (and their χ distributions), I will show the recoil transverse momentum, boson transverse momentum,

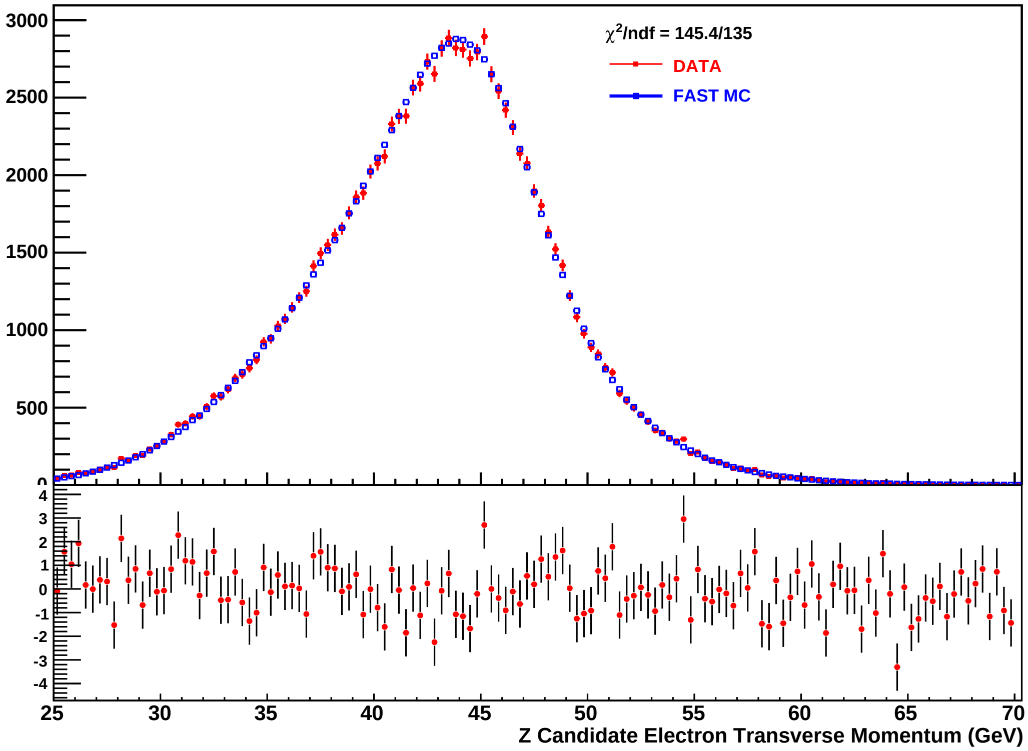

Figure 7.17. Transverse momentum distribution of central electrons from Z boson decays (The red histogram is data, and the blue is our fast simulation).

and electron transverse momentum plots here. These plots relate directly to the variables which are sensitive to the W boson mass, while our other plots mainly verify that we describe the data well enough to attempt to describe the W boson decay products which have different kinematics.

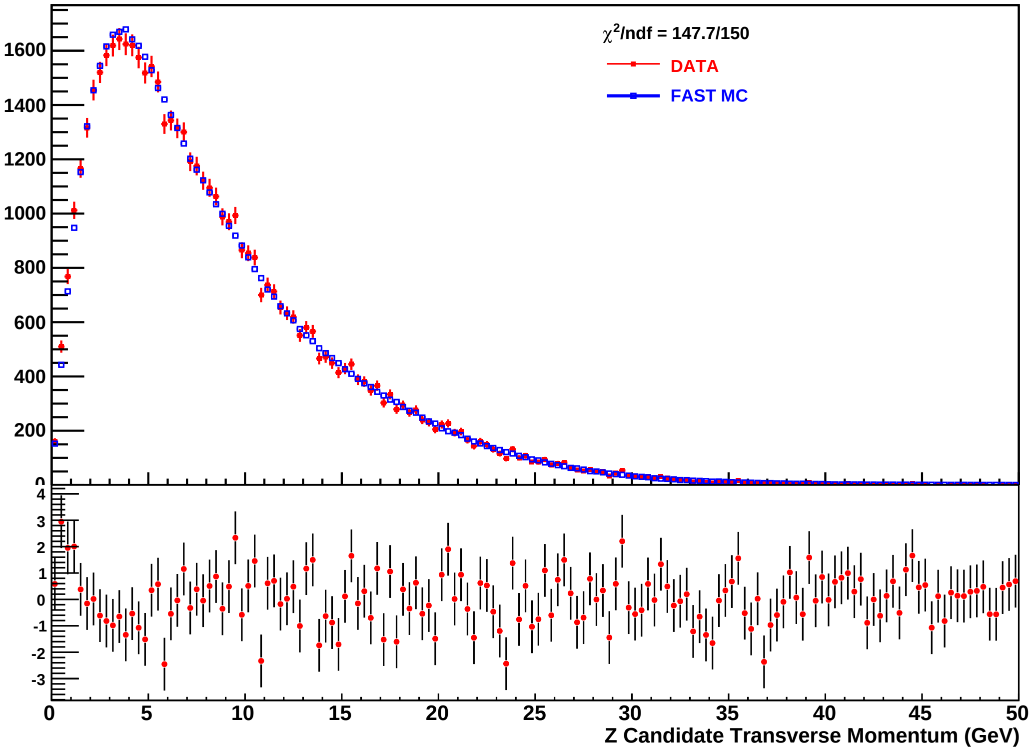

Figure 7.18. Comparison between the data and fast Monte-Carlo Z boson transverse momentum distributions. The difference visible in the χ distribution at the low end is a sign that the value of g_2 in Resbos needs to be tuned. We have verified this with an independent high statistics study.

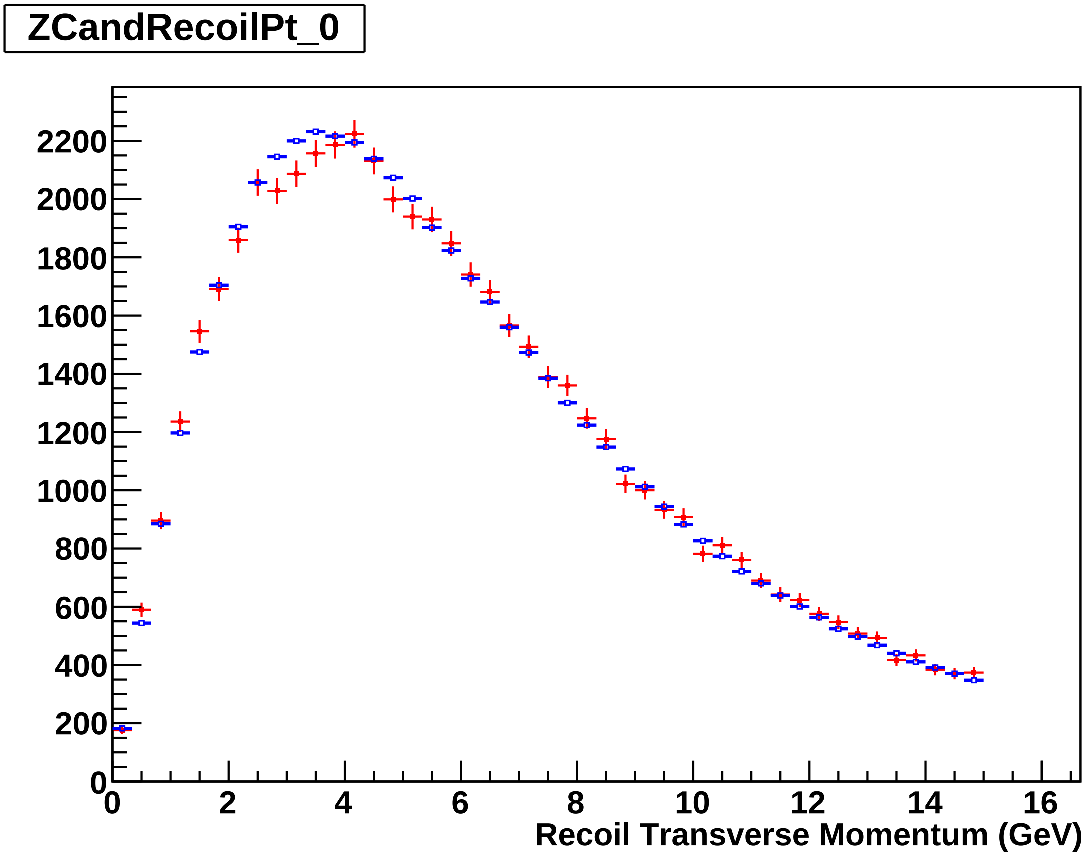

Figure 7.19. Hadronic recoil transverse momentum from Z boson candidates for data (blue) and fast Monte-Carlo (red).

CHAPTER 8

Background Estimations

There are three sources of backgrounds to $W \to e\nu$ events. Events where one electron from the Z boson decay is not properly identified, QCD di-jet events where a QCD jet is incorrectly reconstructed as an electron, and $W \to \tau\nu$ events, since the τ may decay into an electron and additional neutrinos. For the background component from $Z \to ee$ and $W \to e\tau$ events we determine a background shape, and fraction (described below), and then add the correctly normalized distribution to the signal from our fast Monte-Carlo simulation. For the QCD background estimation we rely on a calculation based on the efficiency and fake rate of electrons and QCD jets respectively to pass our cuts.

8.1. W → $\tau\nu$ Background

The background from W → $\tau\nu$ events is determined from a Pythia and GEANT based Monte-Carlo study of these events. The shape of the background is determined by directly applying our analysis selection cuts to the sample, while the background fraction is determined as the ratio of the (acceptance × efficiency) of the $W \to \tau\nu$ sample to pass our selection cuts to the (acceptance × efficiency) of the $W \to e\nu$ sample to pass our selection cuts.

$$f_{\tau\nu} = \left(\frac{N_{after\ selection}}{N_{generated}}\right)_{bkg} \div \left(\frac{N_{generated}}{N_{after\ selection}}\right)_{sig} \tag{8.1}$$

The $W \to \tau\nu \to e\nu\nu\nu$ background fraction is found to be 0.0201817 ± 0.000059.

8.2. $Z \to ee$ Background

The contribution to the background component from $Z \to$ ee events occurs when one of the electrons either escapes the detector or is incorrectly reconstructed and thus fakes large missing E_T. The largest source of this contribution is the case where one of the electrons falls into the ICD region. In order to determine the background contribution due to this effect we identify $Z \to ee$ candidate events that pass $W \to e\nu$ selection by looking for QCD jets in the ICD, or tracks pointing the ICD which are back-to-back in ϕ with the EM cluster that survived our analysis cuts. We also require that the 2 object invariant mass is within a window about the Z boson pole mass, 70 < M(e,Track) < 110 GeV, and 60 < M(e,Jet) < 110 GeV. Both of these selection criteria give compatible background shapes. In order to determine the background fraction for these events we determine the efficiency for jet identification using the tag and probe method again where the probe is a track pointing at the ICD which gives us the total efficiency for finding QCD jets. The background fraction is:

$$f_Z = \frac{\epsilon_{jet} N(e, Jet)}{N_W}, \tag{8.2}$$

where ϵ_{jet} is the efficiency for finding QCD jets. f_Z is found to be: $1.08 \pm 0.02\%$

8.3. QCD Background

QCD di-jet events can fake our signal if a jet is incorrectly identified as an electron and some of the energy in the calorimeter is mis-measured. Although the probability for this to take place is small the large cross section for QCD at the Tevatron leads to a significant contribution to our background. To estimate the QCD background we define a set of linear equations:

$$\begin{aligned} N &= N_W + N_{QCD} \\ N_{trk} &= \epsilon_{trk} N_W + f_{QCD} N_{QCD} \end{aligned}$$

where N_{trk} represents the number of events which pass our full set of selection cuts, N is the number of events which pass all our selection cuts except the tight track match requirement (P(χ^2)$>$ 0.01, a hit in the SMT, and track based $p_T > 10$ GeV). ϵ_{trk} is the efficiency for an electron to pass the tight track match requirement and f_{QCD} is the probability that a QCD jet which has passed all our selection cuts except for the track match requirement, will do so. ϵ_{trk} is determined using the tag and probe method, as described earlier. f_{QCD} is determined from a sample of events which have a QCD jet back-to-back with an EM cluster which has passed our standard selection cuts, except of course for the tight track match. This object is most likely a QCD jet. f_{QCD} is the fraction of these events where the 'EM cluster' passes the track match requirement. In order to reduce the possibility that we have selected a real electron from the decay of a W boson, we consider events with missing transverse energy $<$ 10 GeV when determining the fake rate. We find:

$$\begin{aligned} f_{QCD} &= 0.11 \pm 0.01 \; and, \\ \epsilon_{trk} &= 0.85 \pm 0.0008 \text{ (Binomial error only)} \end{aligned}$$

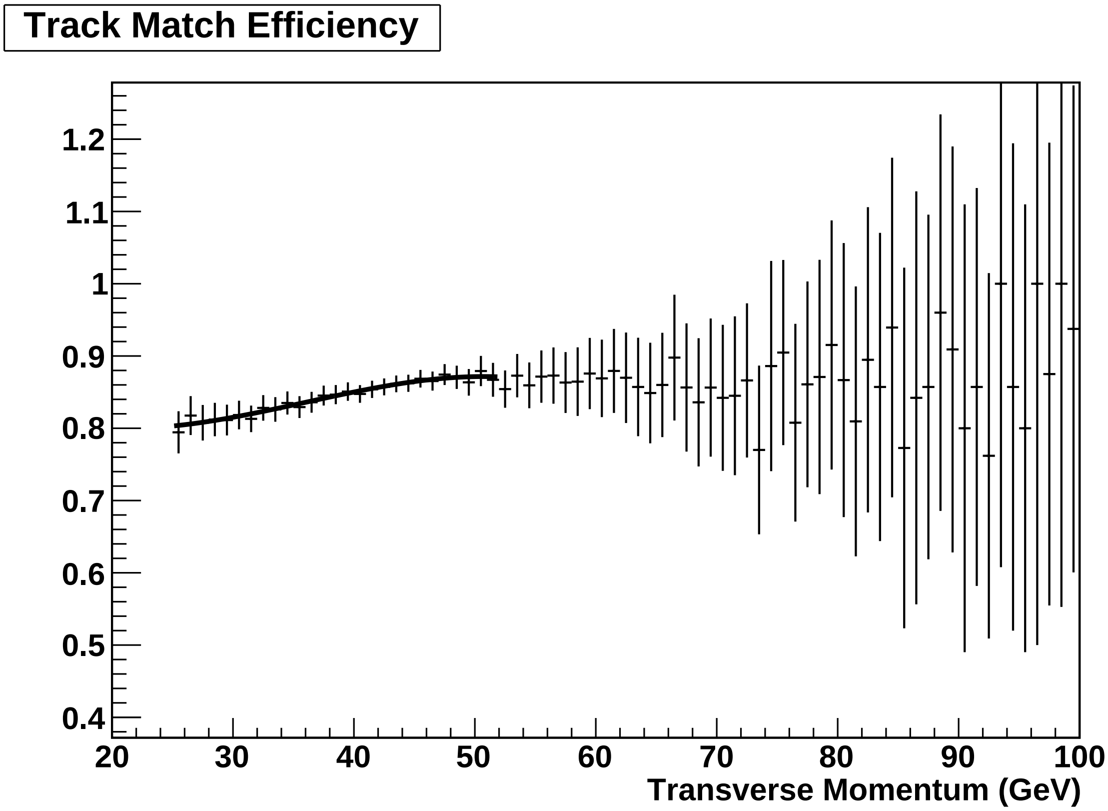

Figure 8.1. The efficiency for finding a track in bins of transverse momentum, determined from Tag and Probe. Above p_T of 55 GeV the efficiency is fixed to its value at 55 GeV which is consistent with the data.

In practice we know that the track matching efficiency is not constant, and in particular that it varies with transverse momentum. Instead of calculating one global background fraction we determine the efficiency in transverse momentum bins, where we determine our efficiency in transverse momentum bins using the Tag and Probe method once again. The dependence of the efficiency on transverse momentum is shown in figure 8.1. Using this method we estimate the background due to QCD to be $1.9 \pm 0.08\%$.

8.4. Combining the Backgrounds

When fitting for the W Boson mass we begin with two histograms. One consisting of the data which pass our full set of selection cuts, and one consisting of the output of our fast Monte-Carlo which provides the shape of the distribution from data without any backgrounds. Since for the $W \to \tau\nu$ and $Z \to ee$ backgrounds we have a shape and a normalization relative to the yield of expected signal events, we simply normalize the histograms correctly and add them to the fast Monte-Carlo prior to the comparison with data. The QCD background histogram is created bin by bin by solving the matrix of equations above.

The various background contributions are shown in figure 8.2, correctly normalized for the standard set of cuts.

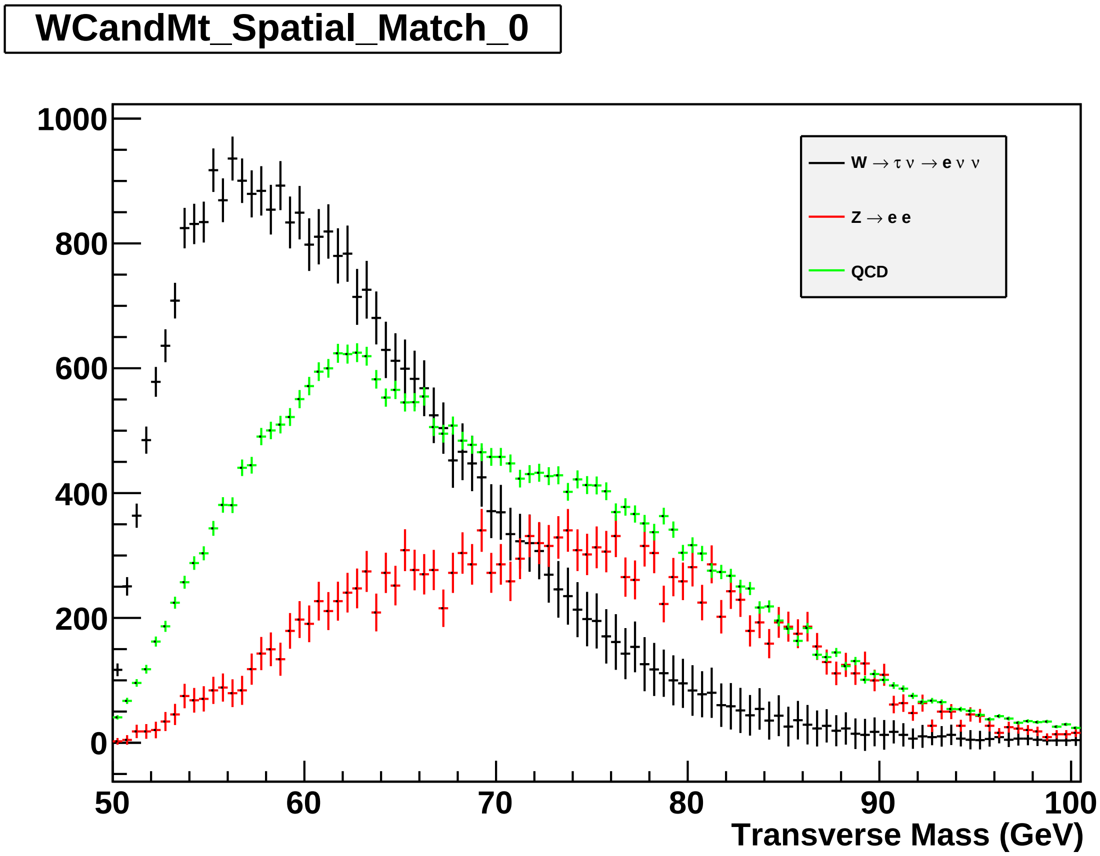

Figure 8.2. Properly normalized background distributions for m_T. The shape and yield determination is described in the test. The black histogram corresponds to the $W \to e\nu$ background, the red to the QCD background, and the green to the QCD background.

CHAPTER 9

Systematic Uncertainties

The uncertainties shown in Table 9.1 are believed to carry over from the previous analysis [**9**]:

- The theoretical uncertainty due to the simulation of QED effects.
- The same energy loss model is used and that uncertanty also remains the same.
- The W and Z boson electron energy loss difference uncertainty is due to the determination of the material in front of the calorimeter, and remains the same.

We have re-evaluated the PDF errors with the more recent CTEQ 6.6M PDF sets, this will be described below. The uncertainties due to the energy scale and the resolution for both electrons and hadrons is largely statistical in nature and has inproved substantially with this larger data sample. The full table of systematic uncertainty from the $1fb^{-1}$ measurement [**9**] is shown below in table 9.1:

9.1. General Method for Evaluation of Uncertainties

The uncertainties are determined using a large ensemble of simulated experiments with our fast Monte-Carlo for each of the 4 cases in which the parameter being studied is varied $\pm 1\sigma$ and $\pm 2\sigma$. We fit for the mass of the W boson for each of these pseudo experiments using our standard procedure. The difference between the true value of the mass and the mean resulting value from each of these sets of pseudo-experiments is determined as a function of the parameter being varied. This dependence is fit to a first order polynomial,

Source	$\sigma(m_W)$ MeV M_t	$\sigma(m_W)$ MeV e_{pT}	$\sigma(m_W)$ MeV MET
Experimental			
Electron Energy Scale	34	34	34
Electron Energy Resolution Model	2	2	3
Electron Energy Nonlinearity	4	6	7
W and Z Electron energy loss differences	4	4	4
Recoil Model	6	12	20
Electron Efficiencies	5	6	5
Backgrounds	2	5	4
Experimental Total	35	37	41
W production and decay model			
PDF	10	11	11
QED	7	7	9
Boson p_T	2	5	2
W model Total	12	14	14
Total	37	40	43

Table 9.1. Systematic uncertainties on the W bosson mass results from the RunIIa analysis. The dominant systematic uncertainty comes from the electron energy scale, and this is determined by the statistical power of the Z boson event sample.

the slope of which is used in the usual error propagation formula:

$$\sigma^2_{M_W}(X) = \left(\frac{\partial M_W}{\partial X}\right)^2 \sigma^2_X, \tag{9.1}$$

where $\frac{\partial M_W}{\partial X}$ is the slope and σ_X is the uncertainty on parameter X. In the case that we need to consider correlations between the matrices we use:

$$\sigma^2_{M_W}(X_1, X_2) = \left(\frac{\partial M_W}{\partial X_1}\right)^2 \sigma^2_{X_1} + \left(\frac{\partial M_W}{\partial X_2}\right)^2 \sigma^2_{X_2} + 2\sigma_{12}\left(\frac{\partial M_W}{\partial X_1}\right)\left(\frac{\partial M_W}{\partial X_2}\right) \tag{9.2}$$

where σ_{12} is the covariance.

9.2. Energy Scale and Offset Uncertainty

The uncertainty due to the EM scale and offset parameters are anti-correlated, as described in chapter 6 the parameters used are:

- $\alpha_{EM} = 1.0162 \pm 0.0019$, and
- $\beta_{EM} = 0.0706 \pm 0.0144$ GeV with
- $\sigma_{\alpha\beta} =$ -0.769

we find: $\frac{\partial M_W}{\partial \alpha_{EM}} \sigma_\alpha = 0.015$ GeV, and $\frac{\partial M_W}{\partial \beta_{EM}} \sigma_\beta = 0.0216$ GeV. and thus the contribution to the uncertainty due to the variation in these parameters is:

$\sigma_{M_W}(\alpha_{EM}, \beta_{EM}) = 14$ MeV

9.3. EM Resolution Uncertainty

As described in chapter 6 the constant term of the resolution C_{EM} is $C_{EM} = 0.0198 \pm 0.0006$. The uncertainty on m_W due to the error on C_{EM} is 3 MeV.

9.4. Recoil Scale and Resolution Uncertainty

Using the method described above, and the parameters described in chapter 6, we find an uncertainty due to the modelling of the recoil resolution to be 8.4 MeV, and on the Recoil Scale to be 16 MeV. Both of these errors seem too large in comparison with the numbers from RunIIa, and with our expectation for the dependence of the W mass on the recoil response. This will need to be investigated further. We see that the largest contributor to this uncertainty is the τ_{had} parameter, which we are able to determine through studies of energy flow. For the response parameters we have:

- $\left(\frac{\partial M_W}{\partial \tau}\right)\sigma_\tau = 0.02226$

- $\left(\frac{\partial M_W}{\partial \text{RelScale}}\right)\sigma_{\text{RelScale}} = -0.0085$
- $\left(\frac{\partial M_W}{\partial \text{RelOffset}}\right)\sigma_{\text{RelOffset}} = 0.0092$

9.5. Efficiency Uncertainty

The most significant efficiency related uncertainty is due to the SET efficiency ratio correction. Variation of the SET efficiency ratio correction lead to an absurdly large uncertainty, which must be due to an error in the estimation. Assuming that the uncertainty due to α_{EM} and β_{EM} is still the dominant EM related uncertainty I will estimate the total error asuming that the contribution from the SET efficiency in 10 MeV. The reader should be aware that the uncertainty analysis on this measurement is incomplete.

9.6. Background Uncertainty

The background uncertainty is determined separately for each of the background components ($W \to \tau\nu \to e\nu\nu$, $Z \to ee$, and QCD) by varying the the number of events in each bin by ($\pm\sigma$) and fitting for the W mass. The maximum change to the fitted W mass is used as the uncertainty due to the background under study. The errors due to each of the three background components is added in quadrature to give the final background uncertainty.

The uncertainties due to to each contribution are added in quadrature to give the total background uncertainty shown below in table 9.2.

Source	$\sigma(m_W)$ MeV M_t
Z → ee	3
W → $\tau\nu$	2
QCD	1
Total	4

Table 9.2. Uncertainty on W boson mass from transverse mass distribution due to background contributions

9.7. PDF Uncertainty

The change on the W boson mass due to the variation of the PDF eigenvectors within their confidence limit provides a determination of the error on the W mass determination due to the PDF set. The total symmetric error is evaluated as [**10**]:

$$\text{Final PDF uncertainty} = \frac{1}{2}\frac{1}{1.6}\sqrt{\sum_i (\triangle M_W(+)_i - \triangle M_W(-)_i)^2} \tag{9.3}$$

The factor of 1.6 is included to because we cite the standard 68% confidence level and the eigenvectors are varied within their 90% confidence level. We find a total Error of 11 MeV. The individual mass variation per PDF error set are shown in figure 9.1.

9.8. Uncertainty Due to Boson p_T

Our data points to a value of g_2 which is different from the world average value by twice as much as the uncertainty on g_2. We are unfortunately not able to generate enough events with the preferred value of g_2 for this analysis. Since the RunIIa uncertainty propogation to the W boson mass was based on the world average uncertainty on g_2 we choose to double this from 2 to 4 MeV.

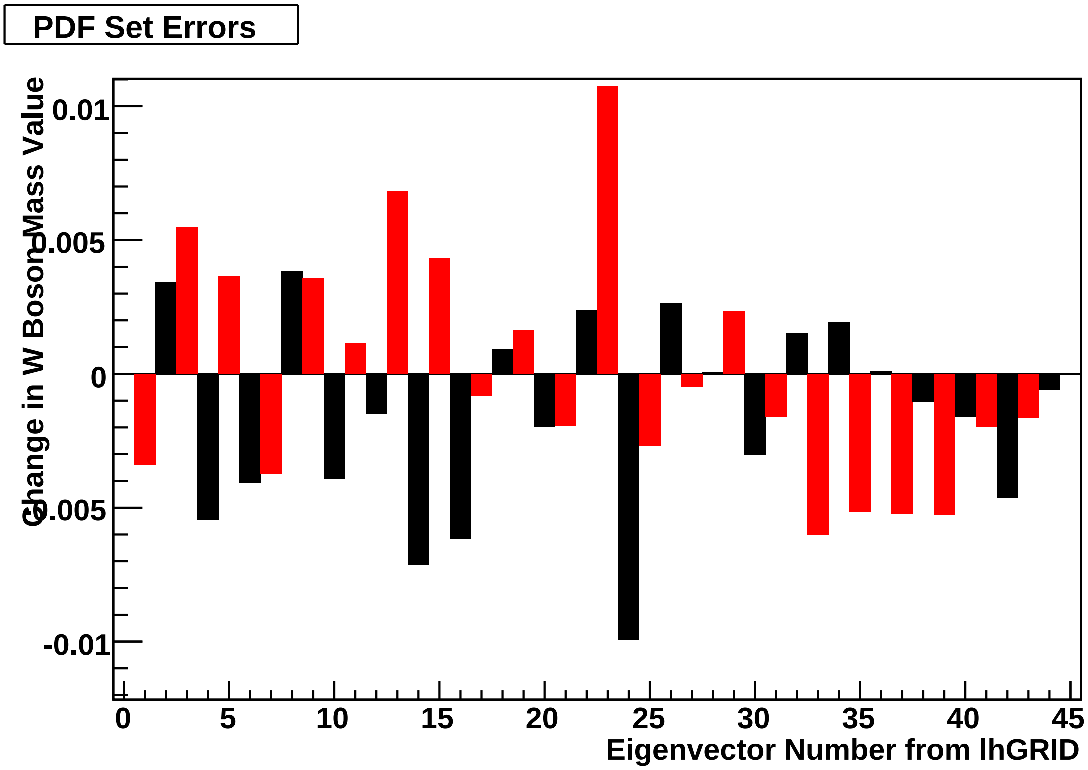

Figure 9.1. Change in measured W Mass (m_W^i - m_W^0) as a function of the PDF error set being used

9.9. Total Systematic Uncertainty

The total systematic and theoretical uncertainty, based on the estimation described above is conservatively estimated to be 32 MeV with the breakdown of the contributing factors shown in table 9.3.

Source	$\sigma(m_W)$ MeV M_t
Experimental	
Electron Energy Scale	14
Electron Energy Resolution Model	3
Electron Energy Nonlinearity	4
W and Z Electron energy loss difference	4
Recoil Model	18
Electron Efficiencies	0 / 10.
Backgrounds	2
Experimental Total	27 / 29
W production and decay model	
PDF	11
QED	7
Boson p_T	4
W model Total	14
Total	30 / 32

Table 9.3. Systematic uncertainties on the W mass results in the transverse mass channel. The dominant systematic uncertainty comes from the Recoil Model, which is unexpected and requires further investigation. The systematic uncertainty due to electron efficiencies has not been calculated due to sstrange behaviour on the dependence, which is most likely due to an error by he analyzer. Total are calculated twice. Once assuming 0 for the electron efficiency, and once assume the value on 10 MeV, where we claim that the uncertainty due to the electron efficiencies should not be as large as that due to the energy scale.

CHAPTER 10

Result and Outlook

10.1. First Look at W Boson Data

10.1.1. The Control Sample

The comparison between our control sample (the Z boson data) and our simulation reproduced below in figures 10.1, 10.2, 10.3, 10.4, and 10.5 indicate that we have obtained a realistic model of the detector response with the limited statistics available to us. These two points are quite important before we consider a comparison with the W boson data:

- The Z Boson control plots show good agreement with the data – with the following caveats:

  We see a difference in the low transverse momentum region of the Z boson transverse momentum distribution, which shows signs of being related to an incorrect determination of the g_2 parameter describing the production cross section at low transverse momentum. This is not unexpected as our determination of g_2 was based on significantly smaller data samples.

  The width of the η_{imb} distribution defined in Chapter 6 in the bin of Z boson transverse momentum between 0 and 1 exhibits a three standard deviation difference between our simulation and the data.
- We have limited statistics

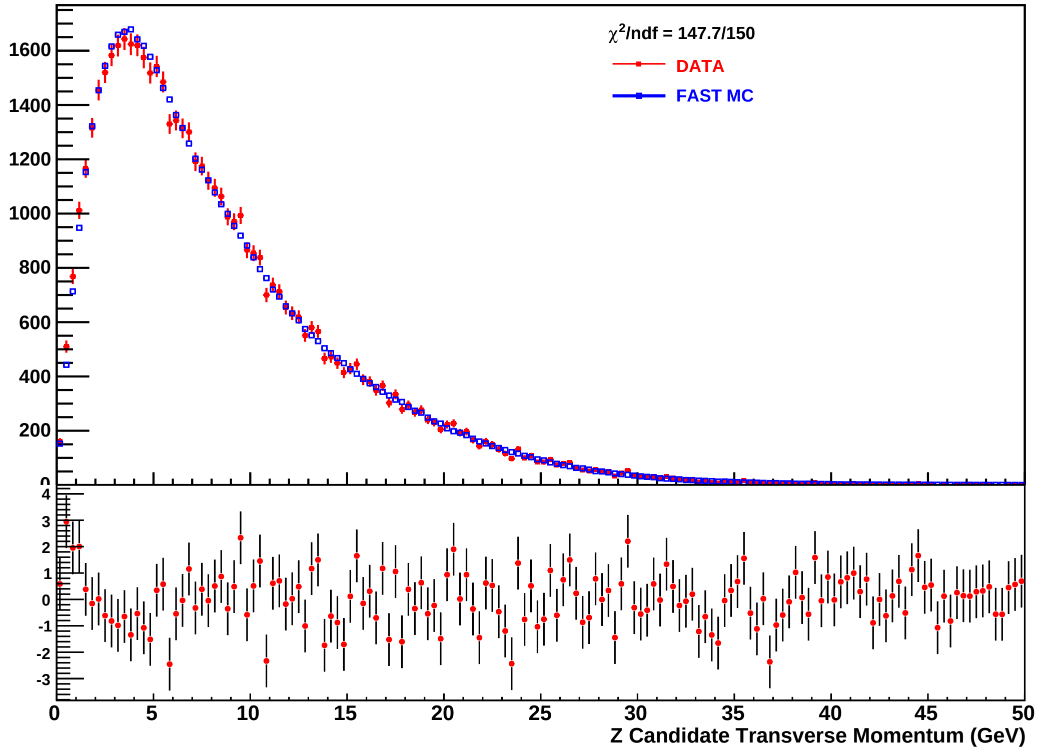

Figure 10.1. boson candidate transverse momentum. The data is shown in red, and the simulation in blue, along with the corresponding χ distribution.

The W boson sample consists of approximately one million, seven hundred thousand events.

The Z Boson (calibration sample) consists of approximately fifty-five thousand events.

Because of the low Z statistics it is possible that effects that are not significantly expressed in the calibration sample may be visible in the W boson data sample.

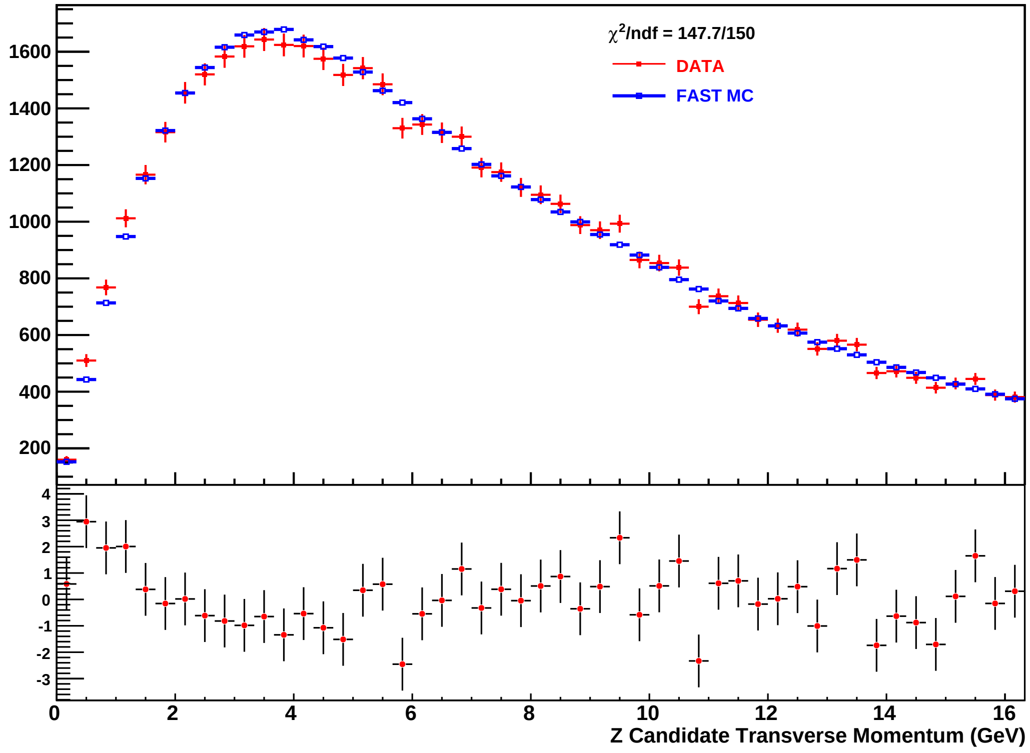

Figure 10.2. Z boson candidate transverse momentum for events with transverse momentum less than fifteen GeV. The data is shown in red, and the simulation in blue, along with the corresponding χ distribution.

10.1.2. W Boson Data with Standard Cuts

A comparison of the W boson data with our fast Monte-Carlo simulation is shown in figures 10.6, 10.7, 10.8, and 10.9, events were selected with our standard cuts as shown below:

- A track matched electron passing all quality cuts with $p_T > 25$ GeV and $|\eta_{det}| < 1.05$
- $MET > 25$ GeV
- $p_T^{rec} < 15$ GeV

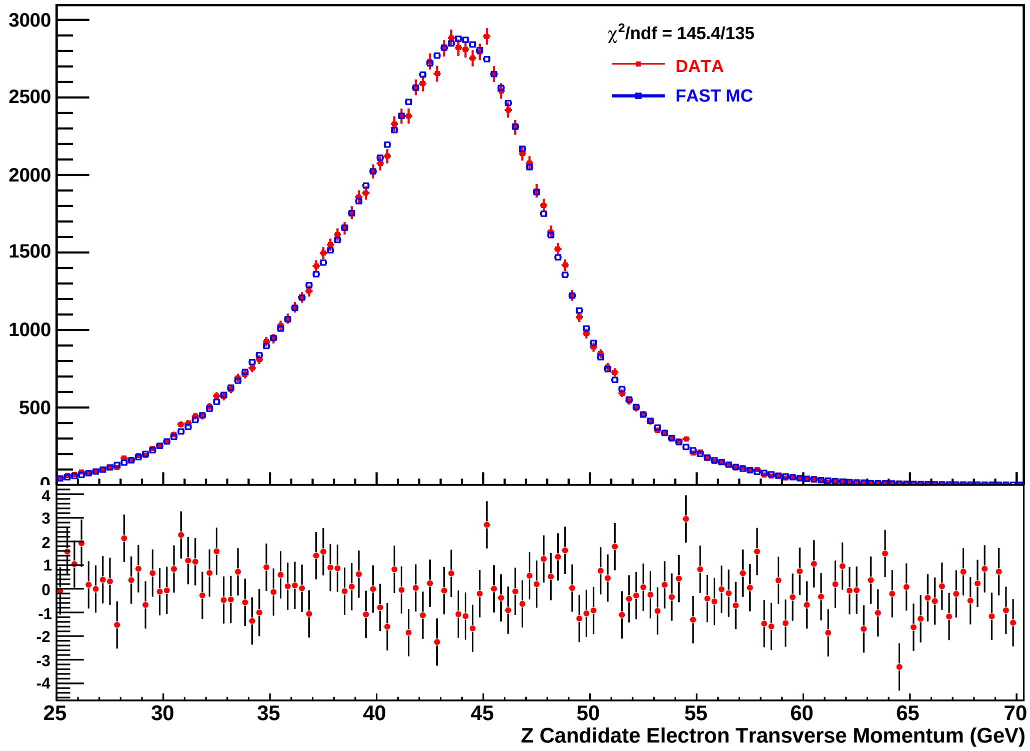

Figure 10.3. Electron transverse momentum distribution for Z boson candidates. The simulation is shown in blue with the data in red. The χ distribution is also shown.

- $50 < M_T < 200$ GeV

The disagreement in the boson transverse momentum distribution (figure 10.6) is expected and attributed to the g_2 parameter. In addition we see a large disagreement in the lepton transverse momentum distribution below 30 GeV, this is most likely due to an inefficiency which we have been unable to describe correctly, possible causes are that the $E1\_SHT27$ trigger eats into our signal region, or there is a Tag and Probe bias and our determination of the efficiency is not sufficient. To address this issue we will, for this preliminary result, raise the electron transverse momentum cut to 30 GeV.

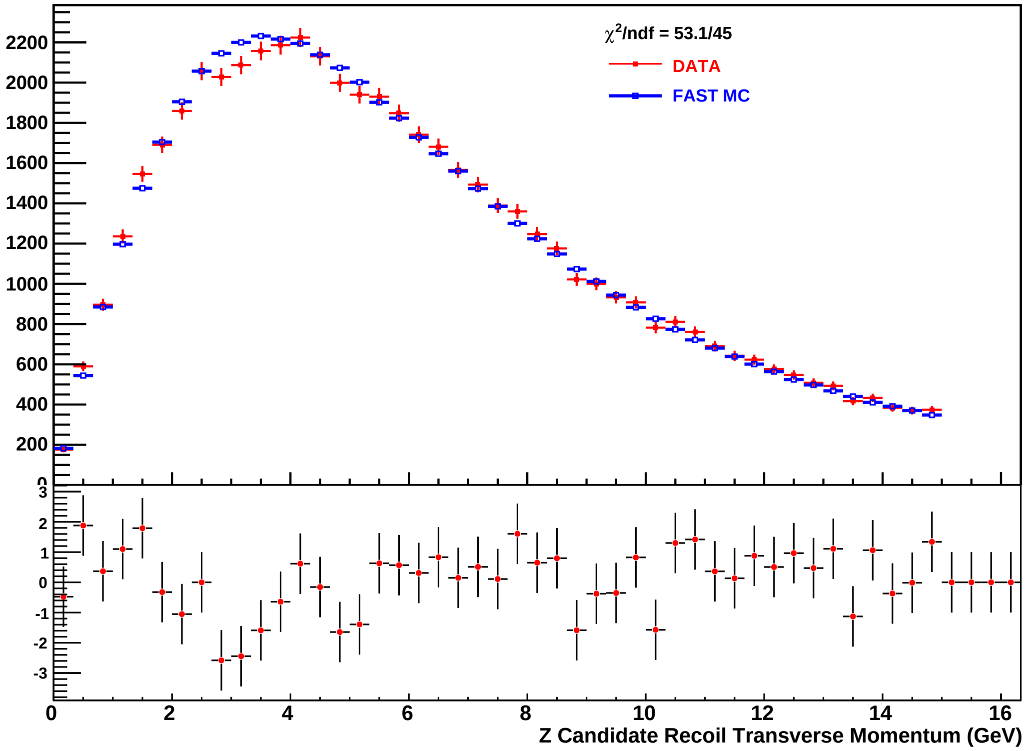

Figure 10.4. Recoil transverse momentum for Z boson candidate events, and the corresponding χ distribution. The blue points indicate our simulation, and the red points indicate our data.

10.1.3. W Boson Data with Modified Cuts

With our default cuts, our first look at the W boson data shows some striking features, which were not apparent from our Z control sample. This is not entirely unexpected as the yield of W events is significantly greater than for the Z events we use to develop our model. The obvious deficit in the low transverse momentum electron yield motivates us to raise the electron transverse momentum cut to 30 GeV before fitting for the W mass, explicitly we now require:

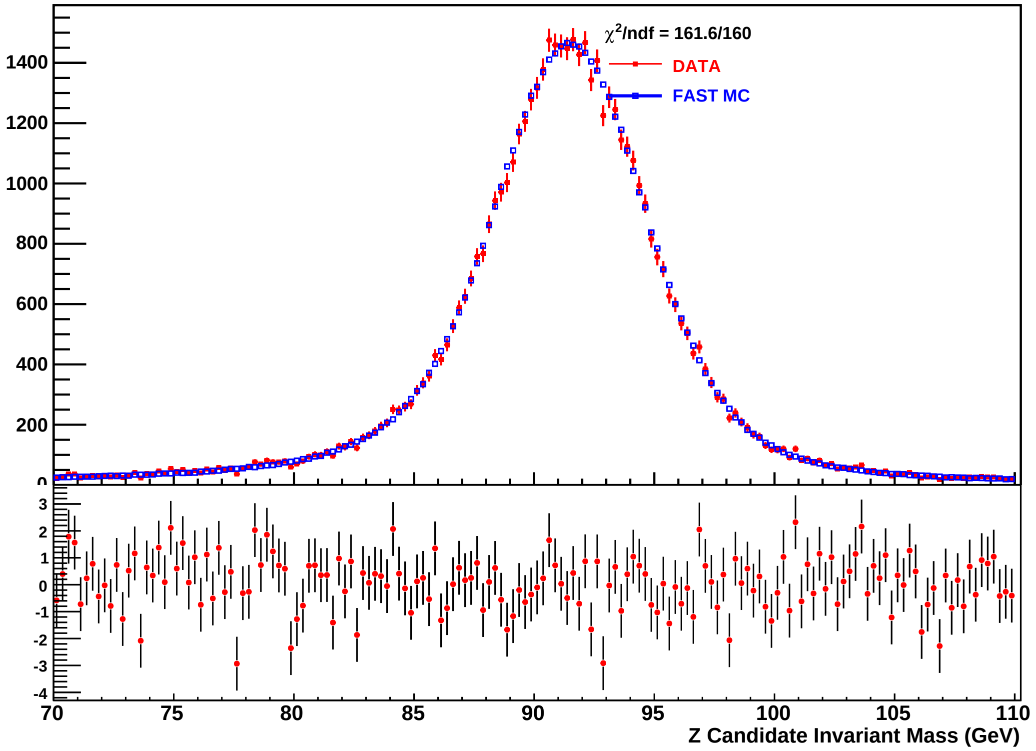

Figure 10.5. The invariant mass distribution for our calibration sample of Z boson candidates (red) compared to our simulation (blue), and the χ distribution.

- A track matched electron passing all quality cuts with $p_T > 30$GeV and $|\eta_{det}| < 1.05$,
- $MET > 25$ GeV,
- $p_T^{rec} < 15$ GeV, and
- $50 < M_T < 200$ GeV.

The discrepancy with the boson transverse momentum distribution (after the raised cuts, figure 10.10), which was apparent with our Z sample to a lesser extent, coupled with the structure in the peak of the electron transverse momentum (figure 10.11) lead us to believe

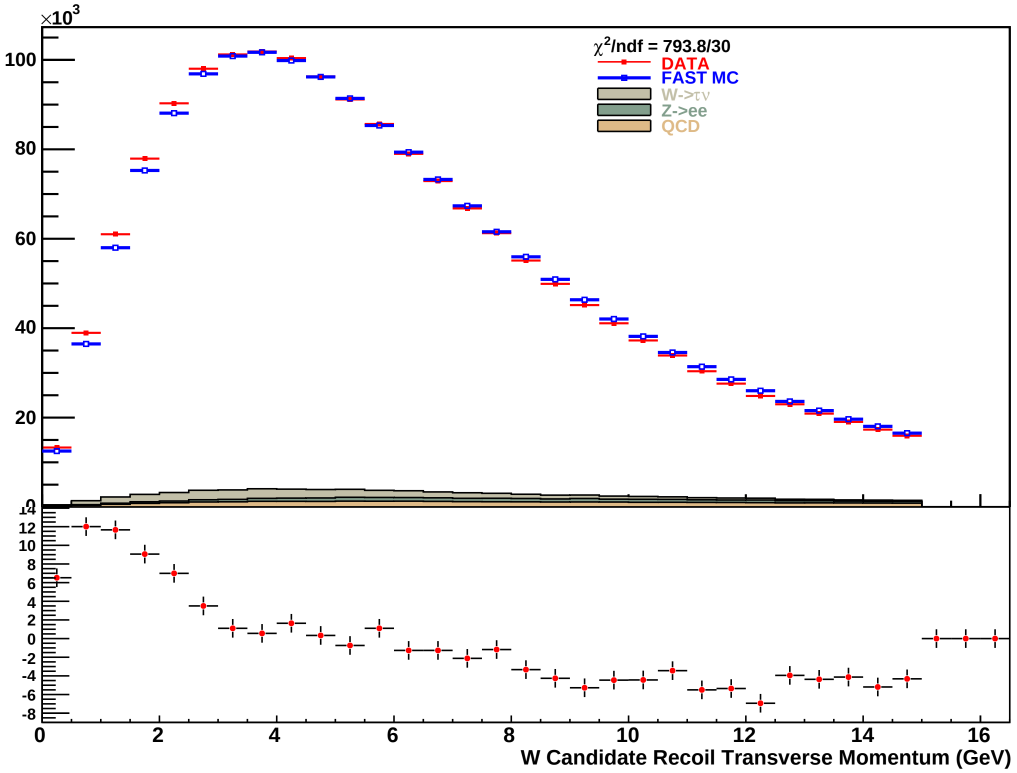

Figure 10.6. W boson candidate recoil transverse momentum distribution. The data is shown in red, and the simulation in blue, along with the corresponding χ distribution.

that the electron transverse momentum or the missing transverse energy (figure 10.12) distributions are not being reproduced accurately enough in our simulation to be used to fit for the W Boson mass. Figure 10.13 shows that the electron transverse momentum distribution is particularly sensitive to the generated boson transverse momentum distribution.

Ideally for a blind analysis we would want to understand the features of these distributions, and have them all agree before removing the blinding offset. However the

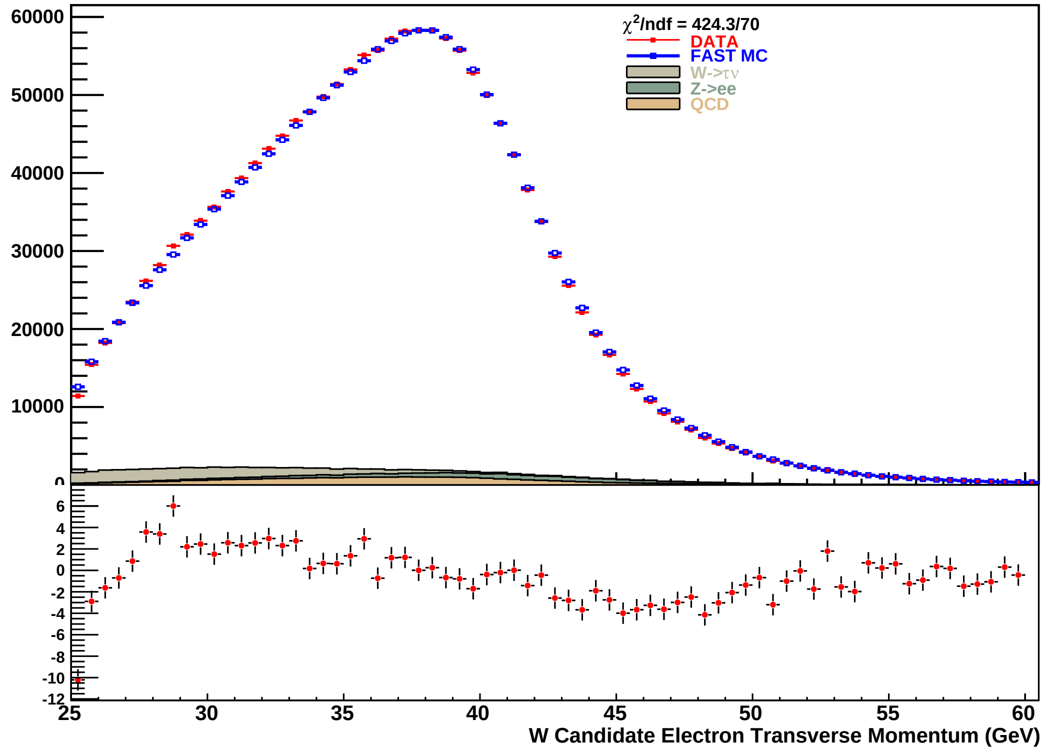

Figure 10.7. W boson candidate electron transverse momentum distribution. The data is shown in red, and the simulation in blue, along with the corresponding χ distribution.

agreement of the best-fit transverse mass distribution to the data is good, and the discrepancies we see are primarily related to the Boson transverse momentum distribution, which the transverse mass is less sensitive to. (This can been seen from figure 10.14, which shows that the transverse mass distribution is more sensitive to the response of the detector than the intrinsic boson transverse momentum distribution). We are investigating whether a change in the g_2 parameter will help to restore consistency of the electron transverse momentum and missing transverse energy distributions. I will proceed with the measurement of the W boson mass by fitting the transverse mass distribution.

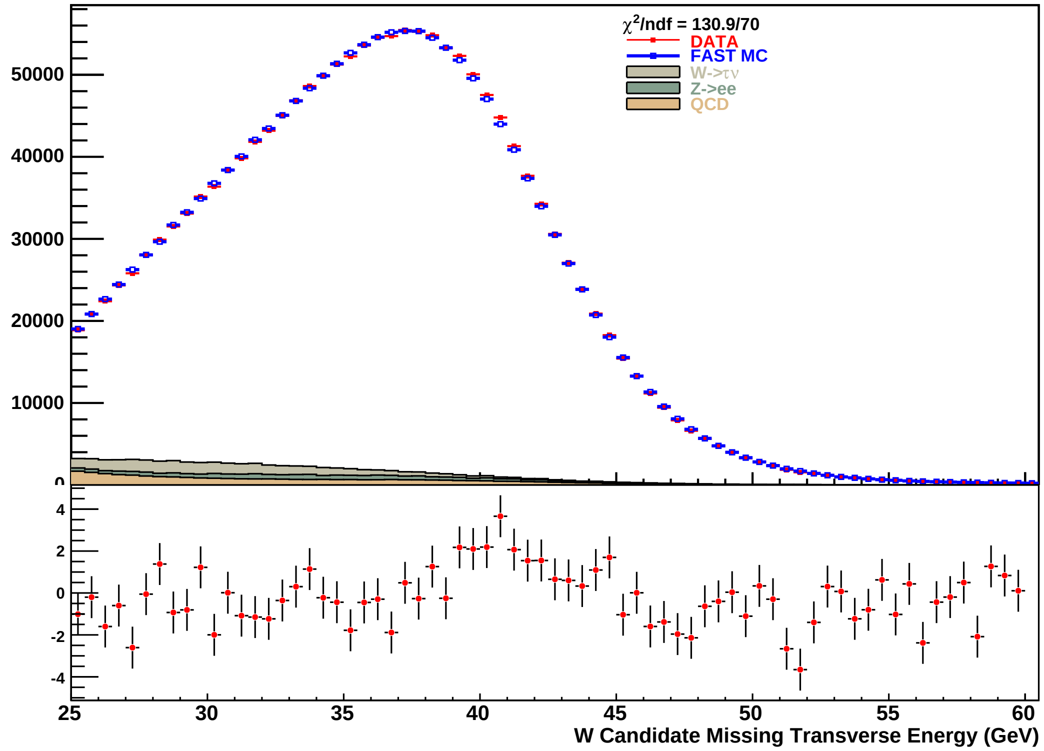

Figure 10.8. W boson candidate missing transverse energy distribution. The data is shown in red, and the simulation in blue, along with the corresponding χ distribution.

10.2. Blind W Mass Result

The true value of the mass of the W boson (as determined from our template fit to the data) has been hidden from us by the addition of an unknown offset to the result returned by the fit algorithm. This is done to remove any bias on the part of the analyzers working on the experiment. For completeness we include the value (mass plus blinding offset) returned from our fitter. The fit range in 65 to 90 GeV in m_T. We find a (blinded) mass of M(W)=81.508 ± 0.013 (stat) ± .029 (syst – estimated) ± 0.014 (Theory) GeV with a $\chi^2/NDF = 46/51$ from the W transverse mass distribution (figure 10.15).

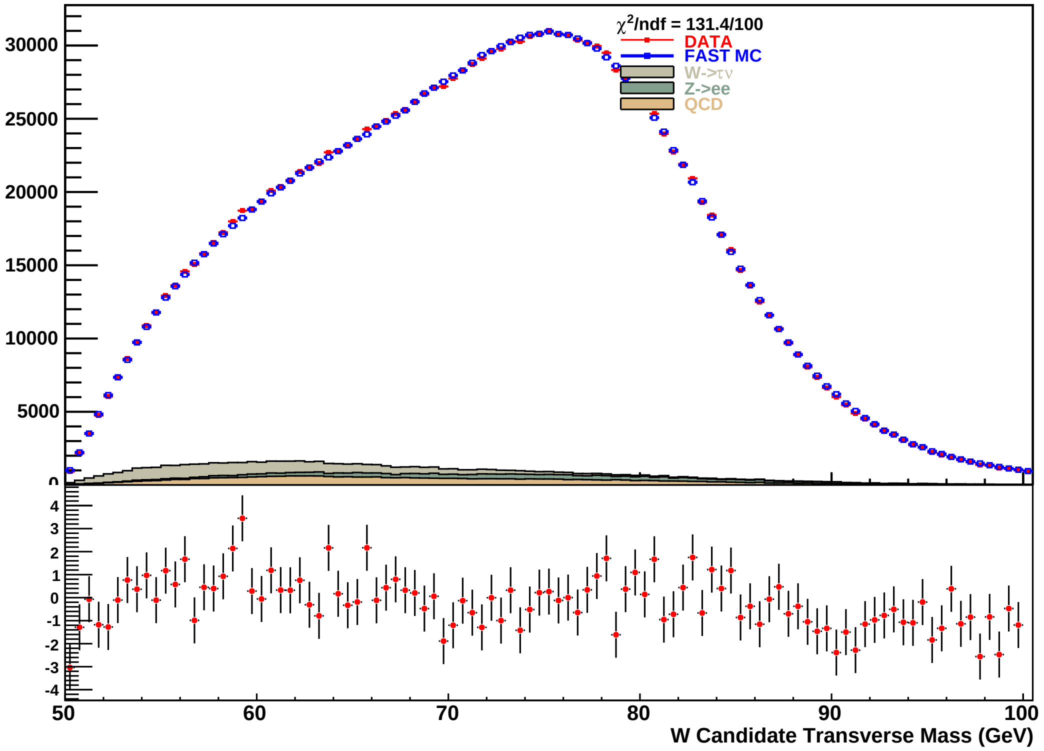

Figure 10.9. W boson candidate transverse mass distribution. The data is shown in red, and the simulation in blue, along with the corresponding χ distribution.

10.3. Un-Blinded W Mass Result

Removing the blinding offset we have a measurement for the mass of the W boson:

- M(W)=80.425 ± 0.013 (stat) ± .029 (syst − estimated) ± 0.014 (Theory)

The total uncertainty (combined in quadrature) is 35 MeV.

10.4. Conclusion and Outlook

A presentation by Jan Stark [**43**] to the DØ collaboration about the RunIIa W mass measurement states “This is **not** a simple redo of the DØ RunI analysis,” and proceeds

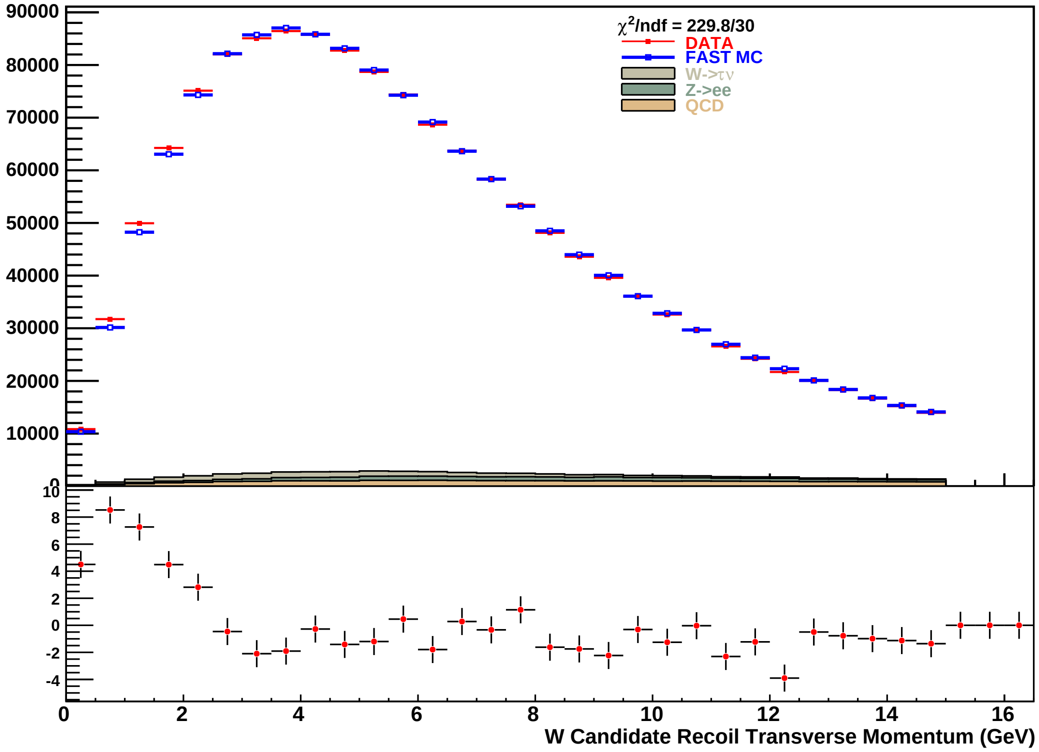

Figure 10.10. This comparison between the W boson data (in red) and our fast Monte-Carlo (plus background) (blue) shows that we do not properly describe the low transverse momentum region.

to describe the difficulties involved in the measurement. This analysis was intended to be a simple redo of the DØ RunIIa analysis, with larger data samples helping drive down our uncertainties. There can be no doubt that this analysis bears more in common with the RunIIa analysis than the RunIIa analysis does with the RunI analysis. The change in the environment at the Tevatron has been significant enough to require more than a 'simple redo' approach. We have shown however that DØ is extremely close to having an updated measurement of the W boson mass. While the discrepancy in the low tail of the electron transverse momentum distribution will possibly hold up a publication, For the

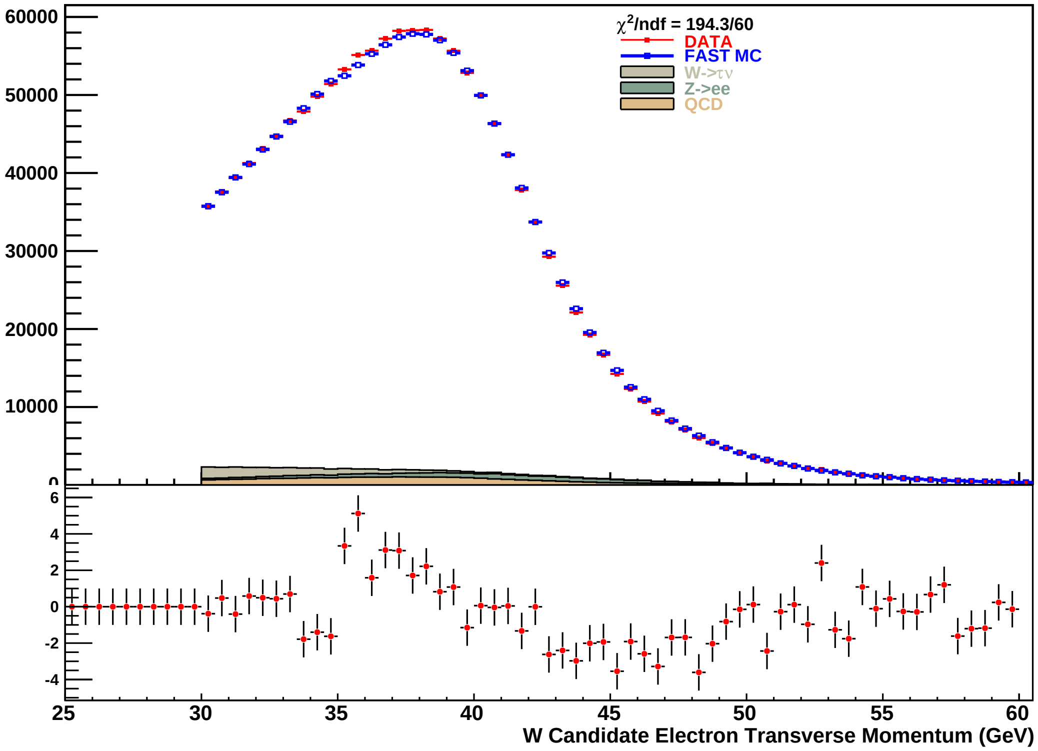

Figure 10.11. The electron transverse momentum distribution for W data (blue) and out fast Monte-Carlo (with background). The visible structure is related to our SET efficiency. As shown in figure 10.10 the boson transverse momentum distribution is not well reproduced by our simulation, and thus we do not expect the electron transverse momentum distribution to match.

purposes of this work (assuming that the SET efficiency error determination is due to a minor oversight) we are a few thousand CPU hours away from a complete measurement. Combination of this result with previous measurements leads to the following averages:

- Tevatron Average – 80.423 ± 0.025 GeV
- World Average – 80.406 ± 0.0020 GeV

We expect a near future publication worthy result from the DØ collaboration which will carry the Tevatron average uncertainty below 25 MeV, and the world average below 20

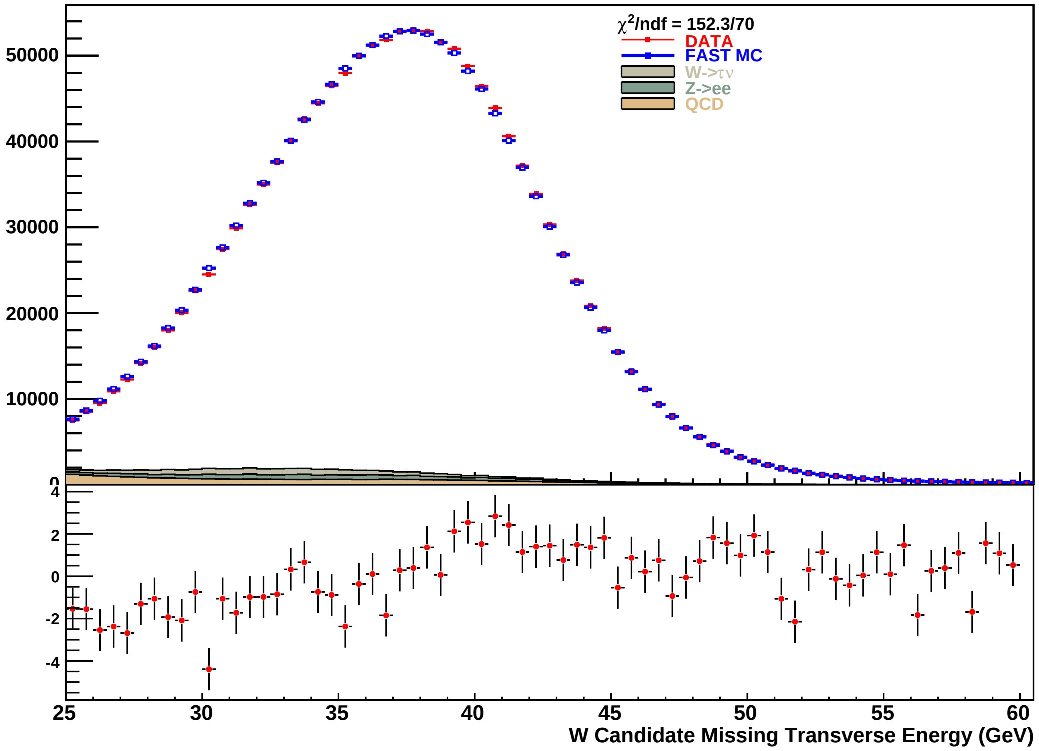

Figure 10.12. The missing transverse momentum distribution of data (red) and our signal plus background (blue). The difference between the two distributions is too large for us to attempt a W mass measurement from this distribution.

MeV, hopefully increasing the tension between indirect and (the lack of) direct evidence for the Higgs boson. As DØ accumulates data we aim for a single experiment measurement with an uncertainty close to 20 MeV.

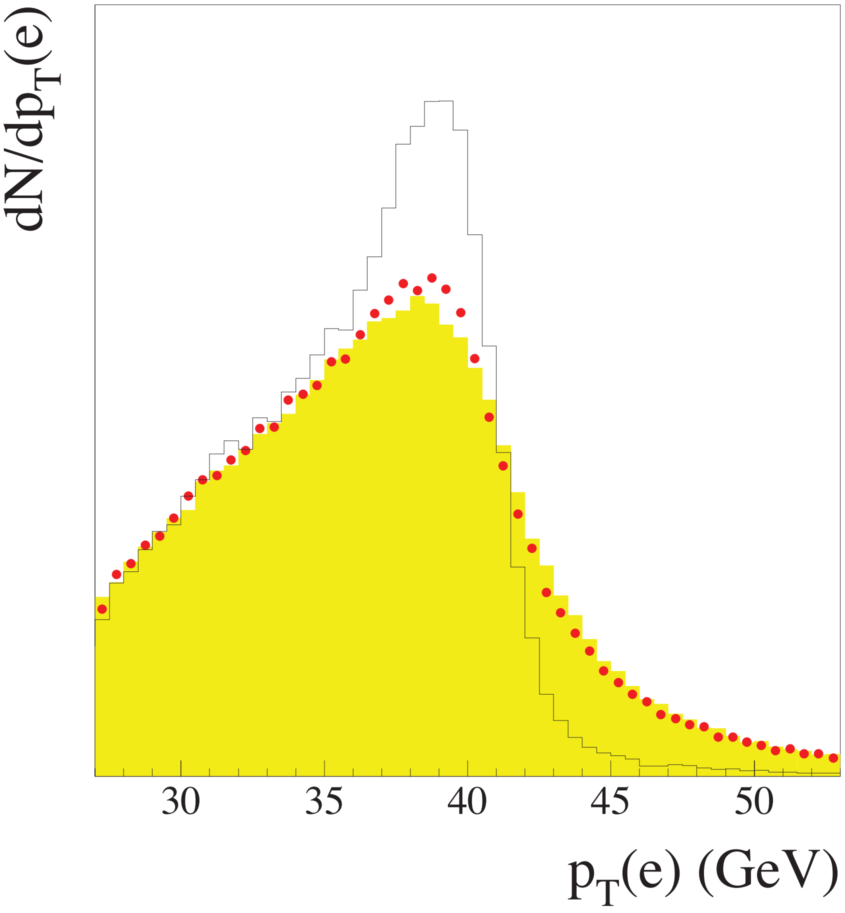

Figure 10.13. A simulated electron transverse momentum distribution. The black histogram describes a boson with no transverse momentum distribution or detector resolution effects. The red histogram describes a boson with a realistic transverse momentum distribution. The yellow histogram includes the effects of a realistic transverse momentum distribution and detector resolution. This illustrates that the electron transverse momentum distribution is sensitive to the boson transverse momentum distribution.

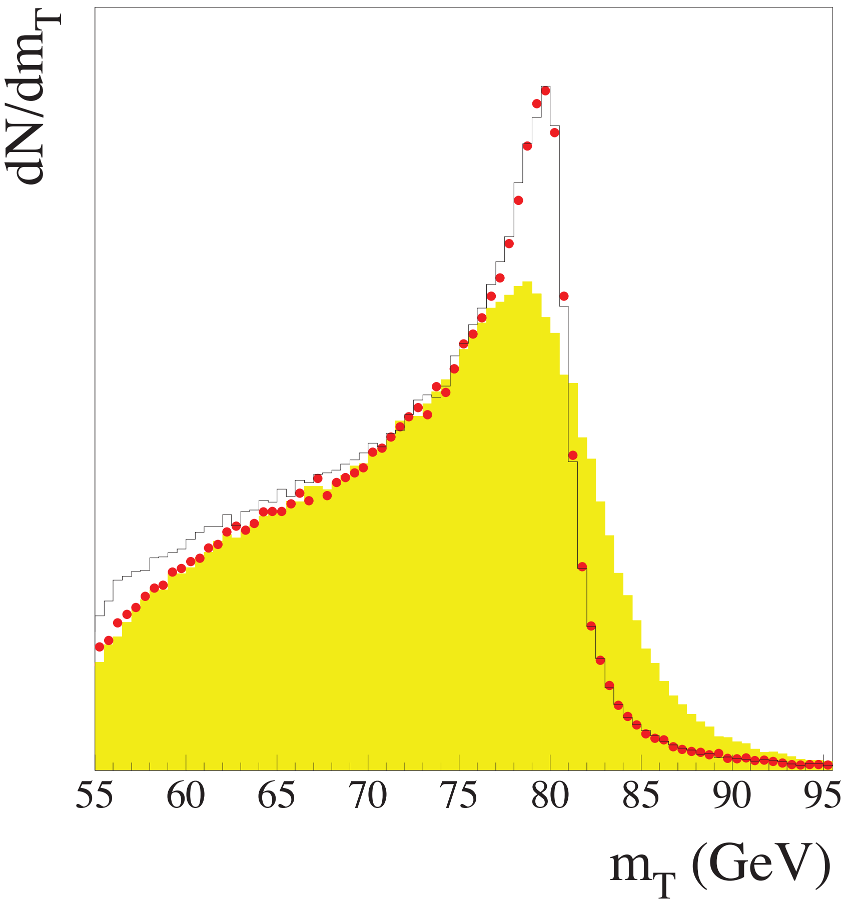

Figure 10.14. A simulated transverse mass distribution. The black histogram describes a boson with no transverse momentum distribution or detector resolution effects. The red histogram describes a boson with a realistic transverse momentum distribution. The yellow histogram includes the effects of a realistic transverse momentum distribution and detector resolution. This illustrates that the transverse mass distribution is sensitive to the resolution of the detector, but not very sensitive to the boson transverse momentum distribution.

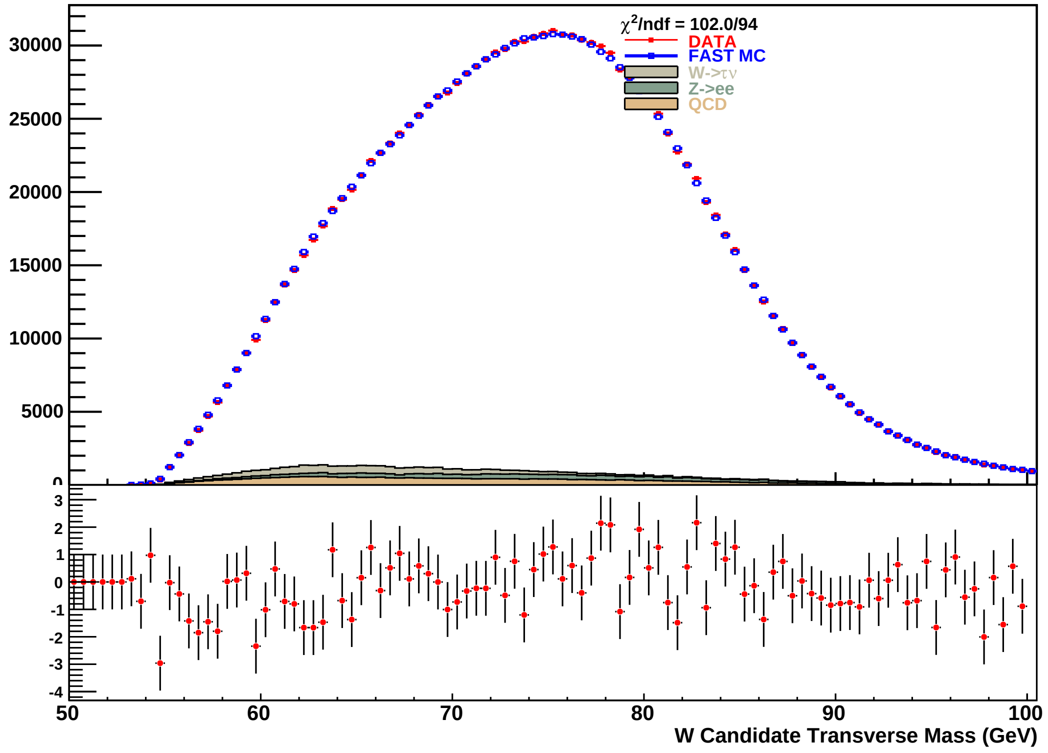

Figure 10.15. The best fit template from our fast Monte-Carlo (in blue) compared the data. Although there is structure in the χ distribution the agreement is good. The fit is performed over the range 65 – 90 GeV.

References

[1] **LEP EWWG** Collaboration, ALEPH *et al.*, "Precision Electroweak Measurements and Constraints on the Standard Model," `arXiv:0911.2604 [hep-ex]`.

[2] **Tevatron Electroweak Working Group** Collaboration, "Updated Combination of CDF and D0 Results for the Mass of the W Boson," `arXiv:0908.1374 [hep-ex]`.

[3] D. W. M. Group, "Measurement of the W Boson Mass using RunIIa Data,". DØ Note 5868.

[4] G. Grindhammer, M. Rudowicz, and S. Peters, "THE FAST SIMULATION OF ELECTROMAGNETIC AND HADRONIC SHOWERS," *Nucl. Instrum. Meth.* **A290** (1990) 469.

[5] Andeen, Tim and Cwiok, Mikolaj and Guo, Jun and Hobbs, John and Osta, Jyotsna and Stark, Jan and Zhu, Junjie, "Modeling the Hadronic Recoil for a precision measurement of the W mass in the Run IIa analysis at DØ(Method I),". DØ Note 5668.

[6] T. Andeen, F. Guo, J. Guo, and J. Zhu, "Effect of recoil on electron identification efficiency,". DØ Note 5105.

[7] M. E. Peskin and D. V. Schroeder, "An Introduction to quantum field theory,". Reading, USA: Addison-Wesley (1995) 842 p.

[8] **CDF** Collaboration, N. Krumnack, "Combined SM Higgs Limits at the Tevatron," `arXiv:0910.3353 [hep-ex]`.

[9] **D0** Collaboration, V. M. Abazov *et al.*, "Measurement of the W boson mass," *Phys. Rev. Lett.* **103** (2009) 141801, `arXiv:0908.0766 [hep-ex]`.

[10] P. M. Nadolsky *et al.*, "Implications of CTEQ global analysis for collider observables," *Phys. Rev.* **D78** (2008) 013004, `arXiv:0802.0007 [hep-ph]`.

[11] S. Alekhin, J. Blumlein, S. Klein, and S. Moch, "Variable-flavor-number scheme in analysis of heavy-quark electro-production data," `arXiv:0908.3129 [hep-ph]`.

[12] A. D. Martin, W. J. Stirling, R. S. Thorne, and G. Watt, "Parton distributions forthe lhc," *Eur. Phys. J.* **C63** (2009) 189–285, `arXiv:0901.0002 [hep-ph]`.

[13] J. C. Collins, D. E. Soper, and G. Sterman, "Transverse Momentum Distribution in Drell-Yan Pair and W and Z Boson Production," *Nucl. Phys.* **B250** (1985) 199.

[14] F. Landry, R. Brock, P. M. Nadolsky, and C. P. Yuan, "Tevatron Run-1 Z boson data and Collins-Soper-Sterman resummation formalism," *Phys. Rev.* **D67** (2003) 073016, `arXiv:hep-ph/0212159`.

[15] **D0** Collaboration, V. M. Abazov *et al.*, "Measurement of the shape of the boson transverse momentum distribution in $p\bar{p} \to Z/\gamma^* \to e^+e^- + X$ events produced at $\sqrt{s}$=1.96-TeV," *Phys. Rev. Lett.* **100** (2008) 102002, `arXiv:0712.0803 [hep-ex]`.

[16] J. C. Collins and D. E. Soper, "Angular Distribution of Dileptons in High-Energy Hadron Collisions," *Phys. Rev.* **D16** (1977) 2219.

[17] E. Mirkes, "Angular decay distribution of leptons from W bosons at NLO inhadronic collisions," *Nucl. Phys.* **B387** (1992) 3–85.

[18] **D0** Collaboration, V. M. Abazov *et al.*, "The Upgraded D0 Detector," *Nucl. Instrum. Meth.* **A565** (2006) 463–537, `arXiv:physics/0507191`.

[19] **D0** Collaboration, R. Angstadt *et al.*, "The Layer 0 Inner Silicon Detector of the D0 Experiment," `arXiv:0911.2522 [physics.ins-det]`.

[20] **D0** Collaboration, D. Smirnov, "Status of the D0 fiber tracker and preshower detectors," *Nucl. Instrum. Meth.* **A598** (2009) 94–97.

[21] M. Abolins *et al.*, "Design and Implementation of the New D0 Level-1 Calorimeter Trigger," *Nucl. Instrum. Meth.* **A584** (2008) 75–97, `arXiv:0709.3750 [physics.ins-det]`.

[22] M. Wetstein, J. Stark, and M. Verzocchi, "Gain Calibration for the EM Calorimeter in RunII,". DØ Note 5004 (2006).

[23] T. R. Andeen, Jr., "Measurement of the W Boson Mass with the D0 Run II Detector using the Electron P_T Spectrum,". FERMILAB-THESIS-2008-24.

[24] J. Guo, “A Precision Measurement of the W Boson Mass,”. FERMILAB-THESIS-2009-24.

[25] ALEPH *et al.*, “Precision electroweak measurements on the Z resonance,” *Phys. Rept.* **427** (2006) 257, `arXiv:hep-ex/0509008`.

[26] D. Adams, “Finding Tracks,”. DØ Note 2958.

[27] H. Greenlee, “The DØ interacting Propagator,”. DØ Note 4293.

[28] H. Greenlee, “The DØ Kalman Track Fit,”. DØ Note 4303.

[29] A. V. Konychev and P. M. Nadolsky, “Universality of the Collins-Soper-Sterman nonperturbative function in gauge boson production,” *Phys. Lett.* **B633** (2006) 710–714, `arXiv:hep-ph/0506225`.

[30] C. Balazs, J.-w. Qiu, and C. P. Yuan, “Effects of QCD resummation on distributions of leptons from the decay of electroweak vector bosons,” *Phys. Lett.* **B355** (1995) 548–554, `arXiv:hep-ph/9505203`.

[31] C. Balazs and C. P. Yuan, “Testing multiple gluon dynamics at the Tevatron,” *Phys. Rev. Lett.* **79** (1997) 2398–2401, `arXiv:hep-ph/9703405`.

[32] G. A. Ladinsky and C. P. Yuan, “The Nonperturbative regime in QCD resummation for gauge boson production at hadron colliders,” *Phys. Rev.* **D50** (1994) 4239, `arXiv:hep-ph/9311341`.

[33] C. Balazs and C. P. Yuan, “Soft gluon effects on lepton pairs at hadron colliders,” *Phys. Rev.* **D56** (1997) 5558–5583, `arXiv:hep-ph/9704258`.

[34] D. Stump *et al.*, “Inclusive jet production, parton distributions, and the search for new physics,” *JHEP* **10** (2003) 046, `arXiv:hep-ph/0303013`.

[35] E. Barberio and Z. Was, “PHOTOS: A Universal Monte Carlo for QED radiative corrections. Version 2.0,” *Comput. Phys. Commun.* **79** (1994) 291–308.

[36] T. Sjostrand, L. Lonnblad, S. Mrenna, and P. Z. Skands, “Pythia 6.3 physics and manual,” `arXiv:hep-ph/0308153`.

[37] **D0** Collaboration, Abazov, Victor Mukhamedovich and others, “Measurement of the shape of the boson transverse momentum distribution in pp → Z → e^+e^- + X events produced at $\sqrt{\text{s}}$=1.96-TeV,” *Phys. Rev. Lett.* **100** (2008) 102002, `arXiv:0712.0803 [hep-ex]`.

[38] T. Andeen and A. Melnitchouk, "Measurement of electron energy scale and offset with Z → ee full monte carlo and data,".

[39] S. Yacoob, J. Stark, and H. Schellman, "Preparation of Zero Bias Events for Overlay onto Monte Carlo as Part of the D0 RunIIb W Mass analysis,". DØ Note 5875.

[40] **UA2** Collaboration, Alitti,J and others, "An improved determination of the ratio of W and Z masses at the CERN collider," *Phys. Lett. B* **"276"** (1992) "354".

[41] J. Hays, J. Mitrevske, C. Schwanenberger and T. Toole, "Single Electron Efficiencies in p17 Data and Monte-Carlo Using p18.05.00 d0correct,".

[42] J. Stark.

[43] J. Stark, "Measurement of the mass of the W boson status of the direct measurement of the W width,".